Scattering by Irregular Particles in Anomalous Diffraction and Discrete Dipole Approximations

by
Piotr J. Flatau

Department of Atmospheric Science
Colorado State University
Fort Collins, Colorado

William R. Cotton, P.I.

**Colorado
State**
University

Department of Atmospheric Science

Paper No. 517

SCATTERING BY IRREGULAR PARTICLES IN ANOMALOUS DIFFRACTION AND DISCRETE DIPOLE APPROXIMATIONS

by

Piotr J. Flatau

Department of Atmospheric Science

Colorado State University

Fort Collins, CO 80523

November 30, 1992

Atmospheric Science Paper No. 517

ABSTRACT

SCATTERING BY IRREGULAR PARTICLES IN ANOMALOUS DIFFRACTION
AND DISCRETE DIPOLE APPROXIMATIONS

The effects of irregular particles on scattering of radiation are considered using theoretical
methods. Major motivation for studying scattering by irregular particles is presented on
the basis of results from a simple climate model. These results indicate that uncertainties
in our knowledge of the asymmetry parameter and extinction factors significantly affect
the response of this model to an imposed climate change. The discrete dipole approxi-
mation (DDA) is considerably extended in this study. It is shown that this is a robust
method as it includes boundary conditions in its formulation, is numerically stable, and
is computationally fast. The method is validated against exact results. DDA is then ap-
plied to study scattering by particle shapes typical of ice crystal clouds. Parameterization
of scattering properties of irregular particles is considered on the basis of the anomalous
diffraction theory. The new approach to the ADT is introduced based on a ray tracing and
compared to DDA for selected geometries. We develop the ADT for particles distributed
in size. A key result is that the similarity scaling predicted by the ADT for spheres is
also shown to apply for nonspherical particles. The results represent a complete param-
eterization of the three main optical properties: the volume extinction β_{ext}, the single
scattering albedo ω, and the particle asymmetry parameter g, as a function of refractive
index, characteristic radius of the distribution and the distribution width.

Piotr J. Flatau
Department of Atmospheric Science
Colorado State University
Fort Collins, Colorado 80523
Fall 1992

ACKNOWLEDGEMENTS

TABLE OF CONTENTS

Chapter 1

INTRODUCTION

1.1 Scattering by irregular particles — problem statement

"Nonspherical particles are abundant in nature: falling rain drops are elongated, many hailstones have nonconcentric cores, hexagonal ice crystals give rise to beautiful halo phenomena, and snowflakes are well known for their intricate forms.

The scattering law of nonspherical particles that are much smaller than the wavelength is governed by their polarizability tensor. The theory is well known ... Particles of simple shape that are much larger that the wavelength may be treated by a combination of geometrical optics and Fraunhofer diffraction... At intermediate sizes, fancy theoretical methods and relatively simple shapes are needed to solve the problem at all. For those sizes empirical knowledge must be relied upon."

This quote after van de Hulst (1980) conveys the essential motivation for this dissertation: the goal is to advance our knowledge about the effects of irregular particles on scattering radiation.

At present, there is no simple general answer to the question concerning the importance of particle shape on particle scattering. A particular answer depends on the problem under consideration; such as:

- High resolution spectroscopy, optical particle sizing, local albedo returns (radar), line-by-line radiative transfer calculations, angular dependence of lidar backscatter, halo, and directional cloud albedo, are all examples where the shape is important. These are processes which depend on details of particle structure.

- On the other hand it is not clear if the time- or space-averaged (bulk) radiative properties such as optical thickness, hemispherical albedo, radiative heating rates, and passive radiometric measurements are strongly shape dependent. The reason may be that such a response "feels" only a randomly averaged ensemble of particles which may be approximated in terms of some equivalent sphere.

Another reason why it is not simple to determine the effects of particles on scattering is due to the limited knowledge about scattering by irregular particles: it is difficult to solve the Maxwell's equations with complex boundary conditions and it is difficult to measure scattering by irregular particles.

1.2   Goals of research

A fairly recent work (Perry et al., 1978) states that, "For arbitrary shapes and sizes, it is not possible to calculate the exact solution for the ... (scattering) matrix elements".

The broad goal of this thesis is to provide some understanding of the effects of particle shape on the scattering of electromagnetic radiation by finding exact solutions of scattering by irregular particles. Another goal is to capture the essence of the scattering properties and construct a suitable parameterization of them. This step, in principle, involves an additional level of difficulty as detailed knowledge of the evolution of size spectra, shapes, orientations, and coagulation rates for non-spherical particles is needed.

The number of possible applications of this work is large. Scattering by irregular particles is relevant to passive and active remote sensing, cirrus cloud properties and cirrus cloud detection systems, to studies of the earth's radiation budget, climate and climate feedback, radiative heating rates, to particle inversion problems and techniques, estimation of effective particle radius, high- and low- resolution atmospheric spectroscopy, atmospheric aerosols, estimates of cloud albedo and optical thickness, lidar backscatter and radar backscatter. Clearly, not all issues can be addressed here. However, we discuss some applications to climate and climatic feedback to establish a general motivation for the work and consider the scattering results in relation to studies of the radiative properties of cirrus cloud, and to the radiative parameterizations in mesoscale models. There are

several recent papers and reviews on the subject (Wiscombe and Mugnai, 1986; Pollack and Cuzzi, 1980; Bohren and Singham, 1991) where other applications are discussed.

1.3 Method of the research and its plan

The method used to address the goals of this research is theoretical in nature. Before launching into these scattering theories and the DDA, we present one of the major motivations for studying scattering by irregular particles in Chapter 2. Results from a simple climate model are shown to indicate how uncertainties in our knowledge of the asymmetry parameter and extinction factors significantly affect the response of this model to an imposed climate change.

A numerical procedure is introduced in Chapter 3 to study some basic properties of scattering by non spherical particles and tests of this model are introduced to validate it. The numerical method is the discrete dipole approximation (DDA) first introduced by Purcell and Pennypacker (1973) but is considerably extended in this study. The discrete dipole approximation (a.k.a coupled dipoles, methods of moments) is based on the volume integral method, i.e. Helmholtz form of Maxwell equations (Saxon, 1955). It is shown that this is a robust method as it includes boundary conditions in its formulation, is numerically stable, and is computationally fast. The method is validated in Chapter 4 where new calculations of sphere clusters are introduced. DDA is then applied to study particle shapes typical of ice crystals clouds in Chapter 5. Here the scattering asymmetry parameter is studied.

In seeking to parameterize scattering properties we use a simple model of particle scattering referred to as the anomalous diffraction theory (ADT, but a.k.a coupled dipoles, methods of moments). This theory provides a simple mathematical structure to derive both the extinction and absorption properties of the particle. The new approach to the ADT is introduced in Chapter 6 based on ray tracing and compared to DDA for selected geometries. Chapter 7 takes the ADT and develops it further for particles distributed in size accordingly to a gamma distribution. The results are expressed in terms of an analytic function for spheres. It is suggested that the same functional form might also apply to

non spheres after some empirical adjustments are made to the parameters of the model. A key result is the similarity scaling predicted by the ADT which is also shown to apply to the Mie solution for spheres and for nonspherical particles. The results of this Chapter, together with those in Chapter 5 represent a complete parameterization of the three main optical properties of spheres: the volume extinction β_{ext}, the single scattering albedo ω, and the particle asymmetry parameter g, as a function of refractive index, characteristic radius of the distribution and the distribution width.

1.4 Physical examples

While this dissertation is mostly theoretical it is strongly based and motivated by experimental results. These results are briefly reviewed throughout this thesis. Interested readers may find it useful to browse the relevant material before reading theoretical developments. Chapter 2 contains an introductory review and additional references to the contemporary problem of climate change. The introductory section of Chapter 5 discusses crystal shapes in cirrus clouds. Chapter 3 discusses numerous physical examples related to DDA applications. Connections between experiment and theory is discussed in Section 8.3.3.

Chapter 2

THE RELEVANCE OF THE MICROPHYSICAL PROPERTIES OF CIRRUS CLOUDS TO CLIMATE

This Chapter establishes the importance of studying light scattering by irregular particles for the climate problems. We examine the effects of the cloud optical properties and their relation to ice water content and particle size on a simple climate system. The more detailed account is given elsewhere (Stephens et al., 1990). It is described here only to identify relevant scattering properties, that are the focus of this research.

It is a widespread belief that thin cirrus clouds act to enhance the 'greenhouse effect' owing to a particular combination of their optical properties (Manabe and Wetherald, 1967; Cox,1971; Stephens and Webster, 1981). These optical properties are fundamentally controlled by the properties ice crystal scattering. It is now shown how these scattering properties can fundamentally change the response of a simple climate model to an imposed change of the amount of CO_2.

2.1 A simple climate model

A radiative equilibrium climate model which includes the parameterized effects of convection as used by Stephens and Webster (1981) is also employed. The intent of this exercise is not to simulate the climate response to variations in cirrus clouds but is directed toward understanding the dependence of surface temperature on the radiative properties of cirrus as well as toward investigating simple aspects of the coupling of the surface temperature to ice water content, cloud microphysics, cloud temperature and radiation.

The climate model employs a convective adjustment scheme similar to that of Manabe and Wetherald (1967). With the exception of the new cloud radiation parameterization described above, the radiative transfer model is that outlined in Stephens and Webster

(1981) and is coupled to the convective adjustment scheme to produce a one-dimensional radiative convective model. Radiative equilibrium is approached iteratively at all levels in the atmosphere except where the resultant temperature gradient between layers exceeds the critical lapse rate value which was set to the moist adiabatic value. The model also invokes the assumption of fixed relative humidity and, together with energy conservation, iterates to a stable radiative-convective temperature profile.

2.2 Simulations with fixed ice water

The results of a series climate equilibrium experiments using this model are shown in Fig. 2.1. These are presented as the difference between overcast and clear sky surface temperature ΔT_g, cloud temperature ΔT_c (upper panel), cloud albedo $\mathcal{R}$ and emittance ϵ (lower panel) as a function of r_e derived at equilibrium. The ice water path prescribed for these experiments is 3 $g.m^{-2}$ which corresponds to a $1km$ thick cloud at a temperature of $229°K$. The model simulations were carried out using the two values of asymmetry parameter g in an effort to demonstrate the sensitivity of the simulated climate to the asymmetry parameter, and thus, in a gross way, to the the shape of the ice crystal. The resultant surface warming reported in earlier studies like that of Stephens and Webster (1981) is also reproduced but the magnitude of this warming is strongly dependent on both the value of g and the value of r_e assumed in the derivation of $\mathcal{R}$ and ϵ. For the simulations with fixed ice path, the surface warming tendency is enhanced by either decreasing the particle size or by assuming more forwardly scattering cloud particles. The difference between this model and others is that it includes a feedback between the ice water content of the cloud and the temperature of the of the cloud. Key parameters of the model are the ice water content and particle size (expressed in terms of the r_e, the ratio of the third and the seconds moments of the size distribution), which define the optical depth of the cloud and the asymmetry parameter g which characterizes the angular scattering. More on this parameter is given in Chapter 5.
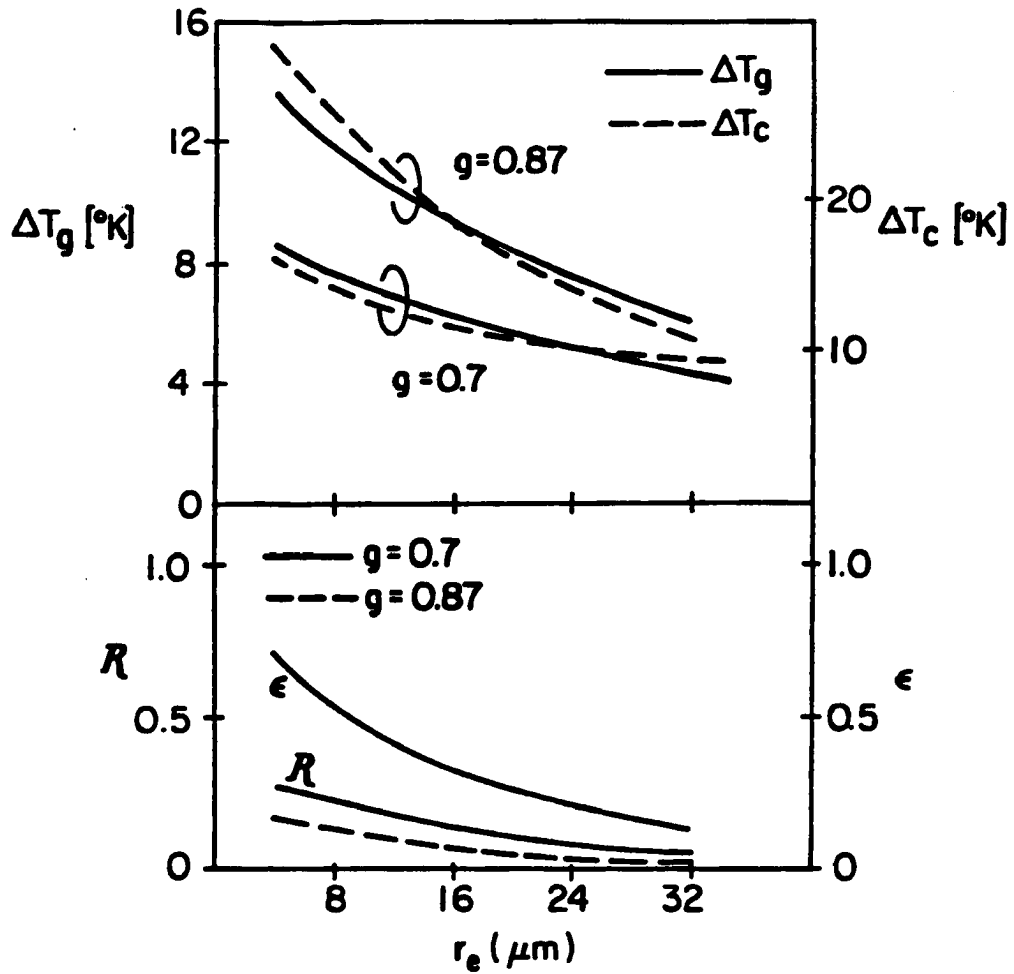
Figure 2.1: The difference in the equilibrium surface T_g and cloud T_c temperatures as a function of r_e for two values of asymmetry (upper panel) and the respective change in cloud emittance and albedo as a function of $\mathcal{R}$. The climate simulations were conducted using $\mathcal{R}_g = 0.1, F_o = 340 W.m^{-2}, \mu_o = 0.49$ and a fixed ice water content $W = 3.0 g.m^{-2}$.

2.3 Simulations with ice water feedback

The ice water feedback was examined by analyzing pairs of control/perturbation simulations with the radiative equilibrium model. The perturbation experiment represents the simulations with twice the present day CO_2 concentration and the control simulations were run with the present day concentrations of CO_2. The notation Δx is used to represent the difference between the perturbation and control simulations of a particular climate parameter of interest (say surface temperature). Two pairs of perturbation/control experiments are then compared; one pair was conducted with the ice water feedback included in the model and the second pair assumed fixed values of ice water path. These comparisons are presented in terms of the parameter $\delta x = \Delta x(\text{ with feedback}) - \Delta x(\text{fixed})$. Positive values of δT_g therefore indicate that the ice water feedback acts to reinforce the simulated CO_2 warming and negative values of δT_g indicate a buffering effect against such a warming.

Values of $\delta T_g, \delta T_c$ (upper panel), δW (middle panel) and $\delta\epsilon$ and δR (lower panel) are presented as a function of r_e in Fig. 2.2 All simulations were performed with $g = 0.7$. These results indicate that the sign of the ice water feedback varies according to the value of r_e used by the model to obtain the cloud optical properties. According to these simulations, the feedback is negative when $r_e < 24\mu m$ and positive for clouds composed of large crystals. The explanation for this is revealed by comparison of δR and $\delta\epsilon$ and δW. According to the experiments described here, the difference in the cloud emittance between the perturbation and control experiments which include feedback exceeds the respective change in cloud albedo when r_e is large but is less than the change in albedo for smaller values of r_e.

2.4 Summary and Conclusions

This chapter illustrates the potential effects of cirrus cloud ice water content feedback and ice crystal shapes on climate change. The central question studied concerns the extent to which both the radiative and microphysical properties of cirrus cloud influence this feedback. This question is especially relevant given of the present uncertainty about the

9
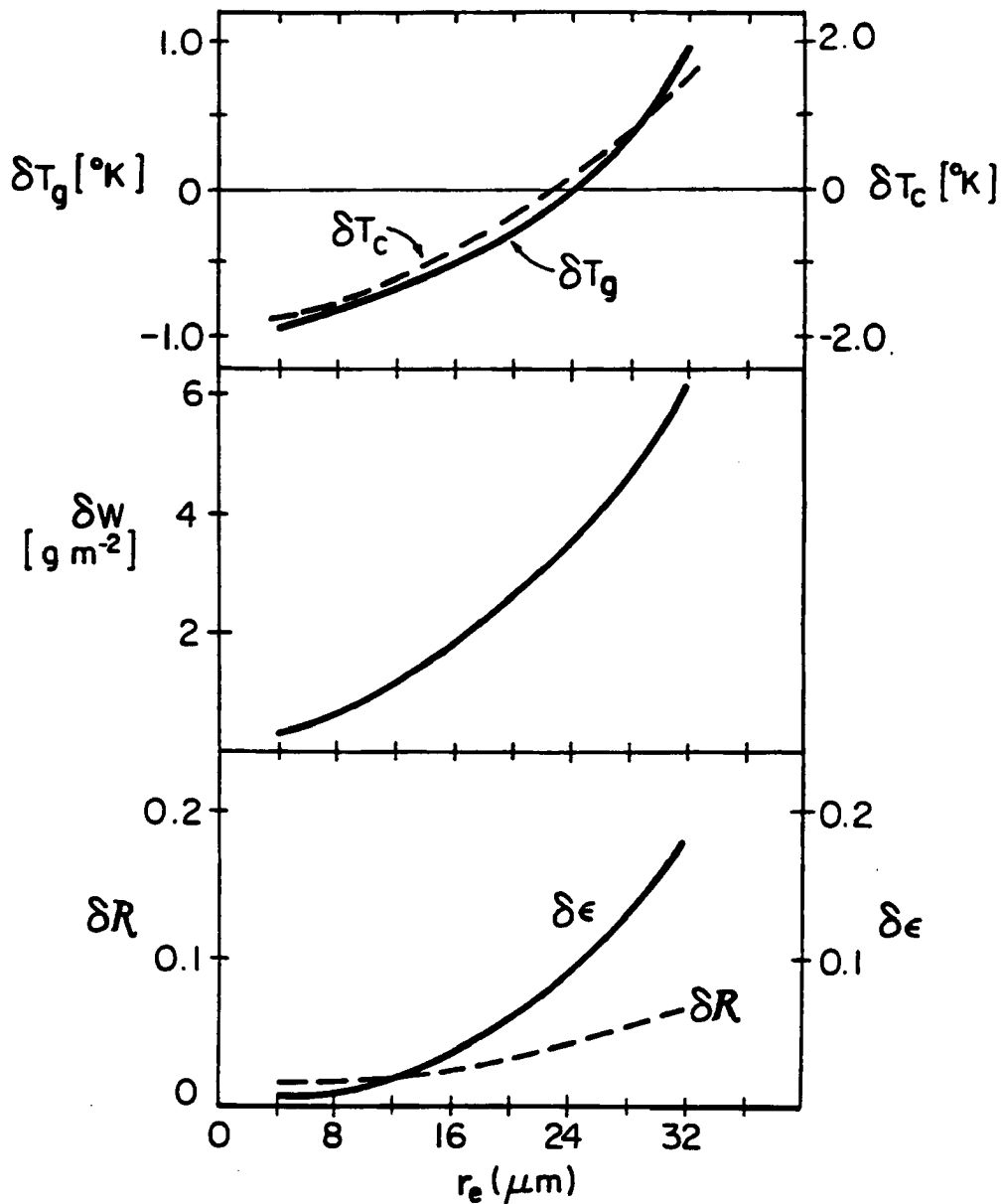
Figure 2.2: The feedback analysis parameter δx as defined in the text shown as a function of r_e. Shown are the effects of ice water feedback on the $2 \times CO_2$ simulations of surface temperature, cloud temperature (upper panel), ice water content (middle panel) and cloud albedo and emittance (lower panel). The simulations were carried out assuming the properties listed in relation to the simulations of Fig.6. Only simulations with $g = 0.7$ are shown.

characteristic size of the ice crystals and impact of crystal shapes in cirrus clouds. The major developments of this work relevant to the research described in this thesis is:

(i) The climate simulations revealed that the predicted effect of cirrus cloud on the surface temperature is sensitive to both r_e (crystal size) and g (crystal shape). Cirrus clouds characterized by $g = 0.87$ (spheres) warmed approximately twice as much as cirrus clouds modeled with $g = 0.7$ (cylinders). According to the parameterizations used, the surface warming was also predicted to be greater for smaller r_e clouds owing to the more dominant effects of particle size on cloud emittance. The model produces a large increase in the temperature of the cloud layer as a result of the absorption of infrared flux by the cloud. The predicted cloud warming is about twice that calculated for the surface and is the mechanism that drives the surface warming in the model.

(ii) The ice water feedback was examined by analyzing pairs of control/perturbation simulations with the radiative equilibrium model. Comparisons of the $(2 \times CO_2 - 1 \times CO_2)$ simulations with and without cloud feedback revealed that the sign of the ice water temperature feedback on CO_2 warming depends on the value of r_e assumed to represent the radiative properties of the cloud.

The study of Stephens *et. al.* (1990) employed observations in an attempt to define the relationship between cloud albedo and cloud emittance on particle size and estimate representative values of g and r_e. While the gross relationships between the relevant cloud optical properties and particle size are poorly understood, a simple idealized model of spherical particles was shown in that study to provide a reasonable match of the observations. Whether this agreement is fortuitous and generally representative of all ice crystals was not known but it is shown later that it should not be universally expected. The three key optical properties of clouds that define their radiative properties are:

1. The optical path:

$$\tau = \int \beta_{ext} dz \qquad (2.4.1)$$

where β_{ext} is the volume extinction efficiency. The optical path defines combined absorption and scattering efficiency of a medium.

2. The single scattering albedo ω,

$$\omega = Q_{sca}/Q_{ext} \qquad\qquad (2.4.2)$$

where Q_{sca} and Q_{ext} are scattering and extinction efficiencies. Single scattering albedo is one in the conservative (no absorption) case and zero for extinction process dominated by absorption.

3. The asymmetry parameter g which defines the (weighted) probability of forward to backward scattering of photons.

The focus of this research is to understand the effect of particle shape and size on β_{ext}, ω, and g.

Chapter 3

LIGHT SCATTERING IN THE DISCRETE DIPOLE APPROXIMATION

3.1 Introduction

The discrete-dipole approximation (DDA) developed by Purcell and Pennypacker (1973) is a very flexible and general technique for calculating the scattering and absorptive properties of particles of arbitrary shapes. This method is the subject of active research in several diverse fields: for example Draine (1988) examines the ultraviolet optical properties of interstellar dust composed of extremely anisotropic, graphite particles. Flatau *et al.* (1990) apply the method to study scattering by hexagonal ice crystals which are common in upper tropospheric cirrus clouds. Goedecke and O'Brien (1988) are concerned with scattering of millimeter waves by snow crystals. Keller and Bustamante (1986) describe the application to spectroscopy of large, internally inhomogeneous, molecular aggregates of chromophores (e.g. viruses or chromosomes) bound together in a rigid structure. The DDA is especially suited to scattering characterized by medium values of the size parameter x, defined as $x = 2\pi a_{eq}/\lambda$, where a_{eq} is the "equivalent radius" (the radius of a sphere of equal volume), and λ is the wavelength of the electromagnetic wave.

Singham and Bohren (1989) recently discussed the virtues of some of the different methods used to solve the DDA. A direct solver method was used by Singham and Salzman (1986), an iterative method of the conjugate-gradient (CCG) type was introduced by Yung (1978), while Born-type expansions have been proposed by several authors (Keller and Bustamante, 1986; Singham and Bohren, 1989).

In this chapter we introduce two different methods of solution based on block-Toeplitz and fast-Fourier-transform (FFT). The block-Toeplitz solver has been developed for the specific case of light scattering by homogeneous rectangular solid parti-

cles. Such particles were studied both theoretically (Napper, 1966; Liou et al., 1983; Purcell and Pennypacker, 1973; Kattawar et al., 1987) as well as experimentally (Napper and Ottewill, 1963; Zerull and Giese, 1974; Zerull, 1976; Zerull et al., 1977a; Perry et al., 1978; Killinger and Zerull, 1988) and occur in nature at low temperatures in the atmosphere such as the "diamond-dust" (Kikuchi and Hogan, 1979; Kajikawa et al., 1980) particles collected in Antarctica. Whalley (1984) suggested that Scheiner's halo may be due to cubic ice. In a review paper, Hallet (1987) mentions materials which could crystallize as a hydrate in the cubic system. Mother-of-pearl clouds (Hallet and Lewis, 1967) and Polar Stratospheric Clouds are both candidates for the existence of cubic particles.

For the particle geometry under consideration, we identify the DDA matrix as a symmetric, BT (block-Toeplitz) matrix and utilize the special properties of such arrays to develop a new algorithm. The special features of rectangular solids that give rise to the particular mathematical structure also exist to a considerable degree for particles of less regular shape and this is exploited here using FFT approach.

This chapter is organized as follows: the next section presents the formulation of the DDA (Purcell and Pennypacker, 1973) and the block-Toeplitz (BT) structure (Bunch, 1985; Friedlander et al., 1979; Arushanian et al., 1983) is introduced in the subsequent section. Next the generalized Levinson (Friedlander et al., 1979) algorithm for the direct solution of the BT matrix is presented and its implementation (Arushanian et al., 1983) is discussed. The role of the Gohberg-Semencul-Heinig (1974) theorem is described and results are shown for cubic particles. Finally we show how fast-Fourier-transform methods can be used to accelerate computations of scattering and absorption by particles of arbitrary shape.

3.2 Discrete dipole approximation

The DDA replaces the solid particle by an array of N point dipoles, with the spacing between the dipoles small compared to the wavelength. The dipoles are assumed to occupy positions on a cubic lattice. Each dipole has an oscillating polarization in response to both

but do offer some simplification as described below. Equation (3.2.5) is a function of the distance and the direction between the dipoles j and k. Thus for the discretized particle, there are many pairs of dipoles which are separated by the same distance and are oriented with respect to each other along the same direction. In addition, tensor $\hat{r}\hat{r}$ is invariant under the $\hat{r} \rightarrow -\hat{r}$ transformation and so is the distance r_{ij}. Therefore, we can write

$$\mathbf{A}(\mathbf{r}_j, \mathbf{r}_k) = \mathbf{A}(\mathbf{r}_k, \mathbf{r}_j) = \mathbf{A}(\mathbf{r}_j - \mathbf{r}_k) \quad (j, k = 1, \dots, N), \quad (j \neq k). \tag{3.2.7}$$

where $\mathbf{A}(\mathbf{r}_j, \mathbf{r}_k) \equiv \mathbf{A}_{jk}$. As we now show, expression (3.2.7) bears a strong resemblance to the definition of a symmetric Toeplitz matrix.

3.3 Block-Toeplitz matrices

A $(K + 1) \times (K + 1)$ symmetric Toeplitz matrix (Bunch, 1985; Arushanian et al., 1983) $\tilde{\mathbf{A}} = [a_{jk}]$ has $K+1$ independent elements defined by $a_{jk} = a_{|j-k|}$ for $j, k = 1, \dots, K$ such that

$$\tilde{\mathbf{A}} = \begin{pmatrix} \mathbf{a}_0 & \mathbf{a}_1^T & \cdots & \mathbf{a}_K^T \\ \mathbf{a}_1 & \mathbf{a}_0 & \ddots & \vdots \\ \vdots & \ddots & \ddots & \mathbf{a}_1^T \\ \mathbf{a}_K & \cdots & \mathbf{a}_1 & \mathbf{a}_0 \end{pmatrix} \tag{3.3.1}$$

where T indicates (matrix) transpose, the elements on each diagonal are equal, and $\mathbf{a}_0 = \mathbf{a}_0^T$. If the a_j's are themselves matrices then $\tilde{\mathbf{A}}$ is said to exhibit block-symmetric-Toeplitz structure.

It will now be shown that the DDA matrix has a special form of block-symmetric-Toeplitz structure for particles which are homogeneous rectangular solids. Such particles can in general be approximated by arrays of identical dipoles located at lattice positions (i, j, k), where $i = 1, \dots, i_{max}$, $j = 1, \dots, j_{max}$, $k = 1, \dots, k_{max}$ and $N = i_{max}j_{max}k_{max}$. Consider the simple case of a three-dimensional particle composed of twelve dipoles as in Fig. 3.1 (with $i_{max} = 2$, $j_{max} = 2$, $k_{max} = 3$). For the sake of discussion, let the dipoles be identified as $d1, d2, \dots, d12$. Let us denote the group of four dipoles lying in *one plane* as $[p1]$ (dipoles $d1, \dots, d4$), as $[p2]$ for dipoles $d5, \dots, d8$, and $[p3]$ for dipoles $d9, \dots, d12$. Let us denote the group of two dipoles lying in *one line* as $[l1]$ for dipoles $d1, d2$, $[l2]$ for

$$k_{max} = 3$$
$$i_{max} = 2$$
$$j_{max} = 2$$
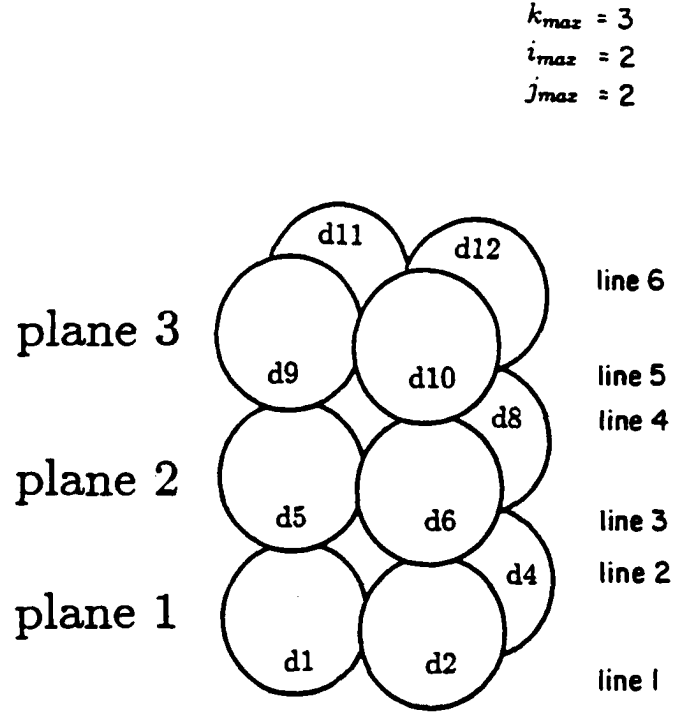
Figure 3.1: Idealized array of discrete dipole structure composed of 12 atoms.

dipoles $d3, d4$, [l3] for dipoles $d5, d6$, [l4] for dipoles $d7, d8$, [l5] for dipoles $d9, d10$, and [l6] for dipoles $d11, d12$. Each dipole interacts with the other dipoles in the array, with the strength of the interaction depending on the distance and the direction. The position of each dipole can be described by three integers (p, q, r) which are components of the r vector: $r = pe_1 + qe_2 + re_3$, where e_1, e_2, and e_3 are unit vectors in three perpendicular directions. The matrix listed in Table 3.1 is a schematic representation of terms that describe the interactions between the twelve dipoles used for this example; each element a_{jk} is a 3x3 matrix given by equations (3.2.5-3.2.6). There are nine"plane" sub-matrices (blocks) to consider and these are emphasized by the dashed lines. For example the upper left block represents the interactions between the $[p1]$ $[p1]$ groups of dipoles. The block structure of the dipole interaction can then be expressed as

$$\bar{A} = \begin{pmatrix} [p1:p1] & [p1:p2] & [p1:p3] \\ [p2:p1] & [p2:p2] & [p2:p3] \\ [p3:p1] & [p3:p2] & [p3:p3] \end{pmatrix} \tag{3.3.2}$$

where the nine blocks $[p1:p1]$, $[p1:p2]$, $[p1:p3]$, $[p2:p1]$, $[p2:p2]$, $[p2:p3]$, $[p3:p1]$, $[p3:p2]$, and $[p3:p3]$ represent those bordered by the dashed lines in the matrix of Table 3.1.

Table 3.1: A matrix of interaction "forces" a_{jk} between twelve dipoles. The bar over the index indicates negative value.

	d1	d2	d3	d4	d5	d6	d7	d8	d9	d10	d11	d12
d1	a_{000}	a_{010}	a_{100}	a_{110}	a_{001}	a_{011}	a_{101}	a_{111}	a_{002}	a_{012}	a_{102}	a_{112}
d2	$a_{0\bar10}$	a_{000}	$a_{1\bar10}$	a_{100}	$a_{0\bar11}$	a_{001}	$a_{1\bar11}$	a_{101}	$a_{0\bar12}$	a_{002}	$a_{1\bar12}$	a_{102}
d3	$a_{\bar100}$	$a_{\bar110}$	a_{000}	a_{010}	$a_{\bar101}$	$a_{\bar111}$	a_{001}	a_{011}	$a_{\bar102}$	$a_{\bar112}$	a_{002}	a_{012}
d4	$a_{\bar1\bar10}$	$a_{\bar100}$	$a_{0\bar10}$	a_{000}	$a_{\bar1\bar11}$	$a_{\bar101}$	$a_{0\bar11}$	a_{001}	$a_{\bar1\bar12}$	$a_{\bar102}$	$a_{0\bar12}$	a_{002}
d5	$a_{00\bar1}$	$a_{01\bar1}$	$a_{10\bar1}$	$a_{11\bar1}$	a_{000}	a_{010}	a_{100}	a_{110}	a_{001}	a_{011}	a_{101}	a_{111}
d6	$a_{0\bar1\bar1}$	$a_{00\bar1}$	$a_{1\bar1\bar1}$	$a_{10\bar1}$	$a_{0\bar10}$	a_{000}	$a_{1\bar10}$	a_{100}	$a_{0\bar11}$	a_{001}	$a_{1\bar11}$	a_{101}
d7	$a_{\bar10\bar1}$	$a_{\bar11\bar1}$	$a_{00\bar1}$	$a_{01\bar1}$	$a_{\bar100}$	$a_{\bar110}$	a_{000}	a_{010}	$a_{\bar101}$	$a_{\bar111}$	a_{001}	a_{011}
d8	$a_{\bar1\bar1\bar1}$	$a_{\bar10\bar1}$	$a_{0\bar1\bar1}$	$a_{00\bar1}$	$a_{\bar1\bar10}$	$a_{\bar100}$	$a_{0\bar10}$	a_{000}	$a_{\bar1\bar11}$	$a_{\bar101}$	$a_{0\bar11}$	a_{001}
d9	a_{002}	$a_{0\bar12}$	a_{102}	$a_{1\bar12}$	$a_{00\bar1}$	$a_{0\bar1\bar1}$	$a_{10\bar1}$	$a_{1\bar1\bar1}$	a_{000}	$a_{0\bar10}$	a_{100}	$a_{1\bar10}$
d10	$a_{0\bar12}$	a_{002}	$a_{1\bar12}$	a_{102}	$a_{0\bar1\bar1}$	$a_{00\bar1}$	$a_{1\bar1\bar1}$	$a_{10\bar1}$	$a_{0\bar10}$	a_{000}	$a_{1\bar10}$	a_{100}
d11	$a_{\bar102}$	$a_{\bar112}$	a_{002}	a_{012}	$a_{\bar10\bar1}$	$a_{\bar11\bar1}$	$a_{00\bar1}$	$a_{01\bar1}$	$a_{\bar100}$	$a_{\bar110}$	a_{000}	a_{010}
d12	$a_{\bar1\bar12}$	$a_{\bar102}$	$a_{0\bar12}$	a_{002}	$a_{\bar1\bar1\bar1}$	$a_{\bar10\bar1}$	$a_{0\bar1\bar1}$	$a_{00\bar1}$	$a_{\bar1\bar10}$	$a_{\bar100}$	$a_{0\bar10}$	a_{000}

Matrix $\bar{\text{A}}$ has block-Toeplitz structure, and all twelve of the blocks are themselves BT. For example $[p1 : p1]$ sub-block has structure

$$[p1 : p1] = \begin{pmatrix} [l1:l1] & [l1:l2] \\ [l2:l1] & [l2:l2] \end{pmatrix} \qquad (3.3.3)$$

where $[l1 : l1]$, $[l1 : l2]$, $[l2 : l1]$, and $[l2 : l2]$ are 2×2 "line" sub-blocks. The blocks $[l1 : l1]$ and $[l2 : l2]$ are also equivalent and are BT since the interactions between the dipoles in a line depends only on the distance and not on their direction. Interaction between dipoles from two *different* planes is thus described by $[p_m : p_n]$, where $m, n = 1, 2, 3$ and $m \neq n$. The invariance to the $\mathbf{r} \rightarrow -\mathbf{r}$ transformation gives $a_{p,q,r} = a_{-p,-q,-r}$. Thus matrix $[p_m : p_n]$ is the transposed $[p_n : p_m]$. Thus the interaction matrix is *block*-Toeplitz, and block-symmetric. Each of the block matrices are of BT structure themselves. The resulting *plane-plane* interactions, and within each plane the *line-line* interactions, and within the line *dipole-dipole* interactions lead to the embedded BT structure; the notation (Arushanian et al., 1983) TTT is appropriate to indicate such a three-level matrix. More specifically, this structure might be denoted $T_{sb}(T_b(T_b(G_s)))$ – block-symmetric-Toeplitz, with blocks which are themselves BT (but not symmetric), with sub-blocks which are themselves BT (but not symmetric), with 3x3 sub-blocks which are symmetric (but not Toeplitz).

3.4 Algorithm and its implementation

We now exploit the properties of the block-Toeplitz matrix in order to solve (3.2.1) in less than $O(K^3)$ operations and with less than $O(K^2)$ storage. If we assume that each block has the dimension $p \times p$ and that there are n of them, then $K = pn$ (in the present application, n is the number of planes, and $p/3$ is the number of dipoles in one plane).

It is clear from (3.3.1) that for the block-symmetric block-Toeplitz matrix, the first block-column is sufficient to store the whole matrix; thus the required storage is $p^2 n$ which is smaller than K^2 by a factor n. Gohberg and Heinig (Gohberg and Heinig, 1974; Friedlander et al., 1979) have shown that the inverse of the Toeplitz matrix can be stored in $2p^2 n$ storage. This result is non-trivial because the inverse of the Toeplitz matrix is non-Toeplitz, so the special structure of (3.3.1) disappears. The particular algorithm which we present below takes advantage of the BT structure with general (i.e. non-Toeplitz) sub-blocks (TG-structure). Unfortunately, it seems that there are no algorithms currently in existence which would allow us to capitalize further on the TTT-structure of the DDA matrices (Arushanian et al., 1983). Thus the algorithm is of order $p^3 n^2$, which can be orders of magnitude better than for direct solvers which are $O(p^3 n^3)$.

The following algorithm (Friedlander et al., 1979; Arushanian et al., 1983; Gohberg and Heinig, 1974) is used to solve (3.2.1) and find $\tilde{A}^{-1}$. Let $\tilde{A}$ be a BT matrix of order $(n+1)p$ defined by (3.3.1). Let us denote by $A_k = [A_{k,k}, A_{k,k-1}, \ldots, A_{k,0}]$ and by $B_k = [B_{k,k}, B_{k,k-1}, \ldots, B_{k,0}]$, the last and the first block row of (unknown) $\tilde{A}^{-1}$. We define the $p \times p$ matrix polynomials $A_k(z) = \sum_{i=0}^{k} A_{k,i} z^i$ and $B_k(z) = \sum_{i=0}^{k} B_{k,i} z^i$. These polynomials satisfy the recurrence relations

$$A_k(z) - X_k B_k(z) = A_{k-1}, \tag{3.4.1}$$

$$B_k(z) - Y_k A_k(z) = z B_{k-1}(z) \tag{3.4.2}$$

where the $p \times p$ matrices X_k and Y_k are given by

$$X_k = -A_{k-1} \begin{pmatrix} a_1 \\ \vdots \\ a_k \end{pmatrix}, \quad Y_k = -B_{k-1} \begin{pmatrix} a_k^T \\ \vdots \\ a_1^T \end{pmatrix} \qquad (3.4.3)$$

With an arbitrary matrix polynomial $A_k(z) = \sum_{i=0}^{n} A_{k,i} z^i$ let us associate matrices

$$\mathcal{L}_k[A(z)] = \begin{pmatrix} a_0 & 0 & \cdots & 0 \\ a_1 & a_0 & \ddots & \vdots \\ \vdots & \ddots & \ddots & 0 \\ a_k & \cdots & a_1 & a_0 \end{pmatrix} \qquad (3.4.4)$$

and

$$\mathcal{L}_k^T[A(z)] = \begin{pmatrix} a_0 & a_1 & \cdots & a_k \\ 0 & a_0 & \ddots & \vdots \\ \vdots & \ddots & \ddots & a_1 \\ 0 & \cdots & 0 & a_0 \end{pmatrix} \qquad (3.4.5)$$

for any $k \leq n$. The Gohberg-Semencul-Heinig algorithm (for the block-symmetric case) for the inverse of $\tilde{A}$ is

$$\begin{aligned} \tilde{A}^{-1} &= \mathcal{L}^T[A_k^T(z)]\mathcal{L}_k[M_k^{-1}A_k(z)] \\ &\quad - \mathcal{L}_k^T[zB_k^T(z)]\mathcal{L}_k[zN_k^{-1}B_k(z)], \end{aligned} \qquad (3.4.6)$$

where $M_k = A_{k,0}$, and $N_k = B_{k,k}$. The essence of the algorithm is that the full inverse of $\tilde{A}^{-1}$ can be constructed from the *two* block-columns and the algorithm exploits (recursively) the special structure of BT matrices.

3.5 Block-Toeplitz solver — timing results

The block-Toeplitz algorithm provides a practical way to solve the DDA scattering problem for large values of N and rectangular targets, and we proceed now to present some results for cubes and parallelepipedes. The Gohberg-Semencul-Heinig algorithm has been implemented in a FORTRAN package (Arushanian et al., 1983) available from NETLIB (Dongarra and Grosse, 1987). We solve DDA problem on a lattice of $N = 1400 = 14 \times 10 \times 10$ dipoles. For incident radiation propagating in the positive x-direction and linearly polarized in the y-direction, two scattering planes are considered: the xy and xz planes. In both cases two linear polarizations are considered: parallel and perpendicular

Table 3.2: Comparison of direct (Linpack), block-Toeplitz, and conjugate gradient (CCG) methods. Titan/Ardent CPU time (in seconds) is given.

Cube	Dipoles	CCG	Linpack	Toeplitz
$4 \times 4 \times 4$	64	5.7	3.3	5.6
$6 \times 6 \times 6$	216	62.7	115.5	113.6
$8 \times 8 \times 8$	512	350.5	1584.3	1051.8
$10 \times 10 \times 10$	1000	1329.3	–	6254.2

to the scattering plane. We consider a sequence of rectangular targets, consisting of $(4 + 2M) \times 4 \times 4$ dipoles, for $M = 0, 1, \ldots, 9$. The elongation is in the x-direction, and we hold the refractive index n and $2\pi a_{eq}/\lambda = 3.158$ constant as we vary M. Fig. 3.2 presents central processor time (on a Titan/Ardent computer, with a Linpack benchmark rating of 6 Mflops; the Linpack benchmark is available from NETLIB (Dongarra and Grosse, 1987)) for 3 different methods: complex conjugate gradient (CCG), Linpack direct solver (Dongarra et al., 1978), and the block-Toeplitz algorithm. One can notice that the Linpack solver is slow (N^3-dependence) whereas CCG and Toeplitz are comparable, with CPU time $\propto N^2$, and much faster than Linpack for large N. For an arbitrary matrix, the CCG method should be *slower* than Linpack because the former is iterative. However, the CCG method converges very rapidly in our case, which probably indicates that the CCG method is able to exploit the "hidden" block-symmetry of the problem. We have also run larger problems and the results are presented in Table 3.2.

Already for $N = 512$ the Linpack solver is the slowest of the three methods. For $N = 1000$ we were unable to store the 3000×3000 complex matrix required for the Linpack solver. Although results in Table 3.2 indicate that the BT results are slower than CCG it is worth stressing that the BT is a *direct* method; thus, in principle, for each new incident direction/polarization, the original $\tilde{A}^{-1}$ can be used to obtain the solution $\tilde{P} = \tilde{A}^{-1}\tilde{E}_{inc}$ in only K^2 operations (whereas each subsequent CCG calculation requires γK^2 operations, with $\gamma \approx 10 - 20$). This is an important point for orientational averages:
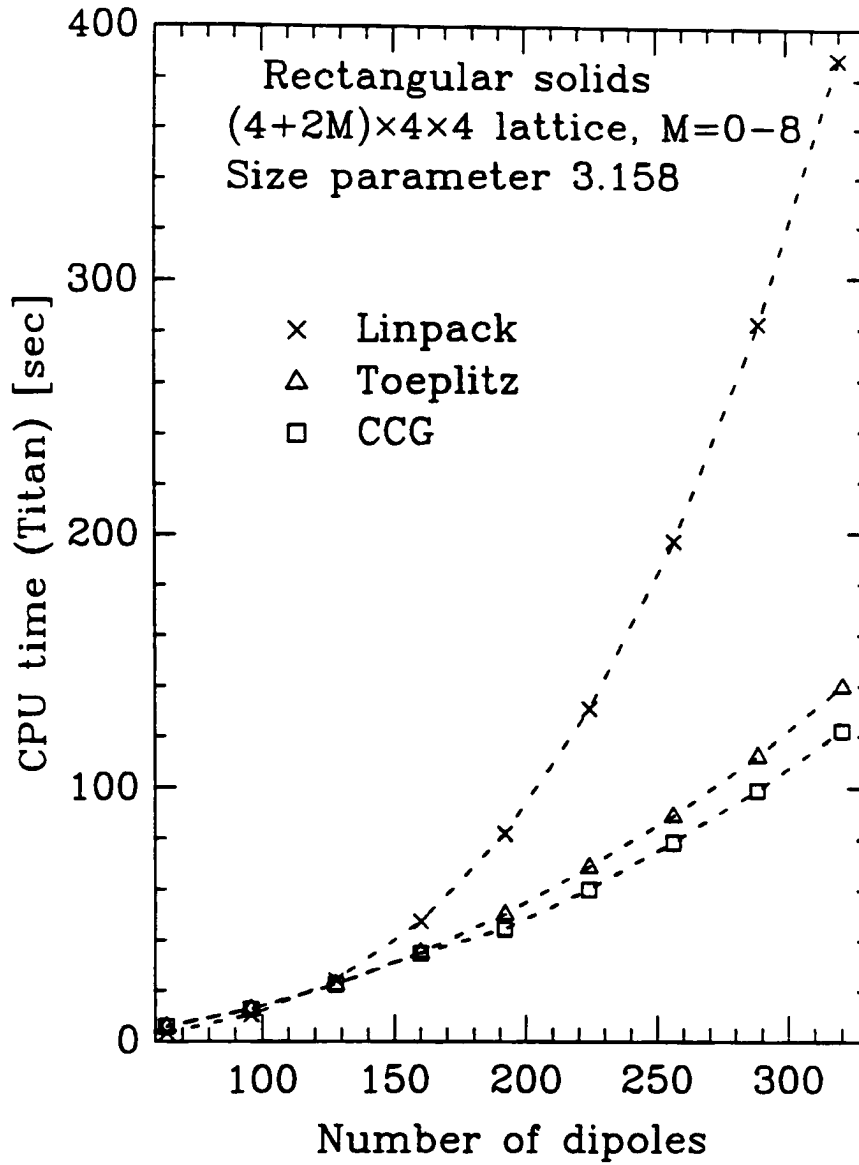
Figure 3.2: CPU time (on a Titan/Ardent workstation) as a function of dipole number for three methods: complex conjugate gradient (CCG), direct matrix solver (Linpack), and the block-Toeplitz solver.

For example it was observed by Singham and Salzman (Singham and Salzman, 1986) that the number of orientations required for the proper averaging depends on the size parameter and varies, in their case, between 3000 and 15000. We should mention that the current *implementation* of the Toeplitz package (Arushanian et al., 1983) does *not* store factored matrix $\tilde{A}^{-1}$, but this is a (remediable) deficiency of the particular implementation and not that of the algorithm.

3.6 Application of FFT techniques to the discrete dipole approximation

Draine (1988) discusses the use of the conjugate-gradient algorithm ("CG") to solve (3.2.1) by iteration. In brief, beginning from an initial "guess" $P_j^{(0)}$, the CG method generates a sequence $P_j^{(n)}$ ($n = 1, 2, ..$) which converges monotonically to the exact solution for $n = 3N$, and may yield an excellent approximation in far fewer than $3N$ iterations. The CG method does not require the actual components of A, but only matrix-vector products of the form $A \cdot X$ and $A^\dagger \cdot X$, where $\dagger$ signifies the hermitian conjugate. The FFT (Goodman et al., 1991) can be used to evaluate these products if the dipoles are located on a cubic lattice: $i \equiv (i_x, i_y, i_z)$, $r_i \equiv (i_x d, i_y d, i_z d) + r_0$, where $i_x \in \{1, 2, \ldots, N_x\}$, $i_y \in \{1, 2, \ldots, N_y\}$, etc.; $N_L \equiv N_x N_y N_z$ is the number of lattice sites in a rectangular volume containing the N "occupied" sites. Since (3.2.5) depends on r_i and r_j through their difference $r_{ij} \equiv r_i - r_j$, A_{ij} depends only upon the difference of its indices. We define

$$A_{ij} \equiv \begin{cases} A'_{i-j}, & \text{if } i \neq j; \\ 0, & \text{if } i = j. \end{cases} \tag{3.6.1}$$

Let the lattice be doubled in each dimension: e.g., $i_x \in \{1, 2, \ldots, 2N_x\}$, and regard A'_i and X_i as periodic in each dimension, e.g. $X_{(i_x, i_y, i_z)} = X_{(i_x \pm 2N_x, i_y, i_z)}$. Set $X_i = 0$ if $N_x < i_x \leq 2N_x$, $N_y < i_y \leq 2N_y$, or $N_z < i_z \leq 2N_z$. Then, for example, the product $Y_i \equiv (A \cdot X)_i$ is

$$Y_i = \sum_{j_x=0}^{2N_x} \sum_{j_y=0}^{2N_y} \sum_{j_z=0}^{2N_x} A'_{i-j} \cdot X_j \equiv \sum_j{}' A'_{i-j} \cdot X_j. \tag{3.6.2}$$

Because (3.6.2) is a convolution, it can be evaluated by Fourier transforms: $\hat{Y}_n = \hat{A}'_n \cdot \hat{X}_n$. Here $\hat{Y}$, $\hat{A}'$, and $\hat{X}$ are the discrete Fourier transforms of Y, A', and X; e.g.,

$$\hat{Y}_n \equiv \sum_i{}' Y_i \exp\left[i \left(\frac{n_x i_x}{2N_x} + \frac{n_y i_y}{2N_y} + \frac{n_z i_z}{2N_z} \right) \right]. \tag{3.6.3}$$

Y can then be computed from the inverse of (3.6.3).

Evaluating $\hat{\mathbf{A}}'_n \cdot \hat{\mathbf{X}}_n$ for all n involves $O(N_L)$ operations, and, if N_x, N_y, and N_z are highly factorizable, the Fourier transforms require $O(N_L \ln N_L)$ operations with the FFT algorithm; thus $\mathbf{A} \cdot \mathbf{X}$ can be evaluated in $O(N_L \ln N_L)$ rather than $O(N^2)$ operations. If N_x, N_y, and N_z are primes, the cpu time scales as $O(N_x^2 N_y N_z) + O(N_x N_y^2 N_z) + O(N_x N_y N_z^2) \sim O(N_L^{4/3})$.

Note: 1. Use of the FFT is not limited to homogeneous solids, since the A_{ij} do not depend on the potentially position-dependent polarizabilities α_j. 2. The method is not limited to brick-shaped solids: an arbitrary shape can be represented by zeroing the polarizations at lattice sites that lie outside its boundary before evaluating $\hat{\mathbf{P}}$. 3. Evaluation of $\mathbf{A} \cdot \mathbf{X}$ by FFTs is formally exact, and is probably less sensitive to round-off errors than direct evaluation because it requires fewer operations per lattice site. 4. Since $\mathbf{A}$ is symmetric, the product $\mathbf{A}^\dagger \cdot \mathbf{X}$ required by the CG can be obtained directly from $\mathbf{A}^\dagger \cdot \mathbf{X} = (\mathbf{A} \cdot \mathbf{X}^*)^*$.

Many applications of the CG and FFT algorithms to electromagnetic scattering problems have appeared in the engineering literature during the past five years (Peterson et al., 1991). Most of this work concerns scattering from conducting bodies, such as antennas and radar targets. The CG-FFT method appears to be unknown to optical physicists and astrophysicists working with the DDA, however.

The FORTRAN implementation requires storage for a total of $\approx 51 N_L$ complex numbers. Each scalar element of $\mathbf{A}'_i$ is either symmetric or antisymmetric under a change of sign in any component of i, and each 3×3 block is internally symmetric. Because $\hat{\mathbf{A}}'$ inherits these symmetries, it can be represented by $6(N_x + 1)(N_y + 1)(N_z + 1)$ complex numbers. Since $\hat{\mathbf{A}}'$ does not change between CG iterations and is independent of the direction of k and of the polarization of $\mathbf{E}_{inc}$, it is computed only once for each k. In order to obtain the total scattering and absorption cross sections averaged over orientation, it is necessary to solve (3.2.1) for two polarizations at each of several directions for k.

The accuracy to which an estimate $\mathbf{P}_i^{(n)}$ is a solution of (3.2.1) may be measured by the fractional error $err^{(n)}$, the r.m.s residual in (3.2.1) per occupied site divided by $|\mathbf{E}_0|$.

Table 3.3: Number of iterations required for a cube

Target Properties				Size Parameter $x = 2\pi a/\lambda$					
m	$|m - 1|$	$|\epsilon - 1|$	N	1	2	3	5	7	10
$1 + 0.1i$	0.10	0.20	512	2	3	4	5	6	7
$1.1 + 0i$	0.10	0.21	512	3	4	5	7	8	11
$1.33 + 0.01i$	0.33	0.77	512	6	9	10	16	29	62
$1 + i$	1.00	1.00	512	7	8	11	22	30	42
$1 + i$	1.00	1.00	4096	7	8	11	22	31	45
$2 + 0i$	1.00	3.00	512	18	34	54	125	270	626
$3 + 4i$	4.47	25.30	4096	73	69	81	148	222	336

Table 3.3 shows the number of iterations n necessary to achieve $\mathrm{err}^{(n)} < 10^{-3}$, for cubical targets with different refractive indices m and for different values of the scattering parameter $x \equiv ka$, where $a \equiv (3V/4\pi)^{1/3}$ is determined by the target volume V. In all cases we took $\mathbf{P}_i^{(0)} = 0$ for the starting point. Evidently, n is an increasing function of both $|\epsilon - 1|$ and x. However, n does *not* appear to depend significantly on N. Fig. 3.3 shows, for a cubical target, the cpu time per iteration as a function of N. Times are shown for Sun 4/65 and IBM 6000/320 computers, and for two different public-domain FORTRAN FFT routines (due to Brenner and Temperton). The cpu time per iteration increases approximately as $N \ln N$. Brenner's FFT routine works for any N, but is especially efficient when N_x, N_y, N_z are powers of two. Temperton's routine requires that N_x, N_y, N_z be products of 2, 3, and 5, so the target must be "embedded" in a lattice with this property.

Fig. 3.3, together with Table 3.3, can be used to estimate the cpu time required to obtain a DDA solution for one incident direction and polarization state. Once the solution $\mathbf{P}_i$ is obtained, an additional $O(N)$ operations are required to compute the scattering in any particular direction; if many scattering angles are required, the cpu time consumed by the scattering calculations may be appreciable. The scattering amplitude for any particular scattering direction (cf. eq. 3.12 of Draine (1988)) is simply a Fourier transform of the $\mathbf{P}_i$, and hence in principle could be obtained by interpolation on the (previously computed) $\hat{\mathbf{P}}_i$.
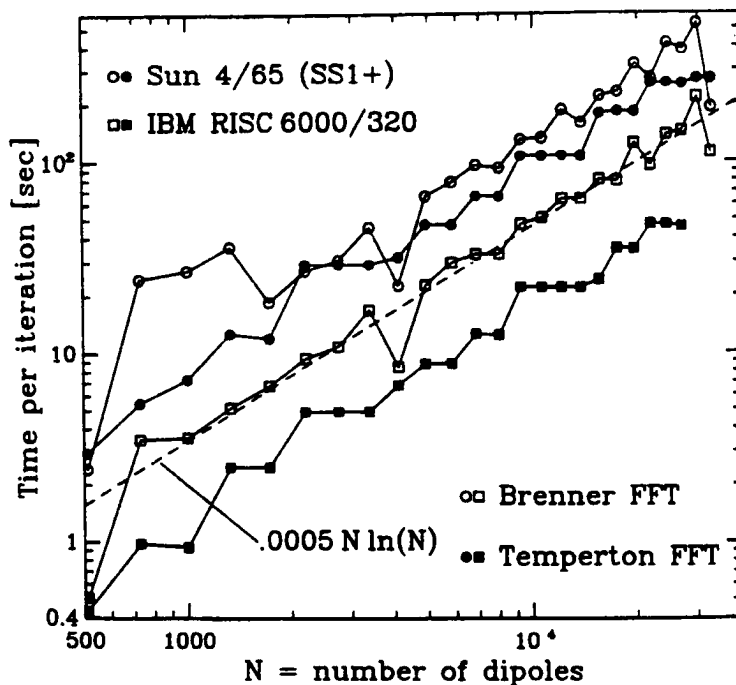
Figure 3.3: CPU time per iteration for cubes represented by different numbers of dipoles for two different computers and two different FFT routines.

3.7 Summary

We show that the matrix equation in the DDA approximation is governed by a symmetric BT matrix and we exploit the properties of such matrices in the solution of the "DDA equation" by using block-Toeplitz or FFT techniques. Particular advantages of the algorithms used in this study are that: (1) the requirements for storage of the DDA matrix on a computer are significantly reduced over the more general case; (2) the full inverse of the DDA matrix can be constructed from just two block columns; (3) CPU time requirements for large N are far less than for direct solvers. These numerical savings are especially relevant to the DDA and to the problem of orientational averaging.

Chapter 4

VALIDATION OF THE DISCRETE DIPOLE APPROXIMATION

4.1 Introduction

It is a constant source of amazement how relatively few exact solutions of Maxwell's equations are in existence. An arbitrary cluster of spheres (Bruning and Lo, 1969; Borghese et al., 1979; Fuller, 1991; Mackowski, 1991; Hamid et al., 1990) can be solved using the multipole expansion method. This provides an independent test of scattering by irregular particles.

In the recent report Wiscombe and Mugnai (1986) they state: "Of great interest, perhaps, is the solution ... for an arbitrary cluster of spheres; indeed, it seems to ... (Wiscombe and Mugnai) that sphere clusters would be excellent archetype for general nonspherical particles. Apparently, however, the solution ... is nightmarish to put into practice". In agreement with this quote we use a cluster of spheres for testing the DDA. It seems that the practical part has been recently improved, (see review by Fuller, 1991). Using a modified version of work by Mackowski (1991) we were able to solve for a relatively large cluster of spheres. In this section, a single and two sphere multipole solution are used to test the discrete dipole approximation. Such comparisons are needed to:

- find the number of dipoles needed to model correctly the shape of a particle in the DDA approximation,

- to decide on numerical convergence criteria, and

- to find a proper dipole polarizability scheme by correcting the Clausius-Mossoti relationship
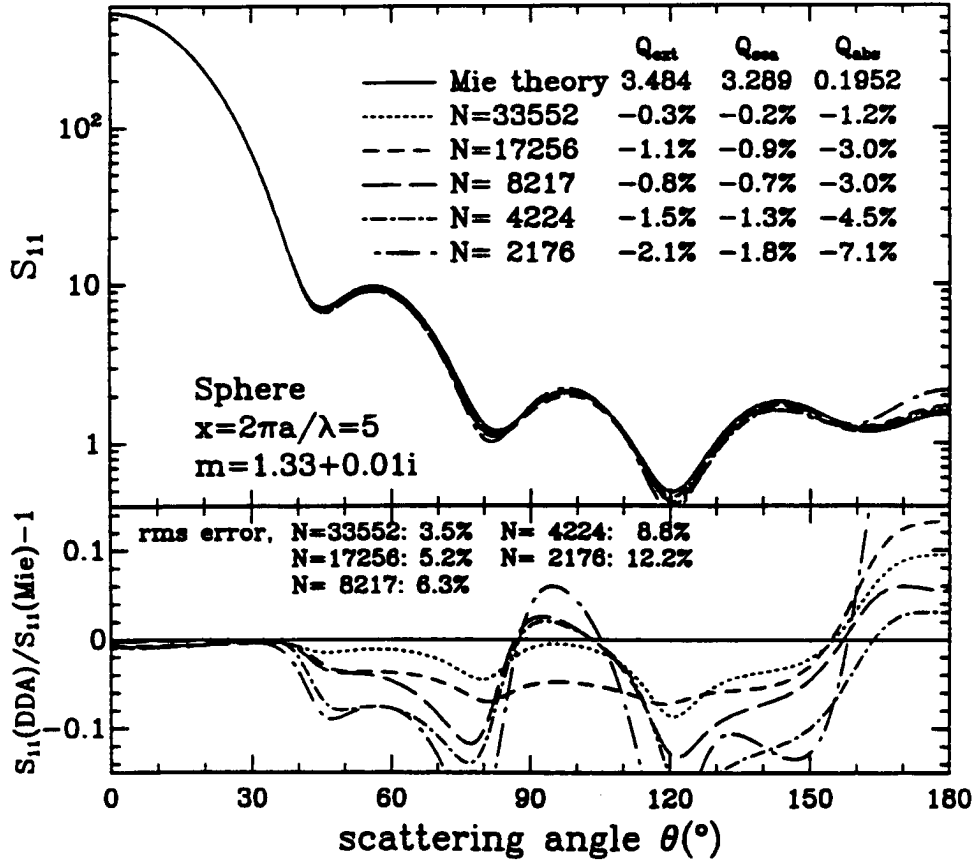
Figure 4.1: [Scattering by a sphere with refractive index $m = 1.33 + 0.01i$ for $x = ka = 5$.] Scattering by a sphere with refractive index $m = 1.33 + 0.01i$ for $x = ka = 5$. Exact results for S_{11} are compared with S_{11} results computed using the DDA with different number of dipoles N.

Also, since the DDA solution often involves iterative solution to a linear problem with matrices of the 10^5 order, it reassuring to see that the method compares well with the exact or independent solution.

4.2 The single sphere comparison

Comparisons of the exact solution for scattering by a sphere with DDA results using different values of N for size parameters $x = 5, 10$ and 15 are presented in this section. The scattering matrix element S_{11} for unpolarized light is shown, for refractive index $m = 1.33 + 0.01i$ and scattering parameter $x = 5, 10$, and 15, in Figs. 4.1, 4.2, and 4.3, respectively. Also shown is the relative error in S_{11} as a function of scattering angle θ; note that the relative error is rather uniformly distributed over θ. In Figure 4.4 we show results
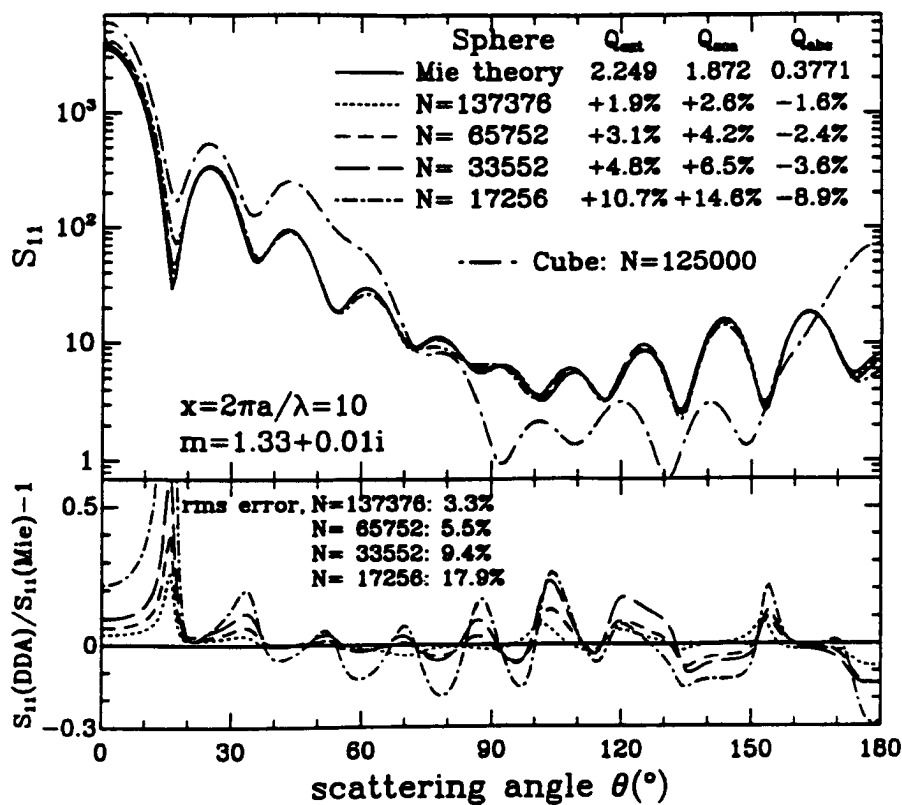
Figure 4.2: Same as Fig. 4.1 but for x=10.
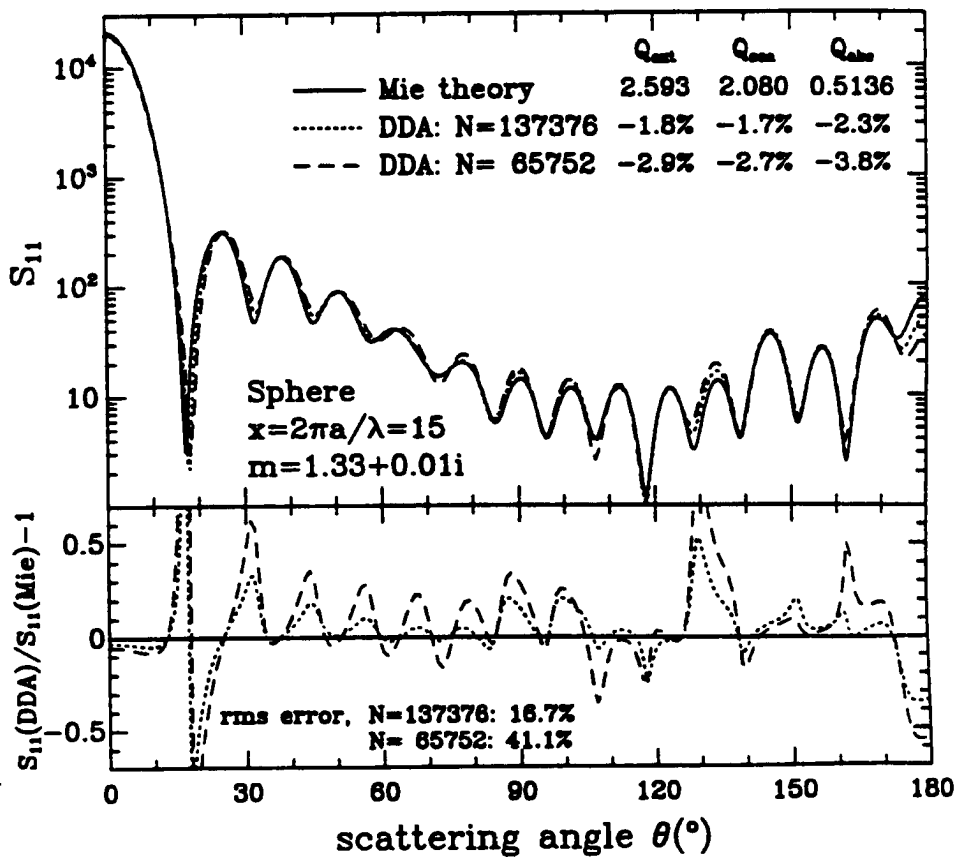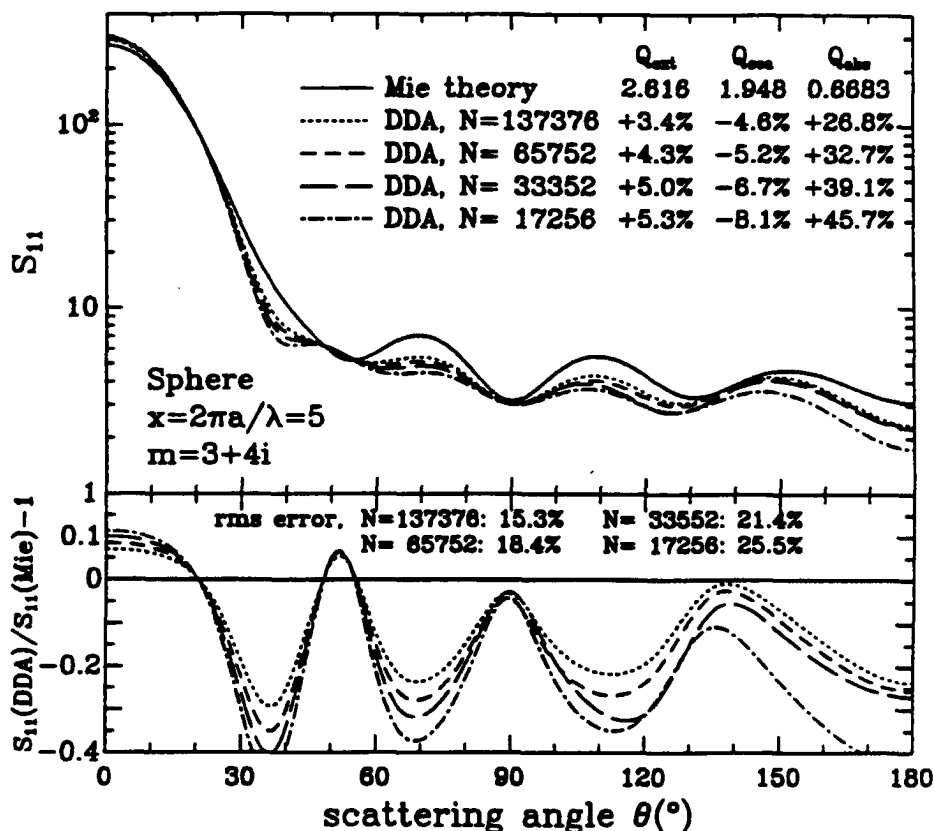

Figure 4.3: Same as Fig. 4.1 but for x=15.

Figure 4.4: Same as Fig. 4.1 but for x=20.

for $m = 3 + 4i$ and $x = 5$. In Figs. 4.1-4.4 we also give, for each N, the fractional errors in the efficiency factors Q_{ext}, Q_{sca} and Q_{abs} for extinction, scattering and absorption, and the rms value of the relative error in S_{11} (averaged over scattering directions). In Fig. 4.2 we also show the computed S_{11} for radiation incident normal to one of the faces of a cube represented by 125000 dipoles. The overall scattering pattern evidently deviates quite appreciably from the solution for a sphere.

For $m = 1.33 + 0.01i$ (with $|\epsilon - 1| \approx 0.77$) accuracies of $\sim 5\%$ in Q_{ext}, Q_{abs} and Q_{sca} are achieved, for $x = 10$, with $N \approx 3 \times 10^4$ dipoles; similar accuracies are achieved for $S_{11}(\theta)$ with $N \approx 7 \times 10^4$. Comparison of Figs. 4.1 and 4.4 shows that the number of dipoles required to achieve a specified accuracy scales approximately as $|m|^3 x^3$, as suggested by Draine (1988). Figs. 4.1-4.4 also support the suggestion that, for fixed m and x, the errors scale approximately as $N^{-1/3}$.

4.3 Two-spheres

Several investigations (Bruning and Lo, 1969; Borghese et al., 1979; Fuller, 1991; Mackowski, 1991; Hamid et al., 1990) have been conducted into the general solution to Maxwell's wave equation for clusters of spheres. The analysis involves a superposition technique, in that the total solution for the field external to a particle is constructed from a superposition of individual solutions. To satisfy the boundary conditions on each sphere, addition theorems are used to transform a spherical harmonic from one coordinate system to another. [1] Such formulation leads to a set of linear equations for the expansion coefficients of the individual solutions. In matrix form the the system of equations is expressed

$$\mathbf{a}^i + \Sigma_{j=1,j\neq i}^{N_s} \mathbf{T}^{ji} \mathbf{a}^j = \mathbf{p}^i \qquad (4.3.1)$$

where **a** define scattered field coefficients for sphere i, $\mathbf{p}^i$ define incident field coefficients for sphere i, and $\mathbf{T}^{ji}$ represents the translation matrix from sphere j to i, N_s is number of spheres. The size of **a**, **p**, and **T** depends on the order of multipole expansion. Far-field scattering and cross sections are determined by a. A detailed account has been given by Mackowski (1991). An efficient solution technique is the order of scattering method developed by Fuller and Kattawar (1988). This method is block iterative solver for linear system of eqs (4.3.1). Our numerical experiments indicate that the bi-conjugate gradient method offers faster convergence rate. Also, spatial invariance (FFT) can be used for certain configurations of spherical clusters. Numerical issues aside, an exact solution for multiple spheres using multipole expansion offers a unique possibility to compare our DDA implementation with the independent solution for a non-spherical targets. Fig. 4.5 and 4.6 shows two pseudo-spheres in contact resolved on 32 × 32 × 32 dipole grid for each of the spheres.

---

[1] Incidentally, the same method is employed in cloud microphysics when finding hydrodynamic forces between two droplets . Hocking (1959) was the first to use the addition theorem for spherical harmonics to get the collision efficiency of two small drops falling under gravity in still air.
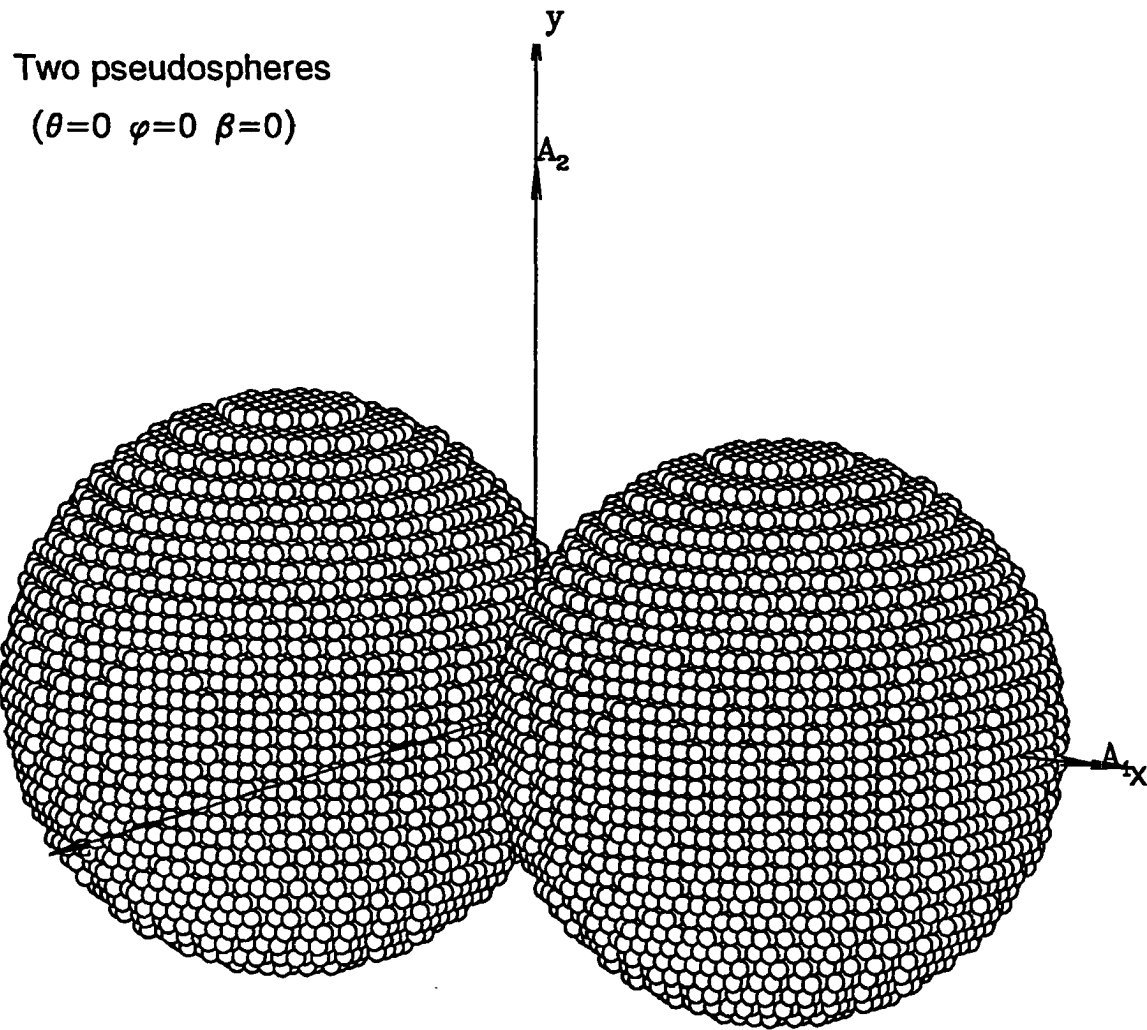
Figure 4.5: Two pseudo-spheres composed of $2 \times 32 \times 32 \times 32$ point dipoles. Light is travelling along x-axis.
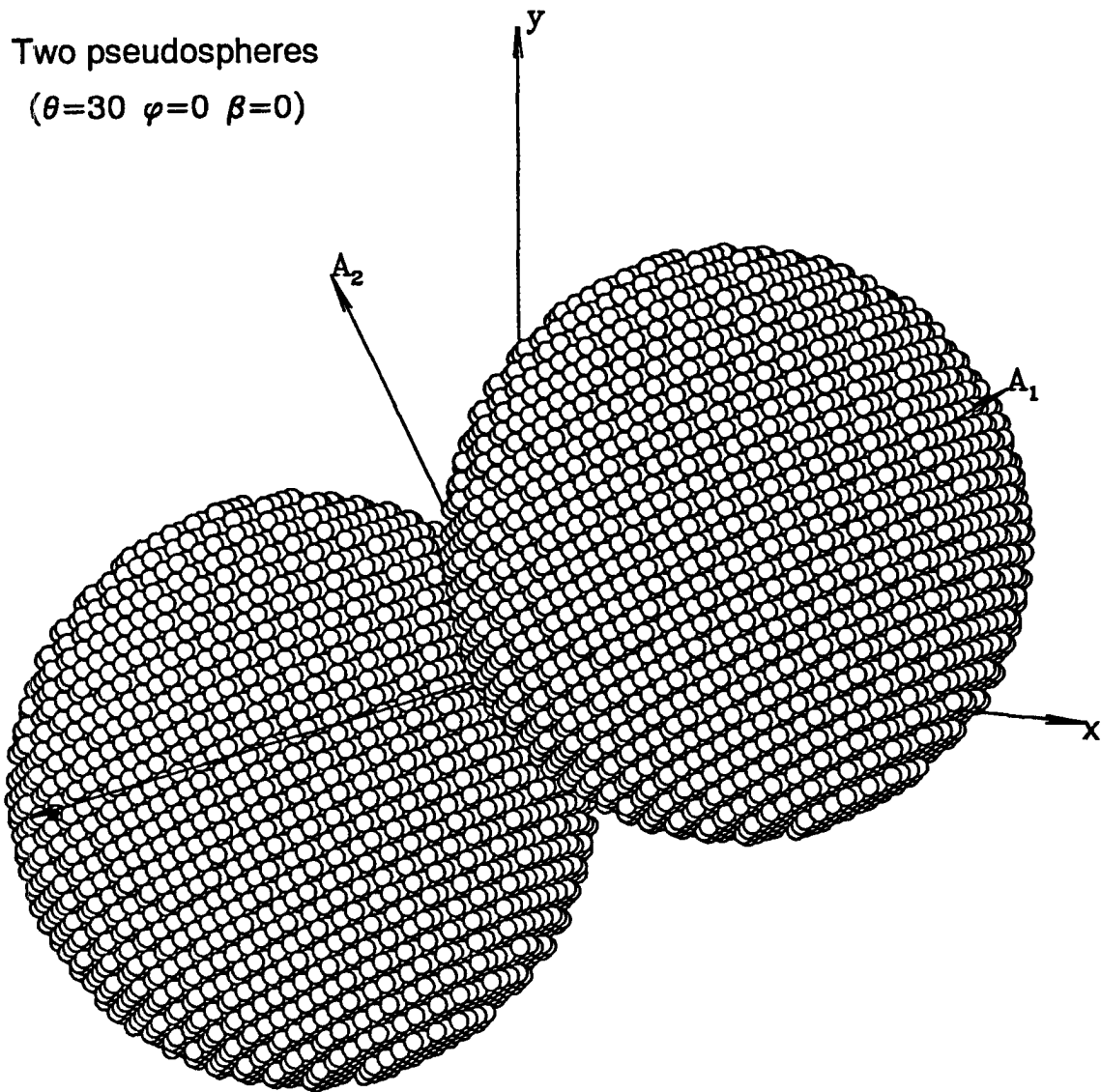
Two pseudospheres

(θ=30 φ=0 β=0)

Figure 4.6: Same as in 4.5 but rotated ($\theta = 30$).

We have compared the exact solution for scattering by two spheres (solid line) in contact with DDA (crosses) for $m = 1.33 + 0.001i$ and a scattering parameter $x = 5$ and $x = 10$ in Figs. 4.7 and 4.8, respectively. DDA matches the exact solution very well although significant errors are observed in side- and back-scatter. In the next section we perform more quantitative error analysis by showing fractional error plots for several values of equivalent size parameter.

4.4 Choice of polarizability definition. Comparisons with two-sphere cluster

Since DDA results depend directly upon the dipole polarizabilities, it is important to determine the optimal method for choosing them. Recently Draine and Goodman (1992) established a new prescription for the dipole polarizabilities by solving a closely-related problem: choosing the dipole polarizabilities such that an *infinite* lattice of point dipoles will propagate electromagnetic plane waves with the same dispersion relation as a medium of specified dielectric function ϵ (LDR method).

In order to compare their new prescription for α with those proposed previously, they report the results of extensive DDA calculations for absorption and scattering by single spheres, and compare exact Mie theory results with DDA calculations. They find that for moderate $|\epsilon - 1|$ their prescription for the dipole polarizabilities generally provides more accurate results for scattering and absorption by spheres; this superiority is presumed to extend to nonspherical targets.

The unique aspect of this prescription, which they were not able to test thoroughly, is that it depends not only on the refractive index m but also on the direction of propagation and the polarization state. In this section we extend their analysis to exact solution for non-spherical particle composed of two spheres in contact. We conclude that indeed the DDA calculations of absorption and scattering should use the LDR-based prescription for the dipole polarizabilities.

The Draine and Goodman (1992) polarizability can be written as

$$\alpha = \frac{\alpha^{(nr)}}{1 - (2/3)i(\alpha^{(nr)}/d^3)(k_0 d)^3} \tag{4.4.1}$$
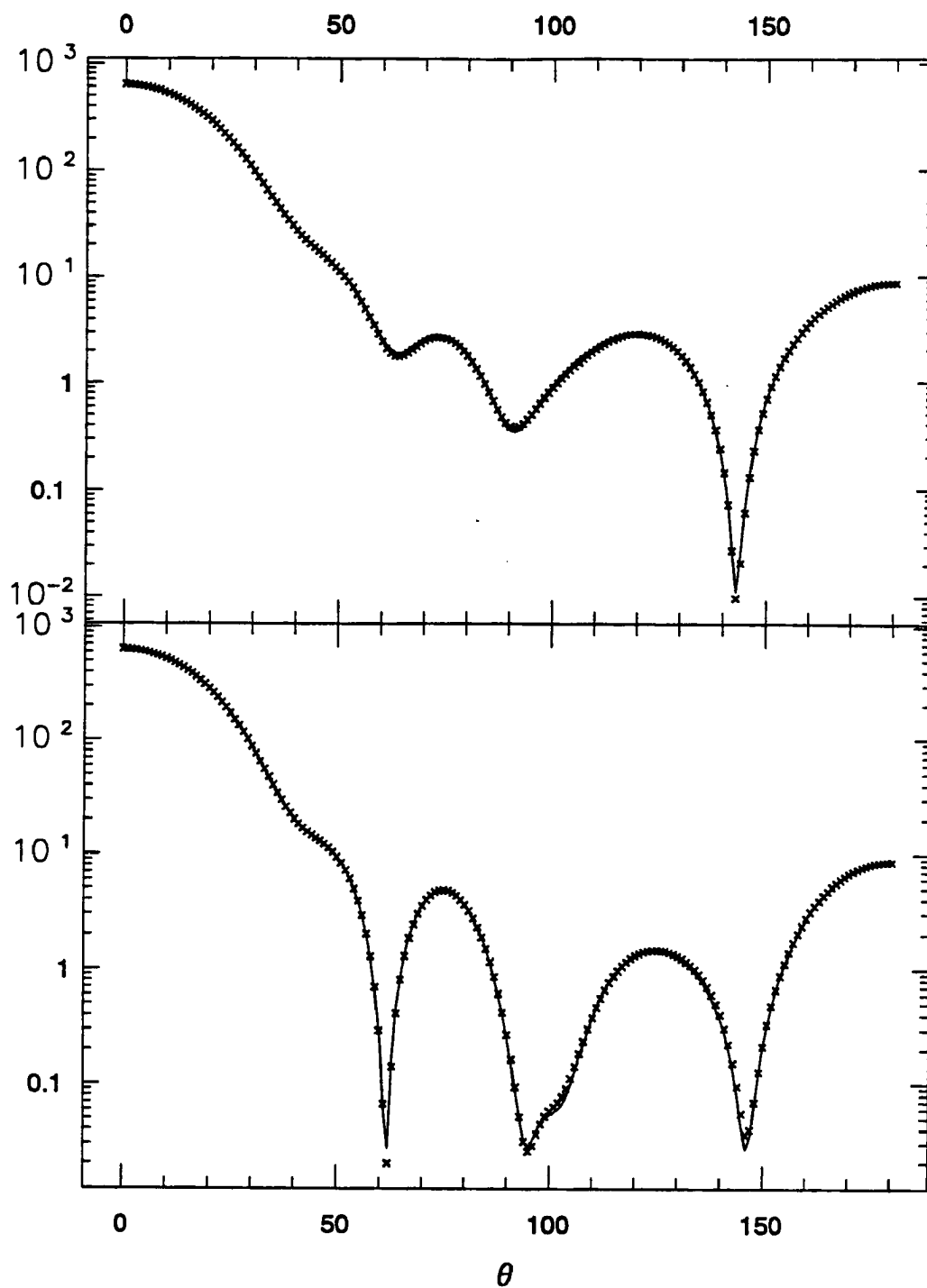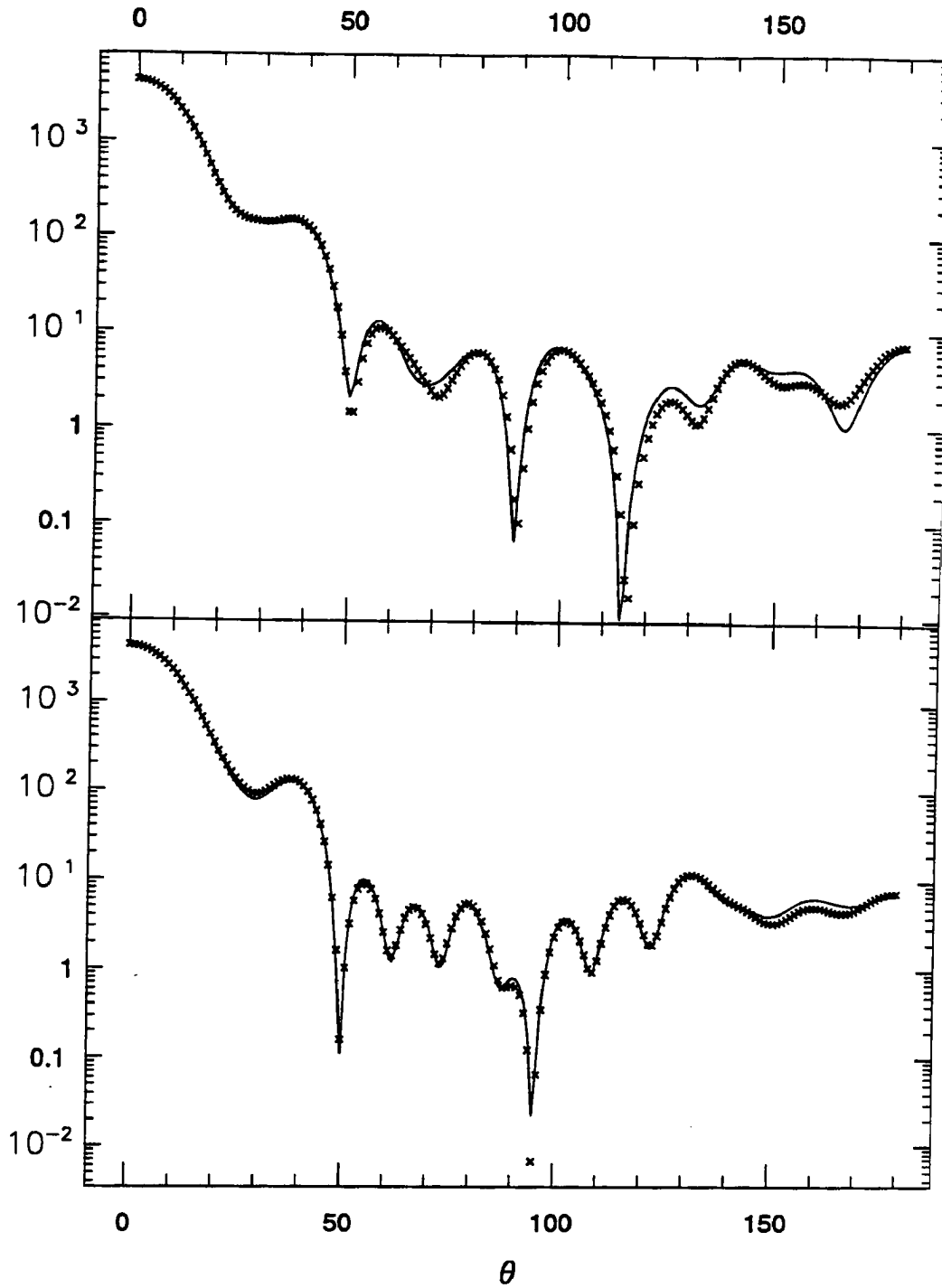
N=34512 r$_{eff}$=5.00000 (1.3300 .0010),

Figure 4.7: [Scattering by a sphere with refractive index $m = 1.33 + 0.01i$ for $x = ka = 5$.] Scattering by a sphere with refractive index $m = 1.33 + 0.01i$ for $x = ka = 5$. Exact results for S_{11} and S_{22} are compared with S_{11} and S_{22} results computed using the DDA for $x = 5$.

$N=34512$ $r_{eff}=10.00000$ $(1.3300$ $.0010)$,

Figure 4.8: Same as in Fig. 4.7 but for $x = 10$.

with

$$\alpha^{(nr)} \approx \frac{\alpha^{(0)}}{1 + (\alpha^{(0)}/d^3)\left[b_1 + m^2 b_2 + m^2 b_3 S\right](k_0 d)^2} \tag{4.4.2}$$

$$b_1 = c_1/\pi = -1.8915316 \tag{4.4.3}$$

$$b_2 = c_2/\pi = 0.1648469 \tag{4.4.4}$$

$$b_3 = -(3c_2 + c_3)/\pi = -1.7700004 \tag{4.4.5}$$

with $\alpha^{(0)}$ given by the "Clausius-Mossotti" polarizability (e.g., Jackson 1975)

$$\alpha_i^{(0)} \equiv \frac{3d^3}{4\pi}\left(\frac{m_i^2 - 1}{m_i^2 + 2}\right) \tag{4.4.6}$$

where m_i is the refractive index at lattice site i. The dependence on direction and polarization enters solely through the quantity S.

There are two other choices of polarizability used in the current literature on the subject. Goedecke and O'Brien (1988) and Hage and Greenberg (1990) showed that the fundamental DDA equation can be derived from a simple discretization of an integral formulation of the scattering problem – the "DGF/VIEF" method. These authors concluded that the dipole polarizabilities should be given by

$$\alpha_i \approx \frac{\alpha^{(0)}}{1 + (\alpha_i^{(0)}/d^3)[b_1(k_0 d)^2 - (2/3)i(k_0 d)^3]} \tag{4.4.7}$$

or, to the same order of accuracy, the "non-radiative" polarizability is

$$\alpha_i^{(nr)} = \frac{\alpha_i^{(0)}}{1 + (\alpha_i^{(0)}/d^3)b_1(k_0 d)^2} \tag{4.4.8}$$

where

$$b_1 = -(4\pi/3)^{1/3} = -1.611992 \tag{4.4.9}$$

Using the optical theorem, Draine (1988) showed that when $k_0 d$ was finite the polarizabilities α_i should include a radiative-reaction correction:

$$\alpha_i = \frac{\alpha_i^{(nr)}}{1 - (2/3)i(\alpha_i^{(nr)}/d^3)(k_0 d)^3} \tag{4.4.10}$$

Figures 4.9-4.10 presents comparison of a two sphere, multipole solution with the DDA. Results are shown for three different prescriptions for the dipole polarizabilities:

CMRR (Clausius-Mossotti plus Radiative Reaction), VIEF (Volume Integral Equation Formulation, and LDR (Lattice Dispersion Relation) as functions of size parameter $x = k_0 a_{eff}$. Refractive index $m = 1.33 + 0.01i$ is used and the dipoles are placed on $2 \times 32 \times 32 \times 32$ cubic lattice. Fig. 4.9 is for the "endfire" configuration of two spheres as in Fig. 4.5. Fig. 4.10 is for $\theta = 30$ which corresponds to the configuration in Fig. 4.6. The light is propagating along the x-axis and is unpolarized. In both cases the LDR method is superior to DGF/VIEF and CMRR for a broad range of size parameter values. For the $\theta = 30$ case the LDR method gives excellent agreement indicating that the directional corrections in (4.4.1) are indeed improving the results.

Figures 4.9-4.10 presents comparison of a two-sphere multipole solution with the DDA for the same physical parameters but for $x = 5$ and as functions of θ. Again, the LDR is consistently better in comparison to two other schemes. The fractional error for scattering efficiency (Fig. 4.11) is close to 1% in comparison with the multipole solution, and for absorption efficiency (Fig. 4.12) the error is less then 3%.

4.5 Summary

This chapter establishes DDA as a sound and exact method to study scattering by irregular particles. The choice of the polarizability scheme is justified on the basis of the multipole solution for a cluster of two spheres in contact. Results show that the DDA, together with the CG-FFT algorithm, makes possible accurate calculations of scattering and absorption by dielectric targets with size parameter x as large as $20 - 30$. This last limit is of computational nature and is not related to the stability of the method.
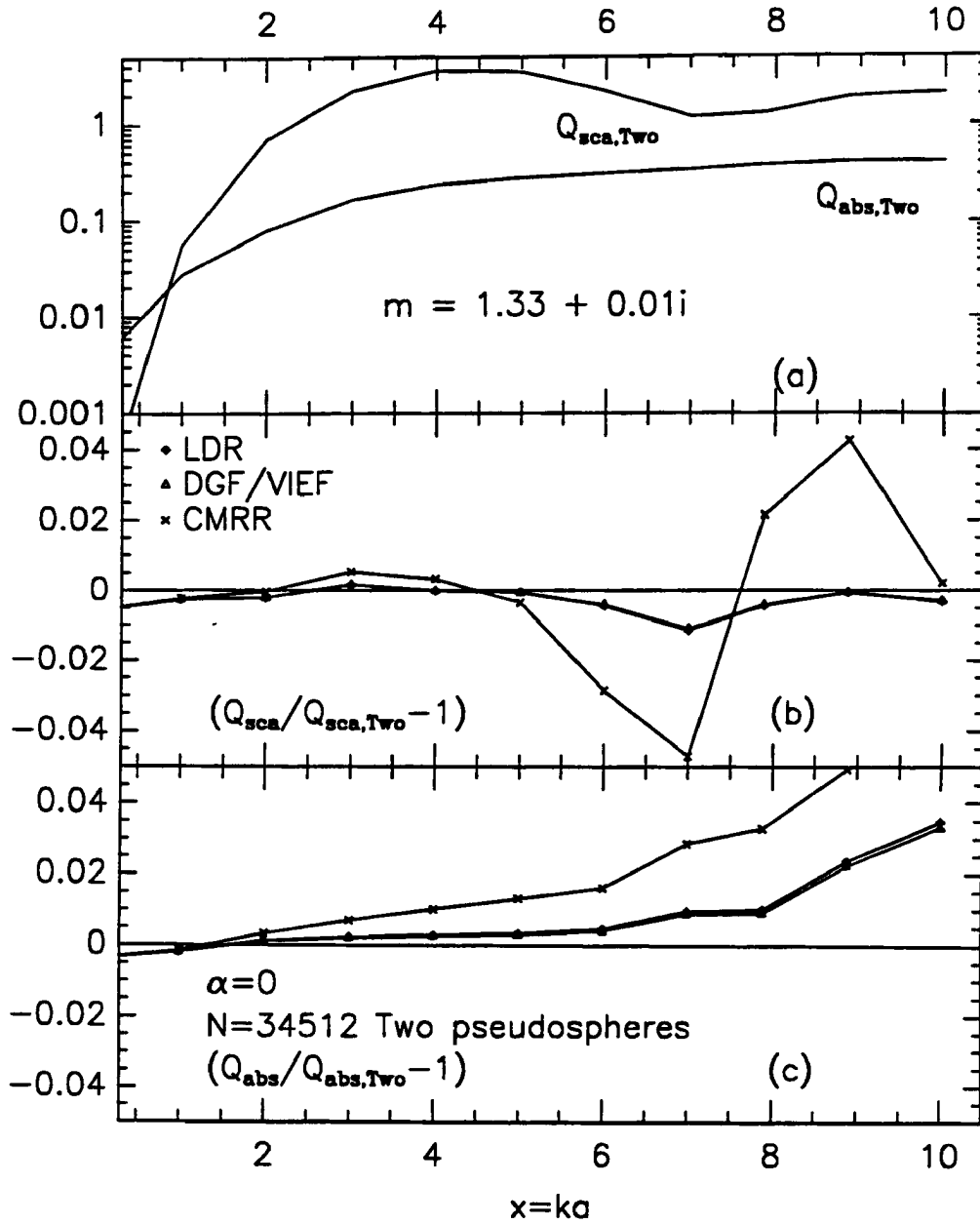
Ver.4b TWOSPH 34512 (1.330, .1000E-01)

Figure 4.9: (a) Q_{sca} and Q_{abs} for two spheres of refractive index $m = 1.33+0.01i$ (b) and (c) Fractional error in computed value of Q_{sca} and Q_{abs} for the N=34512 two pseudo-spheres in contact. Results are shown for three different prescriptions for the dipole polarizabilities: CMRR (Clausius-Mossotti plus Radiative Reaction); VIEF (Volume Integral Equation Formulation); and LDR (Lattice Dispersion Relation) as functions of $x = k_0 a_{eff}$.
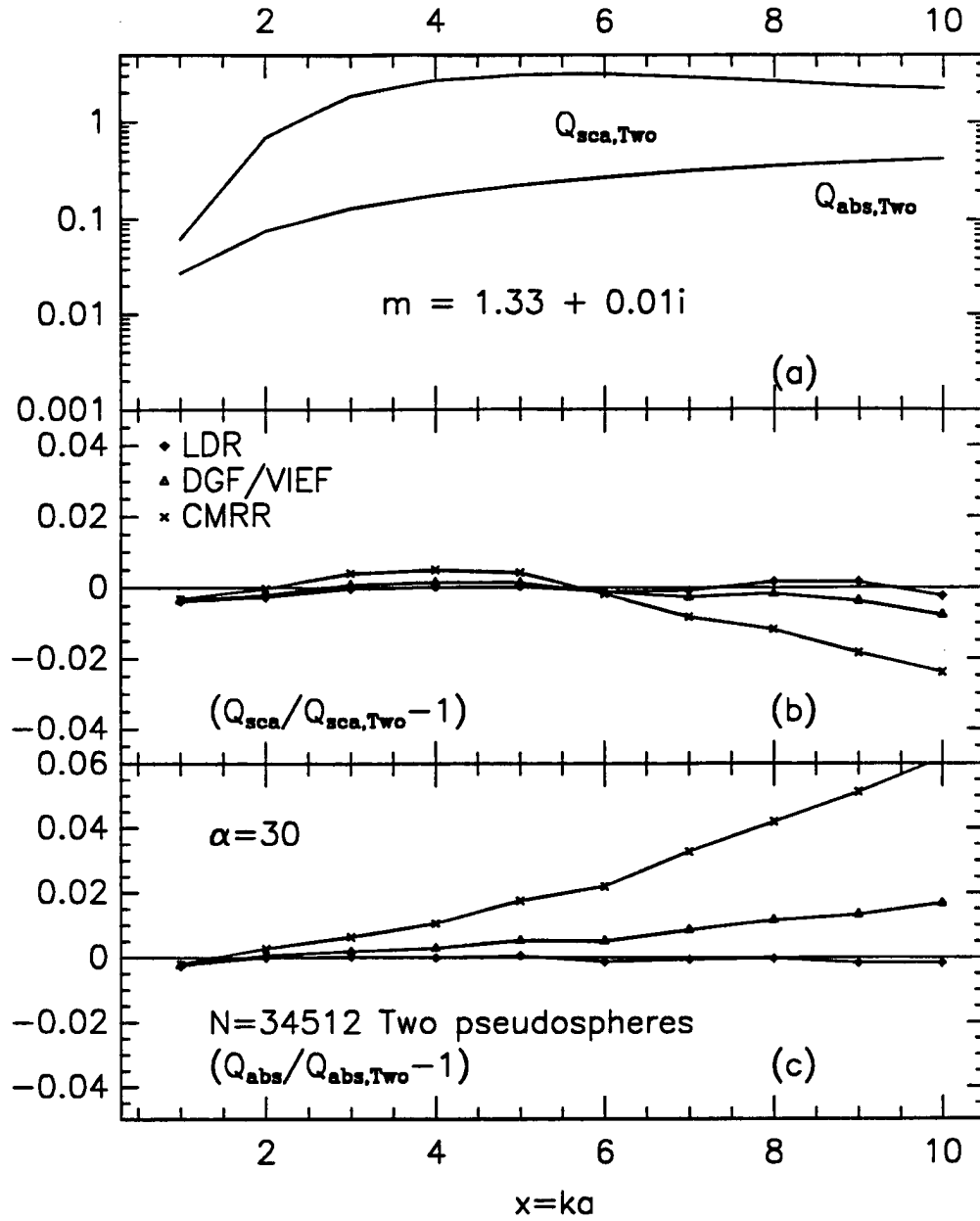
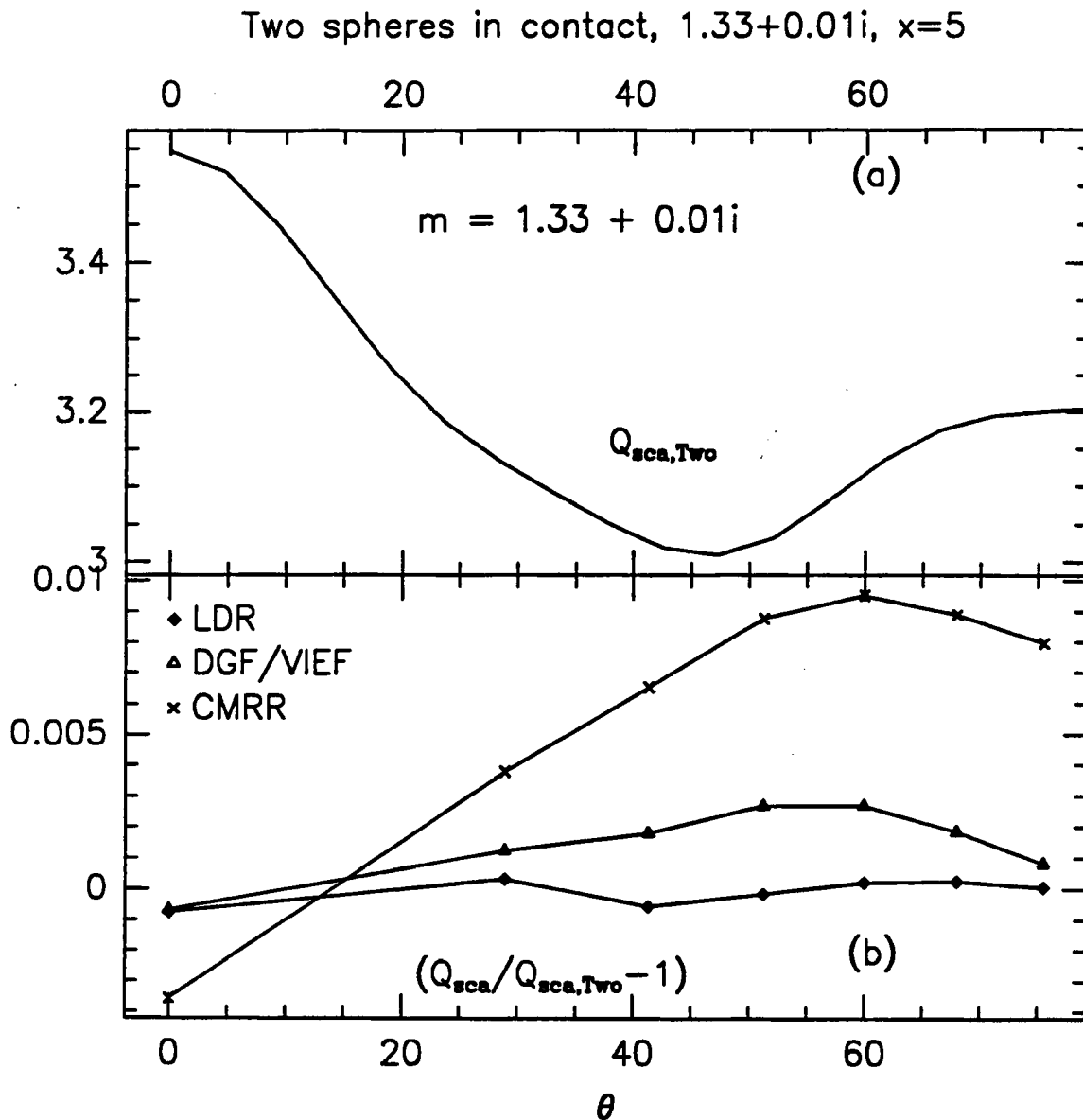Figure 4.10: Same as in Fig. 4.9 but for $\alpha = 30$.

Figure 4.11: (a) Q_{sca} for two spheres in contact of refractive index $m = 1.33 + 0.01i$ (b) Fractional error in computed value of Q_{sca} for the two pseudospheres (the N=34512) Results are shown for unpolarized light for three different prescriptions for the dipole polarizabilities: CMRR (Clausius-Mossotti plus Radiative Reaction); VIEF (Volume Integral Equation Formulation; and LDR (Lattice Dispersion Relation) as functions of angle θ.
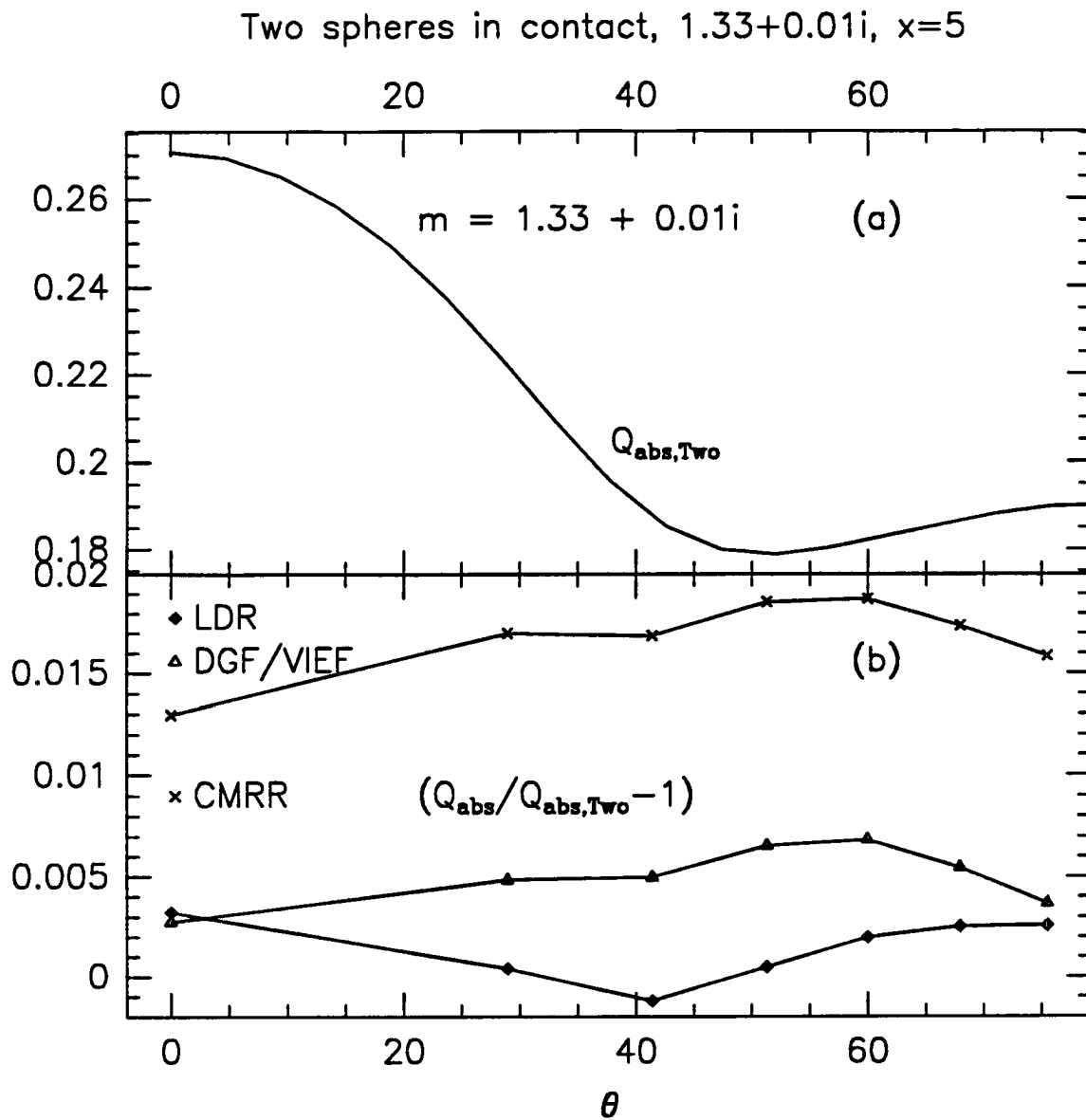
Figure 4.12: Same as in Fig. 4.11 but for Q_{abs}.

Chapter 5

SCATTERING ON ICE CRYSTALS

In this chapter we provide some results on exact scattering calculations by ice crystals. Keeping in mind meteorological applications of this work we limit ourselves to particles typical for upper tropospheric cirrus clouds. Since the ultimate applicability of the research described in this thesis is to the radiative transfer codes in large numerical models, we discuss only the "bulk" type characteristics, such as asymmetry parameter and extinction efficiencies since these are directly incorporated into radiative transfer models. With these apparent limitations the "parameter space" remains formidable.

5.1 Polyhedral and irregular ice crystals

A great variety of growth forms of snow crystals is observed. Nakaya (1954) was the first to study the relation between the form of ice crystals and environmental temperature T and supersaturation σ with respect to ice. Since then many experimental studies of growth patterns have been made and consolidated in a (T, σ) diagram (Kobayashi, 1961) (Fig. 5.1). This diagram shows that the habit change from plates to columns depends primarily on temperature. Morphological instability of polyhedral crystals occurs with an increase of the supersaturation. At low supersaturation polyhedral snow crystals can grow in a stable way. With increasing supersaturation, however, their patterns develop into sector plates, dendrites, or needles (Yokoyama and Kuroda, 1990; Pruppacher and Klett, 1978). There is increasing evidence that the growth pattern depends not only on temperature and supersaturation but also on diffusivity and thermal conductivity of the atmosphere.
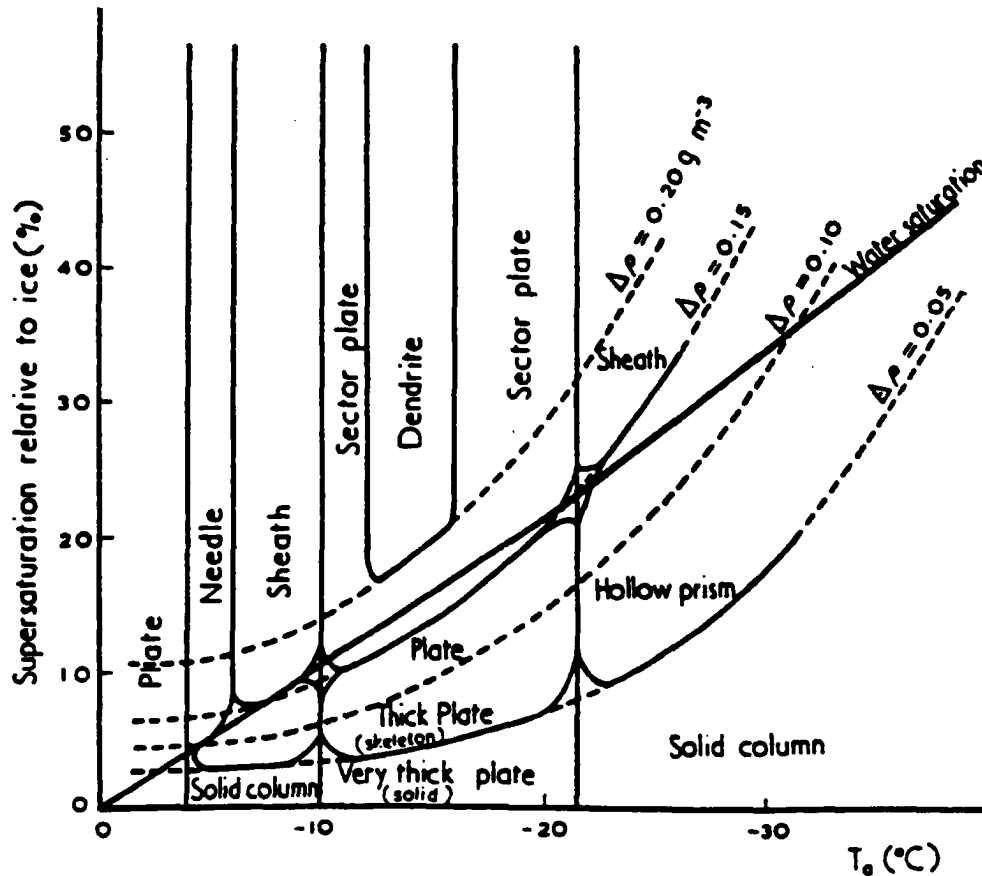
Figure 5.1: Habit changes and stability of polyhedral forms of snow crystals depending on temperature and supersaturation with respect to ice (after Kobayashi (1961)).

There are other simple polyhedral shapes (see Figure 5.2) including pentagonal, rhombic, trapezoidal, and triangular plates which are "peculiar" and not included in the classification in Figure 5.1. See Kikuchi and Hogan (1979) for more details about such diamond dust ice crystals.

Besides simple polyhedral forms, irregular crystals or combinations of simple shapes are common in nature. These include combination of bullets (Figure 5.3), hollow prisms (Figure 5.4), rimed snow crystals (Figure 5.5), polycrystalline crystals with spatial branches (Lee, 1972; Takahashi, 1979), or twined structures (Kobayashi et al., 1976).

Such crystals are often represented by spheres of equivalent volume in radiative transfer literature. This procedure is equivalent to melting of ice crystals and is well illustrated in Figure 5.6. Columns or hollow columns are often represented by infinite cylinders (Stephens, 1986). From this variety of shapes we provide some representative calculations.
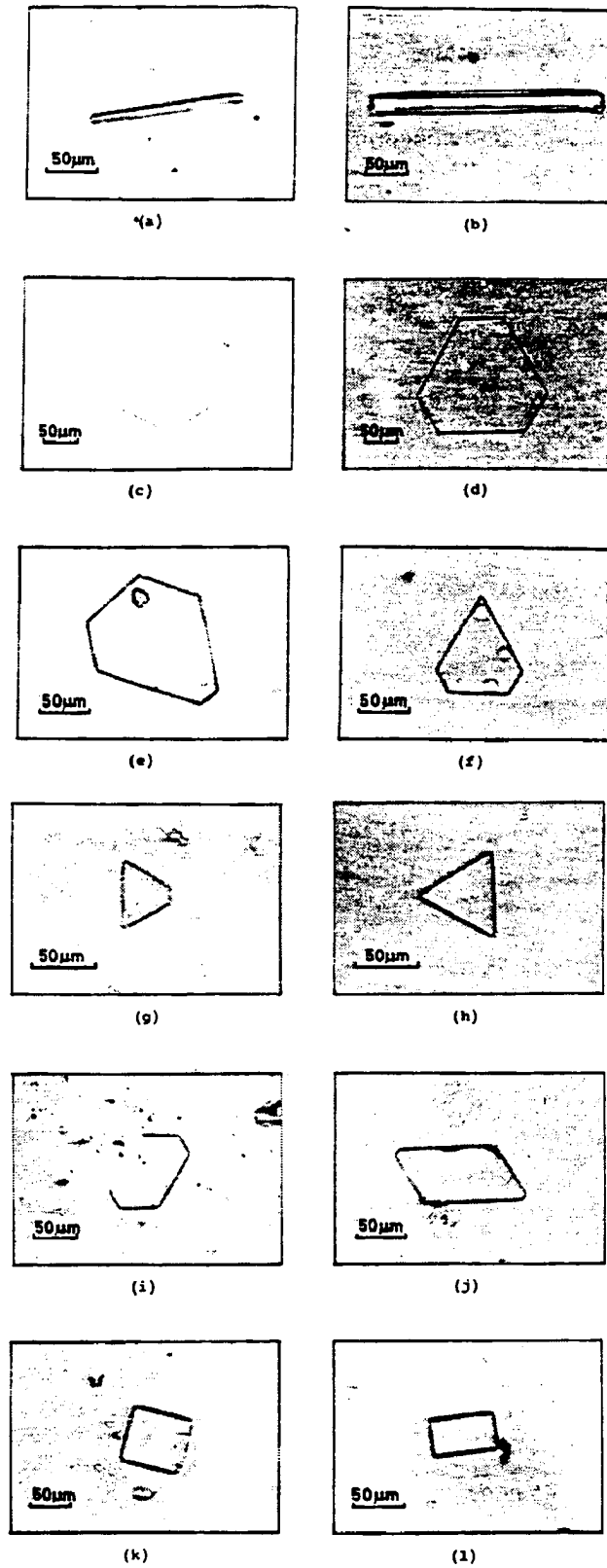
Figure 5.2: Typical shapes of diamond dust type ice crystals observed in summer season at Amundsen-Scott South Pole Station, Antarctica (after Kikuchi and Hogan (1979)).
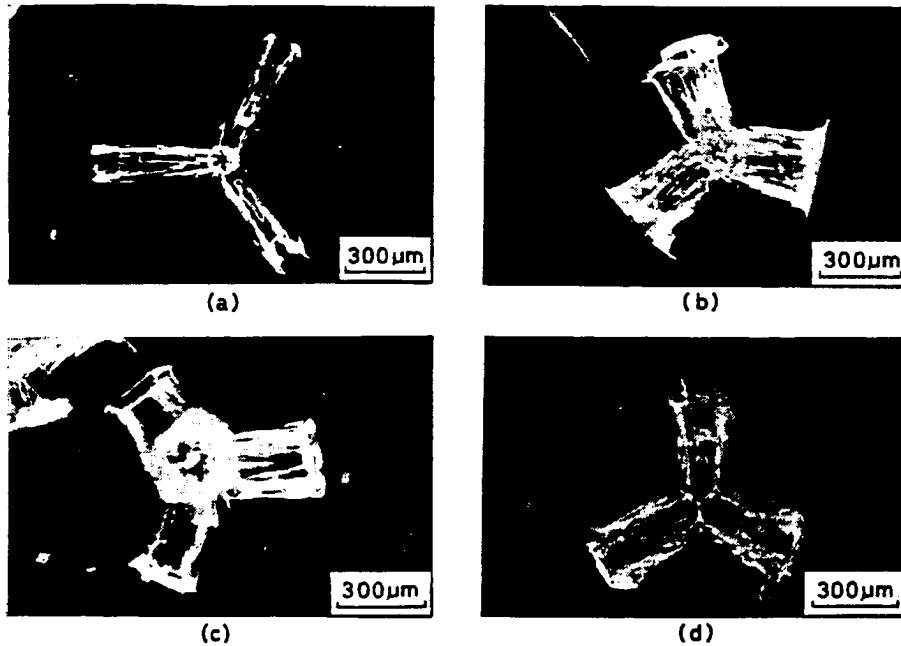
Figure 5.3: Examples of replicas of a combination of bullets (after Uyeda and Kikuchi (1979)).

The asymmetry parameter is studied for simple polyhedral shapes typical of high cirrus and small supersaturations with respect to ice. We also present scattering efficiencies for inhomogeneous particles.

5.2 The asymmetry parameter

The importance of asymmetry parameter to radiative transfer and climate was introduced in Chapter 2 and is also discusses by Liou (1974), Stephens (1980) and Minnis et al. (1992). Several accounts of numerical studies of the asymmetry parameter are available for irregular particles (Asano and Sato, 1980; Wiscombe and Mugnai, 1986; Kokodii, 1985; Cohen and Alpert, 1980). Asano and Sato (1980) state that the asymmetry parameter of randomly-oriented equivalent spheroids tends to be larger than that of the equivalent $g_{sphrd} > g_{sph}$. Opposite results were obtained by Pollack and Cuzzi (1980) who claim that $g_{irr} < g_{sph}$. They obtained smaller values of asymmetry parameters even for platelike particles than those for the volume equivalent spheres by choosing a parameter value of the forward scattering to backscattering ratio based on laboratory measurements. Examination of Wiscombe and Mugnai's (1986) results for particles described by Chebyshev
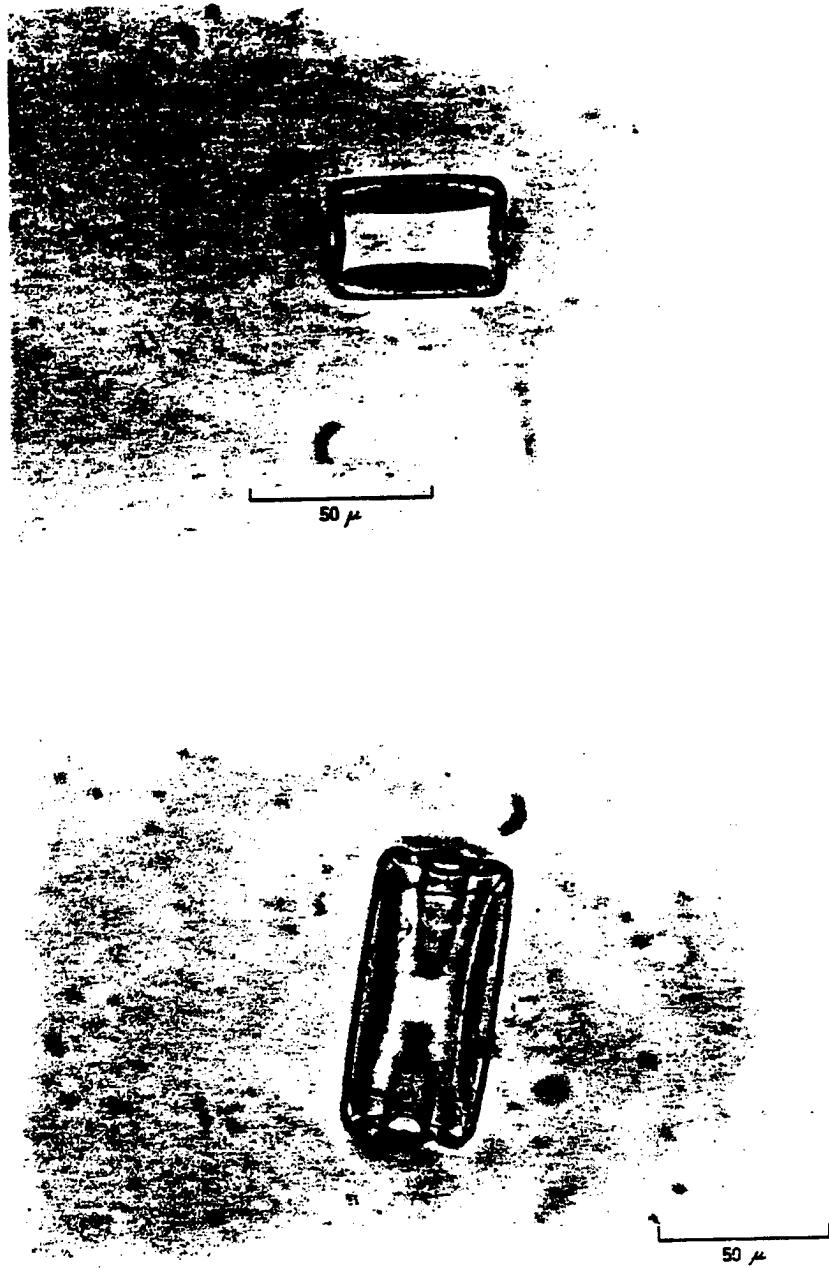
Figure 5.4: Replicas of a small ice crystals. (after Ono (1971)).

	Rimed crystal		Hexagonal graupel	Conelike graupel
Without tumbling (rotation)	Plane crystal	a_1	a_2	a_3
		b_1 Break off		b_2
		c_1		c_2
	Columnar crystal	d_1		d_2 x
	Radiating assemblage of plane branches	e_1		e_2 - ＊
	Frozen drop	f_1		f_2

	Rimed crystal		Lump graupel
With tumbling (rotation)	Columnar crystal	g_1	g_2 x
	Radiating assemblage of plane branches	h_1	h_2 ※
	Frozen drop	i_1	i_2 ※

Figure 5.5: Formation mechanisms of three kinds of graupel particles. (after Harimaya (1976)).

functions ("Chebyshev particles") shows that, in their case, $g_{che} \approx g_{sph}$. Liou (1974) states that the asymmetry parameter for spheres is consistently larger than that for scattering on cylinders, i.e. $g_{cyl} < g_{sph}$. Stephens (1980) derives some of the radiative properties of cirrus clouds in the infrared region on this basis. Stephens et al. (1989) state that $g_{irr} < g_{sph}$ on the basis of interpretation of radiative flux measurements from flights collected during the FIRE cirrus field project. The need to employ values of the asymmetry factor smaller that those values associated with spherical particles was also pointed out by Platt et al. (1980) in their bispectral analysis of satellite observations. Minnis et al. (1992) compare their effective emittance to results of Platt and Stephens (1980) .

before melting ⟶ after melting

before melting ⟶ after melting

100 μ
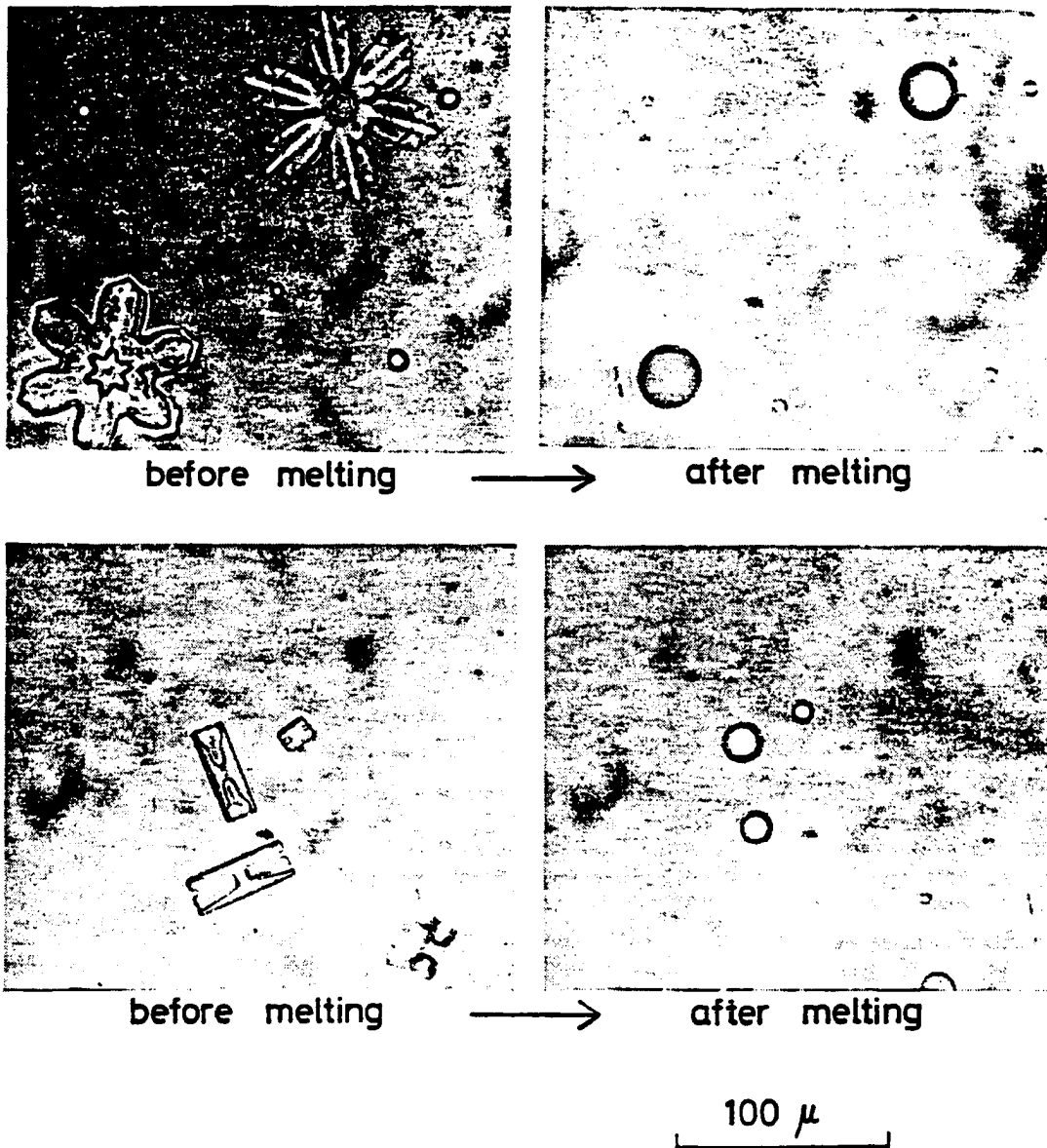
Figure 5.6: Ice crystals before and after being melted. (after Kajikawa (1973)).

They note that the most important factor driving the effective emittance differences between their results and those of Platt and Stephens (1980) is the choice of asymmetry parameter. They employ $g \approx 0.94$ in comparison to $g = 0.71 - 0.81$ used by Platt and Stephens (1980).

No definite picture emerges from perusal of available literature; not even the sign of $g_{irr} - g_{sph}$ is well understood. It is certain, however, that the asymmetry parameter is of primary importance to climate and radiation transfer studies.

5.2.1 Mie calculations

This section is devoted to discussion of the asymmetry parameter for spherical scatterers. After a short review of the subject a parameterization scheme for asymmetry parameter is introduced, similar in simplicity to expressions for efficiencies in Anomalous Diffraction Approximation (Chapter 7). The scheme provides a formulation which can be directly integrated for ensembles of particles defined by gamma size distribution. While the scheme is developed for spherical particles, it is argued that the form of the parameterization carries over to nonspherical particles. There are some reasons to expect that this is possible. Part of the analysis of the asymmetry parameter is of a general nature and not specific to particle shape.

Several accounts of numerical studies of the asymmetry parameter are available for spheres (Irvine, 1965; Hansen and Travis, 1974; Wiscombe and Mugnai, 1988; Shah, 1990). We follow and extend Kerker (1969) and van de Hulst (1980) expositions. The asymmetry parameter g, depends on particle composition (refractive index), its size, and shape. For a large particle the forward and near forward scattering determines g. The forward scattering depends on diffraction, external reflection, and transmission with two refractions (Asano and Sato, 1980). The diffraction part is independent of the refractive index but depends on shape and size. For large particles the diffracted component is in forward direction. Reflection and refraction depend on size and refractive index. When the refractive index is unity, there are no reflected rays and all of the radiation passes through the particle un-deviated. The results is that $g = 1$ (Kerker, 1969). For very large refractive index $|m| = \infty$ (metallic object), there are no refracted rays, and specularly reflected rays

are isotropically distributed. The only contribution to the asymmetry parameter comes from diffracted radiation which gives $g = 0.5$. We designate the asymptotic value of g for large size parameter x, intermediate values of refractive index, and for non-absorbing spheres to be g_∞ and the value of g_∞ is expected to be in the $(1, 0.5)$ range. van de Hulst (1980) noticed that the asymptotic behavior is inversely proportional to the size parameter, the fact he attributed to grazingly reflected waves. This can be written as

$$g^{0i}(x, n) = g^{0i}_\infty(n) - \frac{\Lambda(n)}{x}, \qquad x \to \infty \tag{5.2.1}$$

where 0i indicates no absorption, n is real part of refractive index, slope Λ weakly depends on real part of refractive index. Figure 5.7 shows the asymmetry parameter g obtained from the Mie solution for non-absorbing sphere as a function of size parameter for large x. The same data are presented as a function of $1/x$ where, in addition, a linear fit is superposed for each of the three refractive index values. Figure 5.8 presents the slope Λ and g^{0i}_∞ in (5.2.1). These results were obtained by the the weighted least square fit (Morris, 1990) of (5.2.1) to Mie results for x in the $50 - 200$ range as a function of n. The value of Λ oscillates with respect to n and

$$\Lambda = -1.85 + 0.17n \tag{5.2.2}$$

gives a linear fit. Value of g^{0i}_∞ can also be approximated by

$$g^{0i}_\infty = 1.487 - 0.59n + 0.1n^2 \tag{5.2.3}$$

Both (5.2.2) and (5.2.3) are valid for $n = 1.2 - 2.5$. Shah (1990) derives g^{0i}_∞ from geometric optics and Mie calculations for broader range of parameters.

For absorbing spheres, the effect of the absorption is to reduce the intensity of radiation which passes through the sphere. This causes an increase of asymmetry parameter because the effects of the diffraction peak and the grazing reflection are more prominent (van de Hulst, 1980). For the very large, absorbing spheres Kerker (1969) notes that: According to Fresnel equations, the angular distribution of the reflected and refracted rays is determined almost entirely by the real part of refractive index. Since the particle

Mie
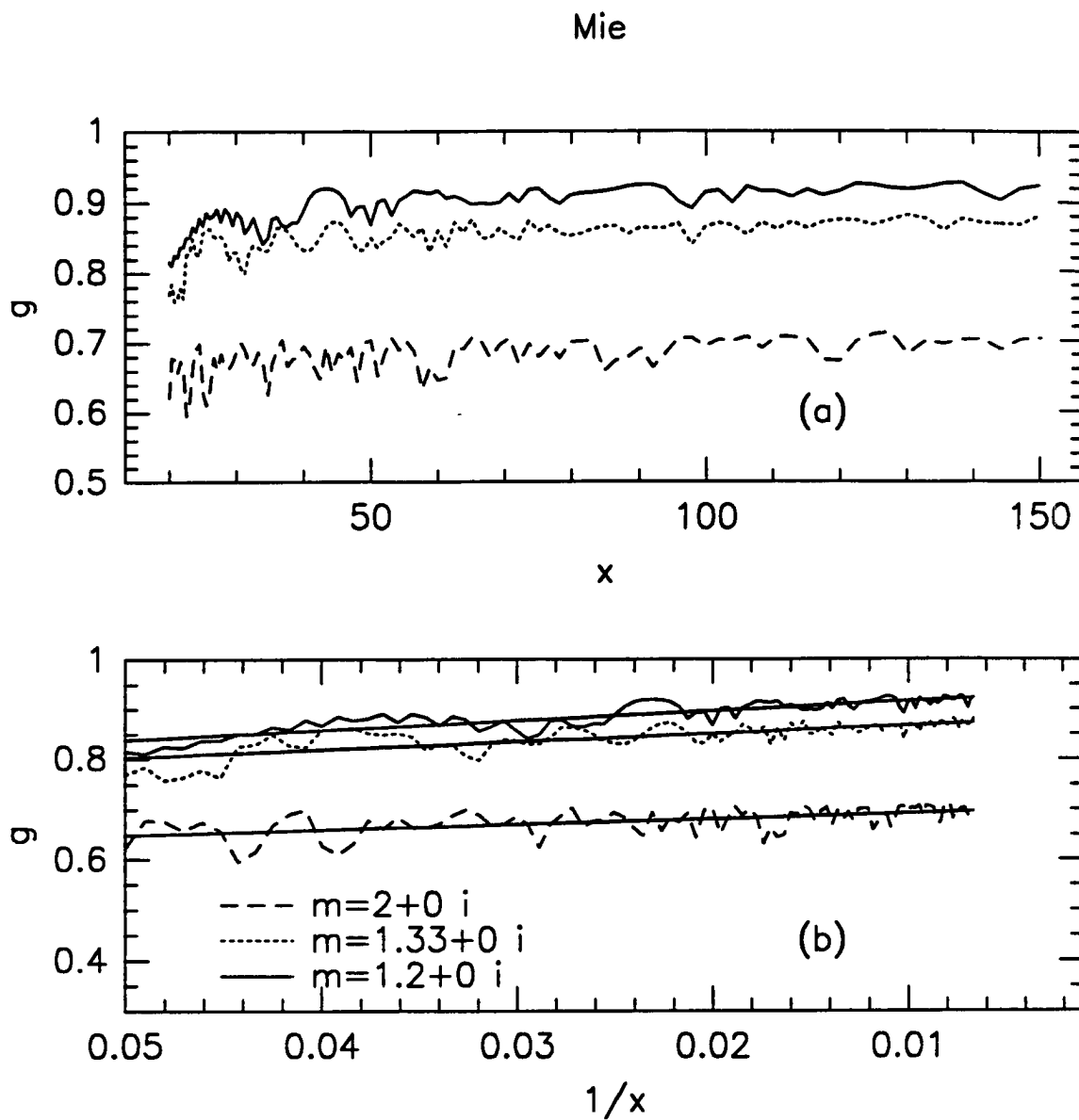
Figure 5.7: (a) Asymmetry parameter g obtained from the Mie solution for non-absorbing sphere as a function of size parameter for large x (b) Same as before but as a function of $1/x$.
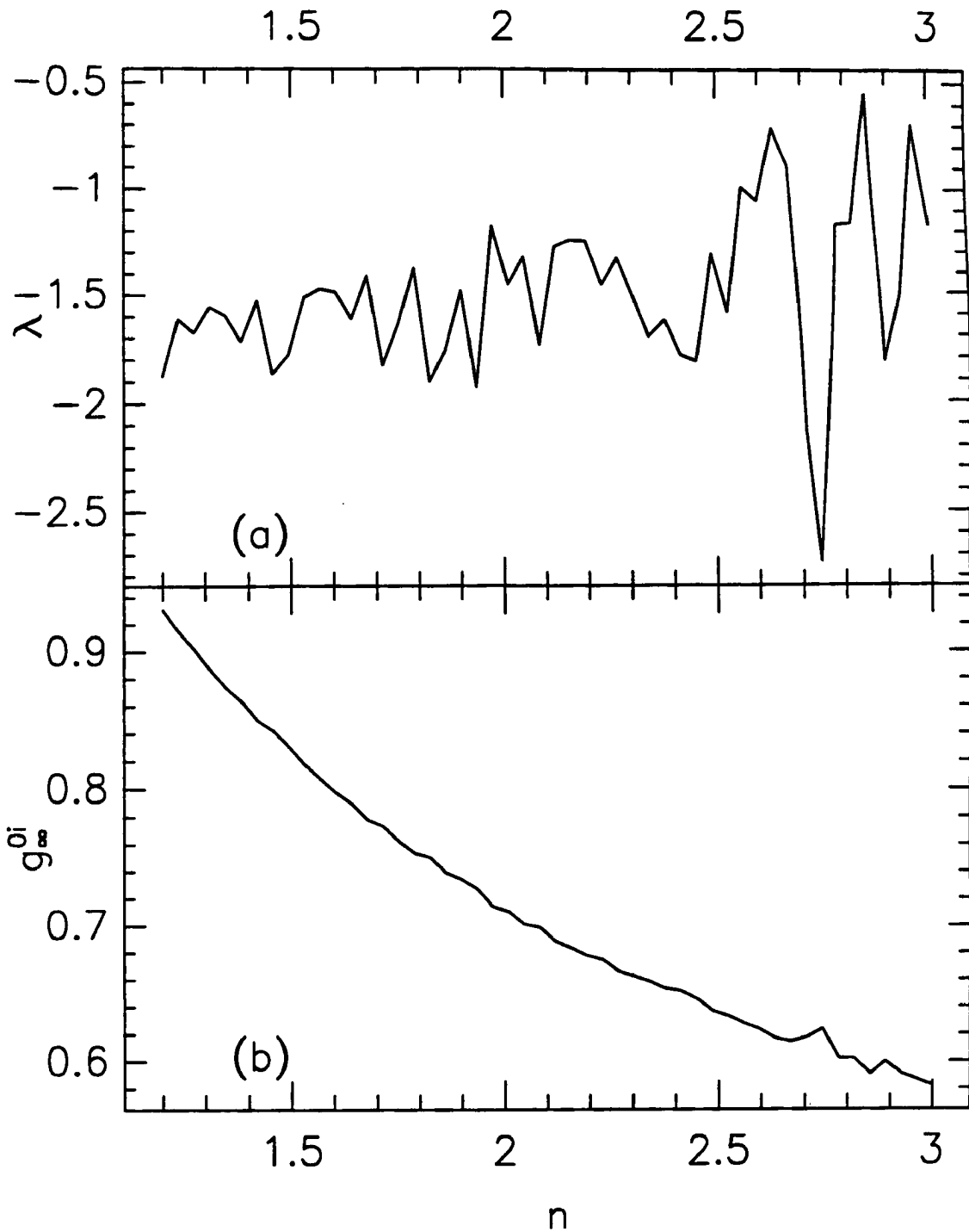
Figure 5.8: (a) Slope Λ in equation 5.2.1 for no absorption case. as a function of real part of refractive index (b) asymptotic value of asymmetry parameter g_∞^{0i} as a function of real part of refractive index.

is so large that all of the refracted energy is lost by absorption and since the diffraction is independent of the optical constants it follows that the asymmetry factor will depend primarily upon the real part of refractive index. This effect is shown in Fig. 5.9a. where the asymmetry parameter g is plotted for three values of size parameter $x = 50, 100, 250$ as a function of the complex part of the refractive index. For large absorption the asymmetry parameter is independent of size but depends on the real part of refractive index; it is $n = 1.33$ in our case. The plot is slightly misleading (Hansen and Travis, 1974) in that for a very large n' the asymmetry factor tends to 0.5 independently of the real part of refractive index. On the basis of analogous analysis Zege and Kokhanovskiy (1988) derived a semi-empirical expression for the asymmetry parameter which is interpolation between to asymptotic regimes for non-absorbing and absorbing

$$g(x, n + n'i) = g^i_\infty(n) - [g^i_\infty(n) - g^{0i}(n, x)]e^{-\beta(n)xn'} \qquad (5.2.4)$$

where $g^{0i}(n, x)$ is given by (5.2.1), β depends on real part of refractive index, $g^i_\infty(n)$ is an asymptotic value for large x with non vanishing absorption. Figure 5.9b is the same as Fig. 5.9a but plotted as a function of $v = xn'$ in (5.2.4). For large absorption the asymmetry parameter is self-similar in such an independent variable. Equation (5.2.4) is similar to functions governing ADT (Chapter 7) and can be integrated to get a closed-form solution for a gamma size distribution. Thus, it provides a convenient parameterization scheme of the asymmetry parameter.

5.2.2 Cubes, hexagonal plates and prisms

We consider here cubes, hexagonal plates with the length $a = 16$ and diameter $b = 64$ (Figure 5.10), and with $a = 24$ and $b = 45$ (Figure 5.11), hexagonal column with $a = 48$ and $b = 24$ (Figure 5.12) for the incident light parallel to the prism (cube and hexagon) axis (x-direction). We also consider a full (not presented) and hollow hexagonal prism for the light propagating along x-axis as in Fig. 5.13) and $a = 25$, $b = 49$. All units are non-dimensional. Figure 5.14 presents an optically soft particle. Solid lines are Mie calculations for equivalent volume spheres for refractive index $m = 1.01 + 0.001i$ (such a particle would look black), squares are DDA calculations for cubes. For this refractive index, the reflected

Mie
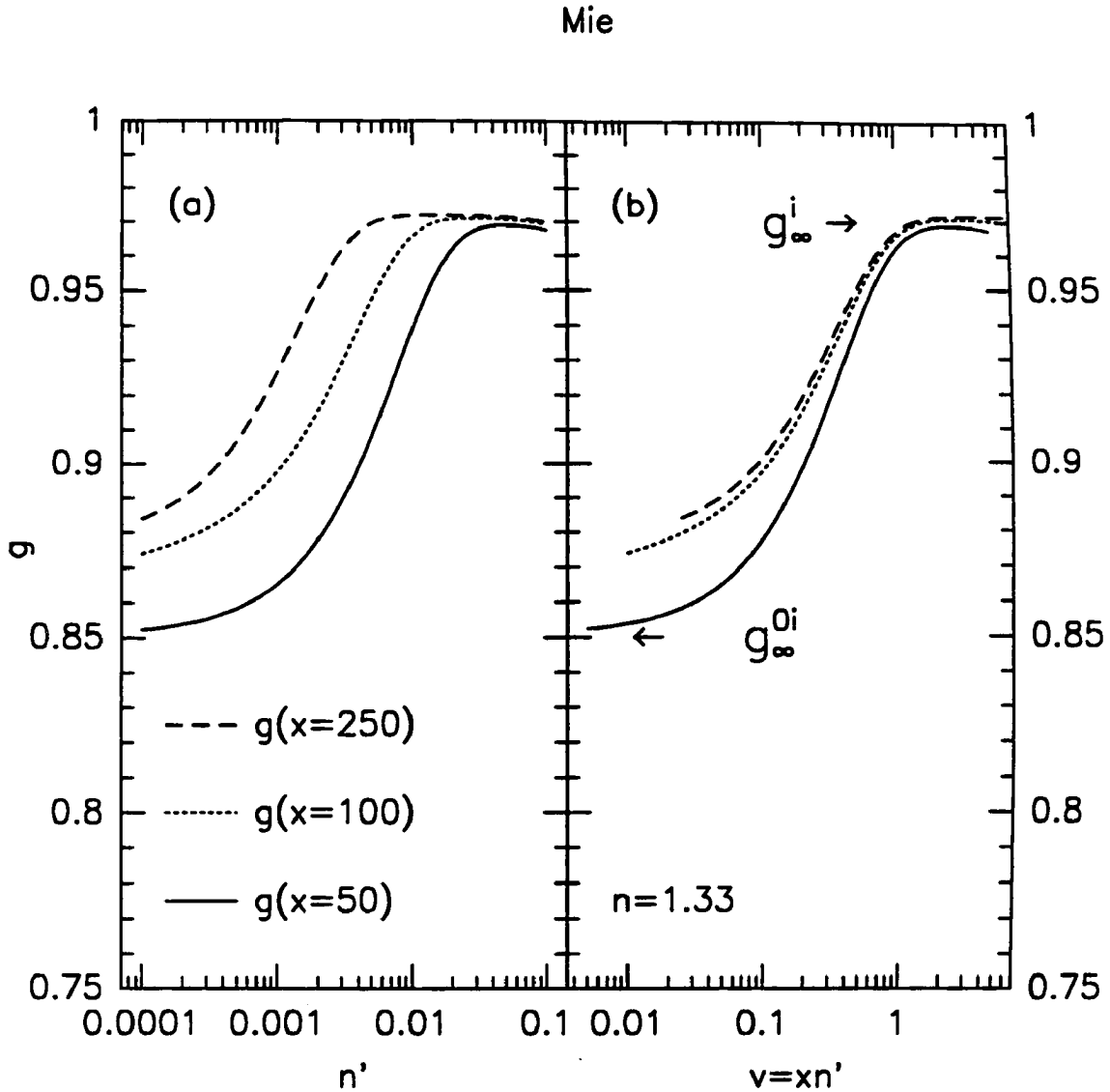
Figure 5.9: (a) Asymmetry parameter g for three values of size parameter x as a function of complex part of refractive index. Real part of refractive index is $n = 1.33$. For large absorption the asymmetry parameter is independent of size. (b) Same as in (a) but plotted as a function of $v = xn'$. Self-similar behavior for $v \approx 1$ can be seen.

Pseudo-hexagon

$(\theta=0 \quad \varphi=0 \quad \beta=0)$
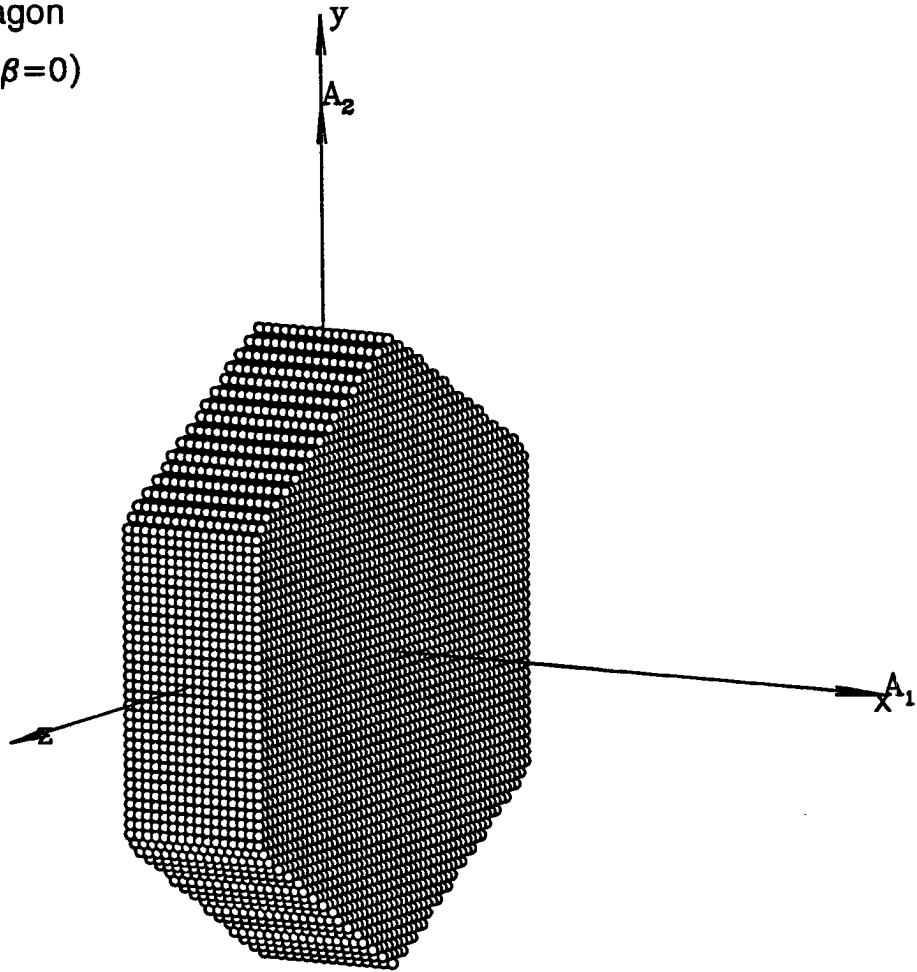
Figure 5.10: Hexagonal plate of length $a = 16$, and "diameter" (distance between opposite vertices) $b = 64$ (non-dimensional units). There are $N = 42304$ dipoles in this target.

and refracted components of the asymmetry parameter are similar to that of the sphere. Absorption is proportional to volume for this complex part of the refractive index. Thus, in such "equivalent volume" type comparison both cubes and spheres have apparently similar absorption efficiencies and the diffracted component. The asymmetry parameter for such soft particles seems to be shape independent. Another limiting case is presented in Fig. 5.15 which corresponds to the metallic case (iron has refractive index $m = 1.27 + 1.37i$ at $\lambda = 0.42 \ \mu$m). For such large absorption, the refraction component is negligible. The diffraction component are similar for large size parameters and reflection determines the asymmetry parameter. The length of the object is not important. Thus, the plate with large aspect ratio 16 × 64 has the lowest asymmetry parameter. Figures 5.16 and 5.17

Pseudo-hexagon

$(\theta=0 \quad \varphi=0 \quad \beta=0)$
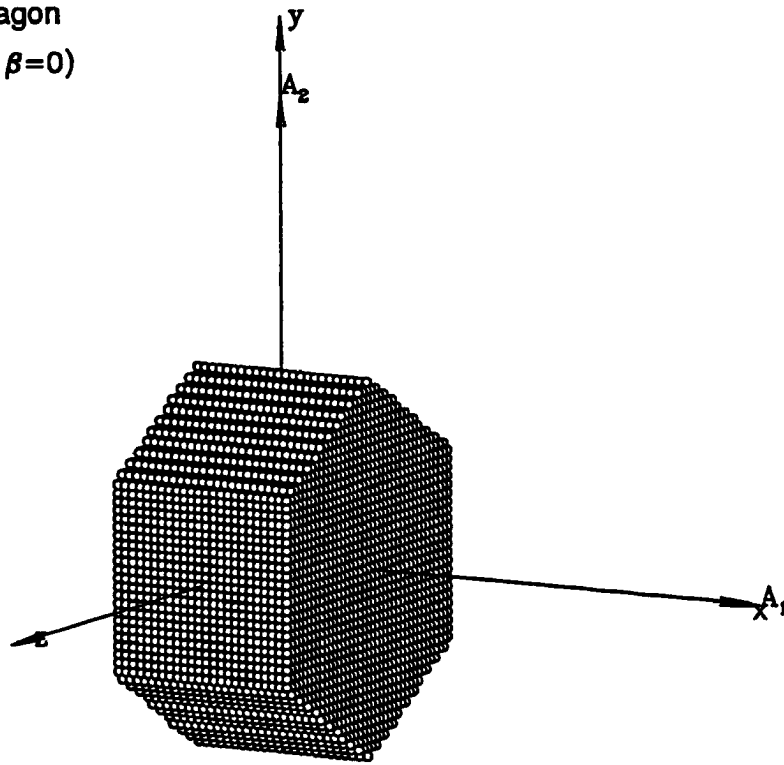
Figure 5.11: Same as 5.10 but for $a = 24$, $b = 45$, and $N = 31560$.

Pseudo-hexagon

$(\theta=0 \quad \varphi=0 \quad \beta=0)$
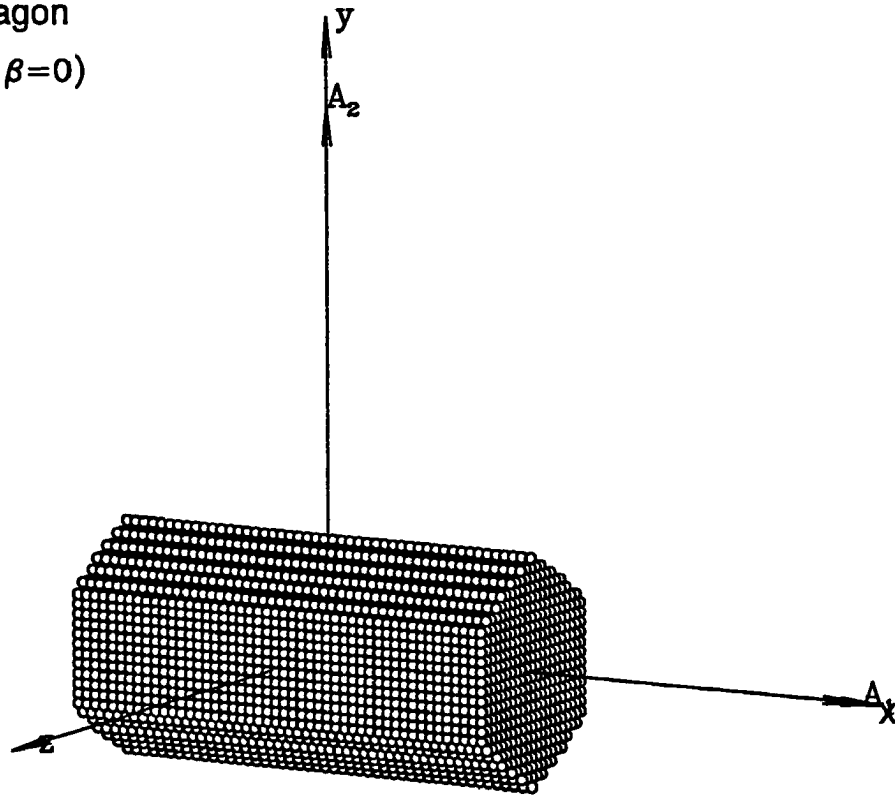
Figure 5.12: Same as 5.10 but for $a = 48$, $b = 24$, and $N = 18048$.

Hollow hexagon

$(\theta=0 \quad \varphi=0 \quad \beta=0)$

r=24 z/2=12 r=24/3
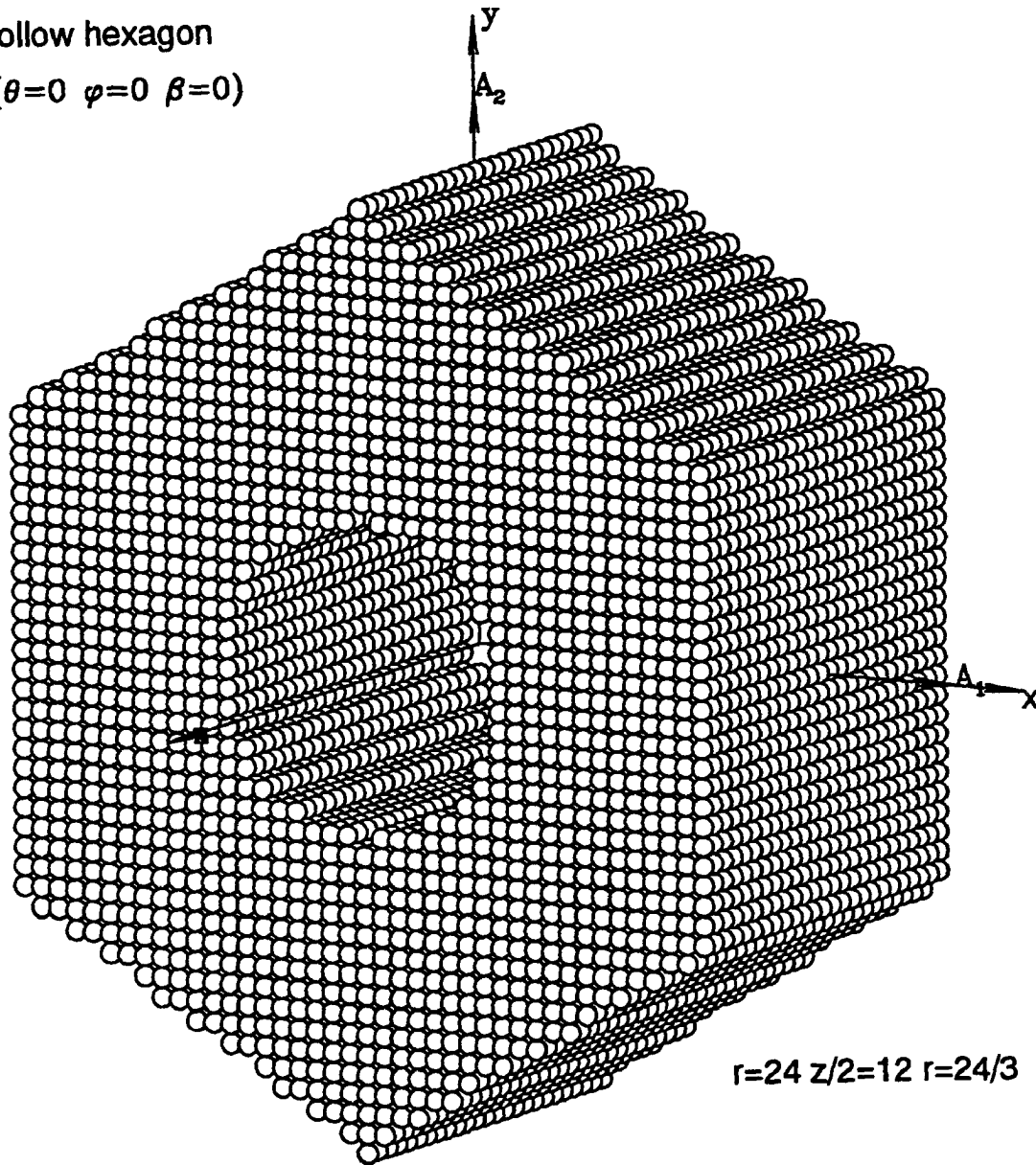
Figure 5.13: Same as 5.10 but for hollow prism with $a = 25$, $b = 49$, and $N = 32350$.

(unpolarized)
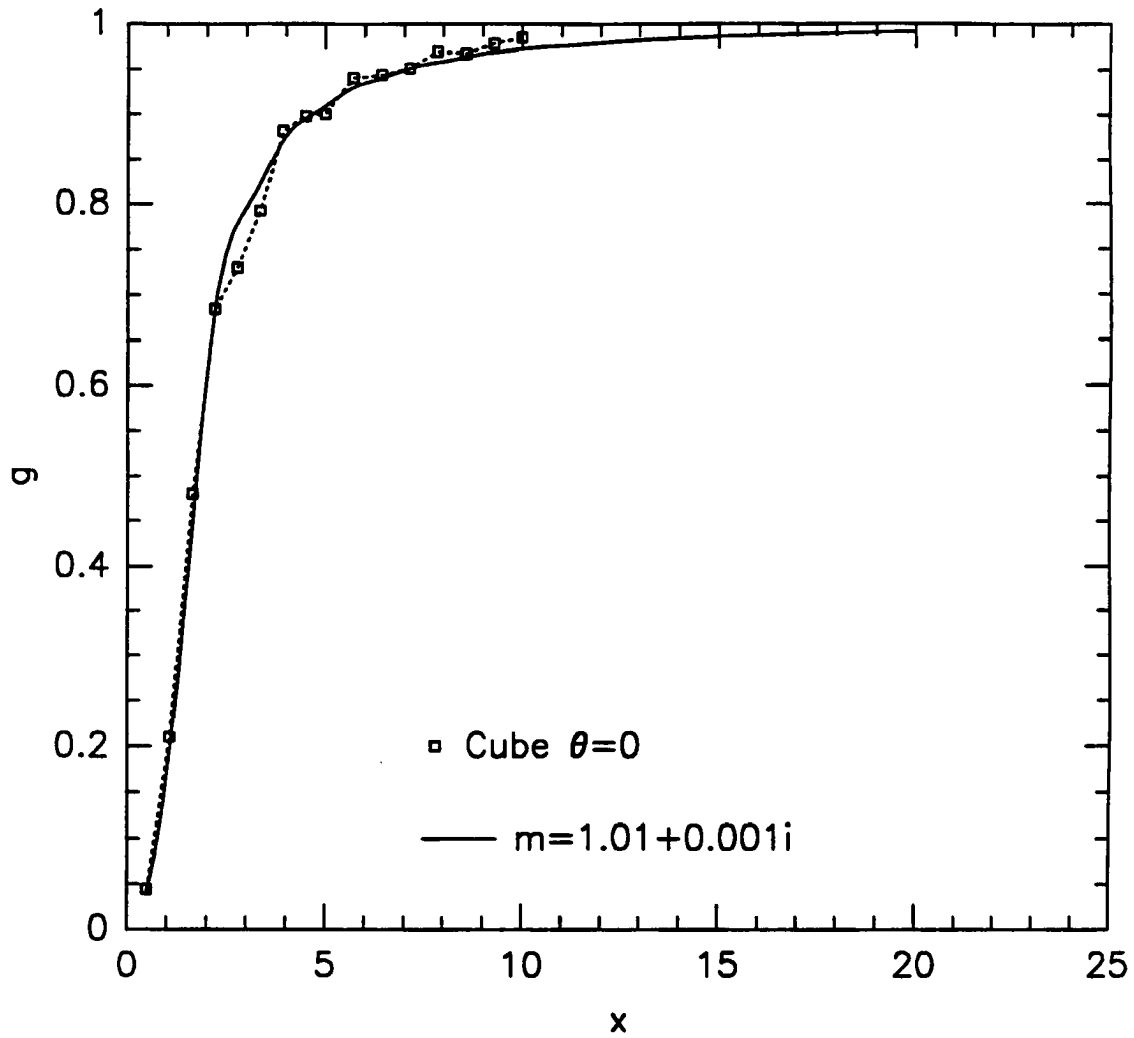
Figure 5.14: Asymmetry parameter for cube (squares) and sphere (solid line) for soft particles of refractive index $m = 1.01 + 0.0001i$.

axis incidence (unpolarized)
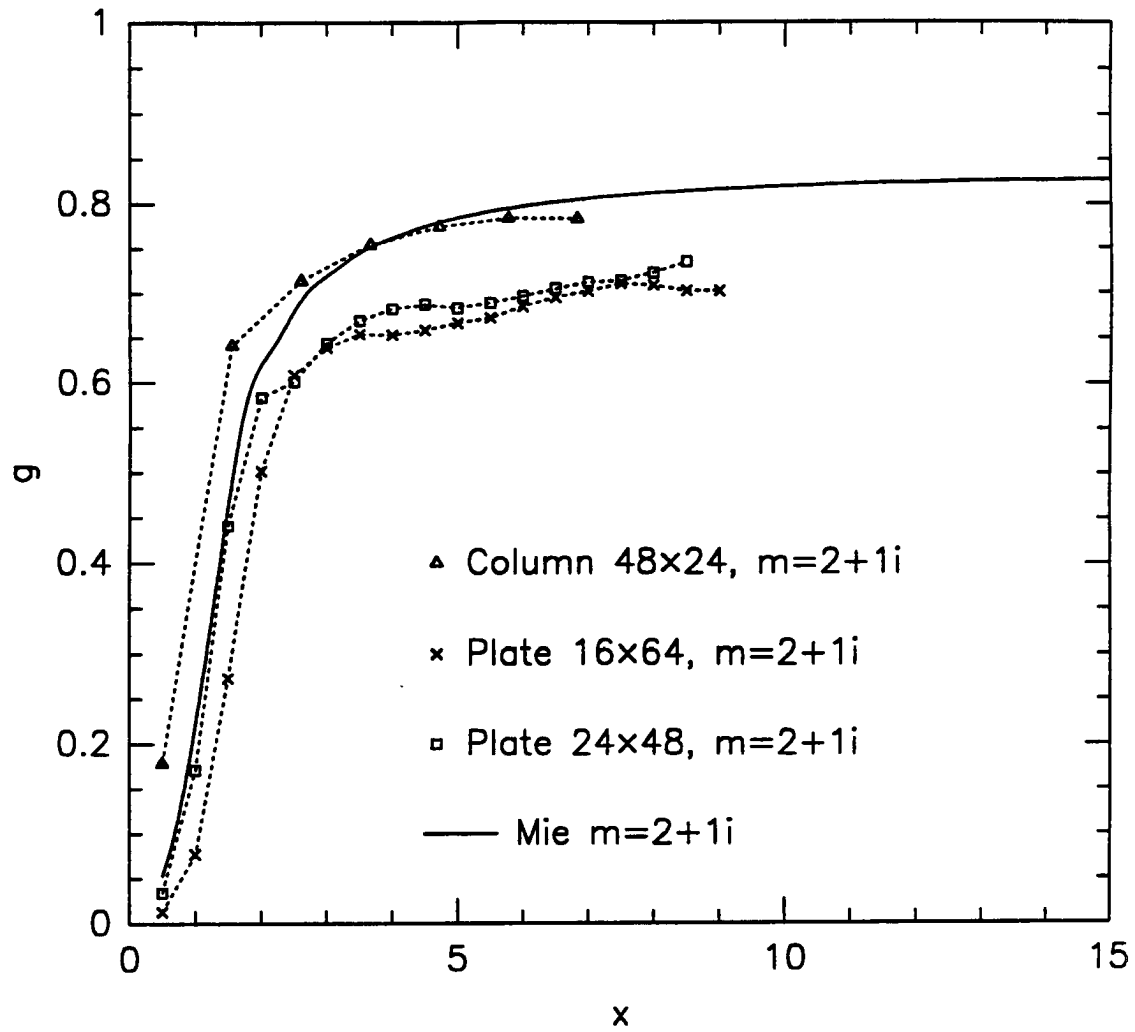
Figure 5.15: Asymmetry parameter for 46 × 24 column (triangles), 16 × 64 plate (crosses), 24 × 48 plate, and sphere (solid line) for semi-metallic refractive index $m = 2 + 1i$.
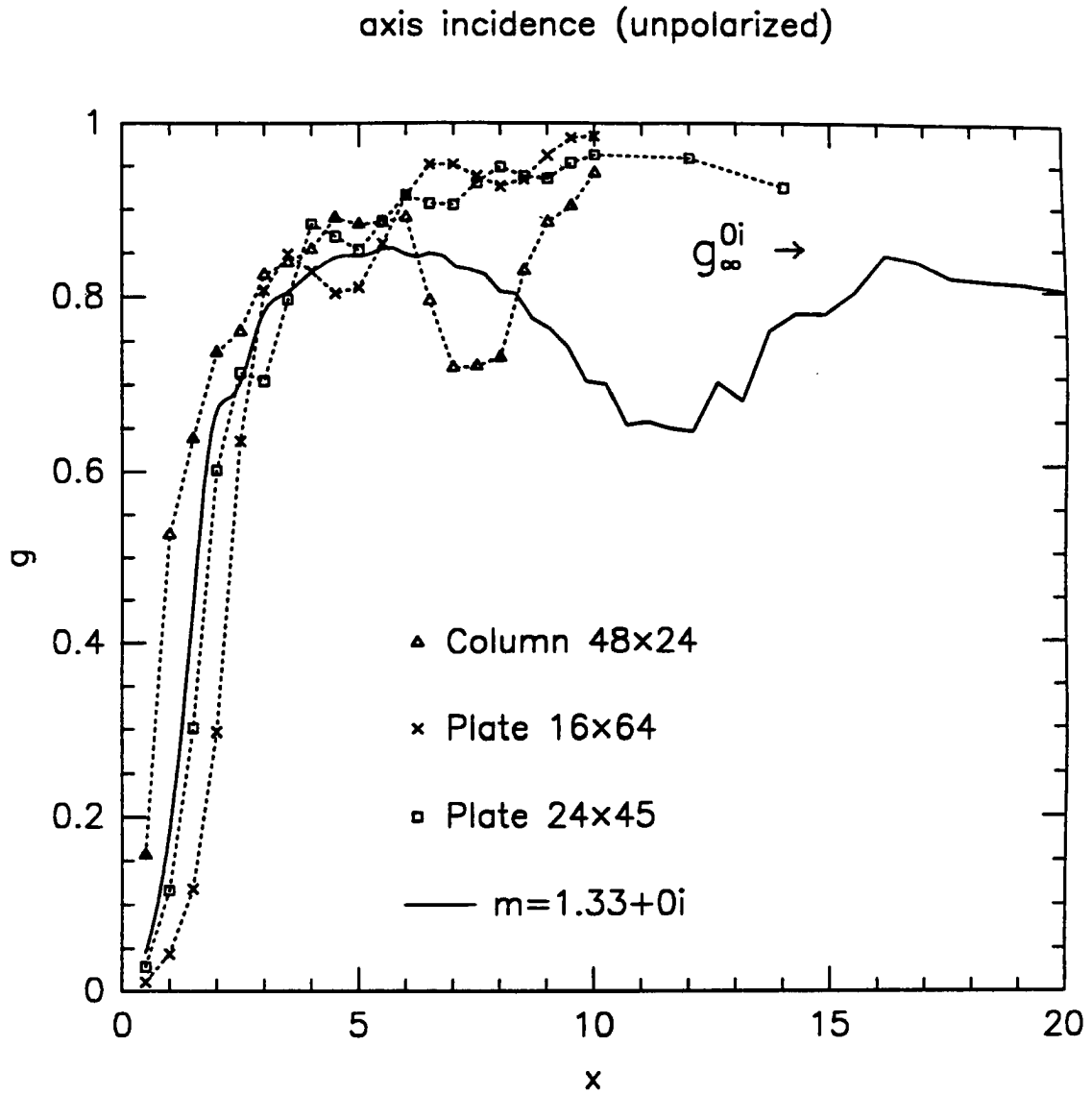
Figure 5.16: Same as in 5.15 but for non-absorption case with the refractive index $m = 1.33 + 0i$.
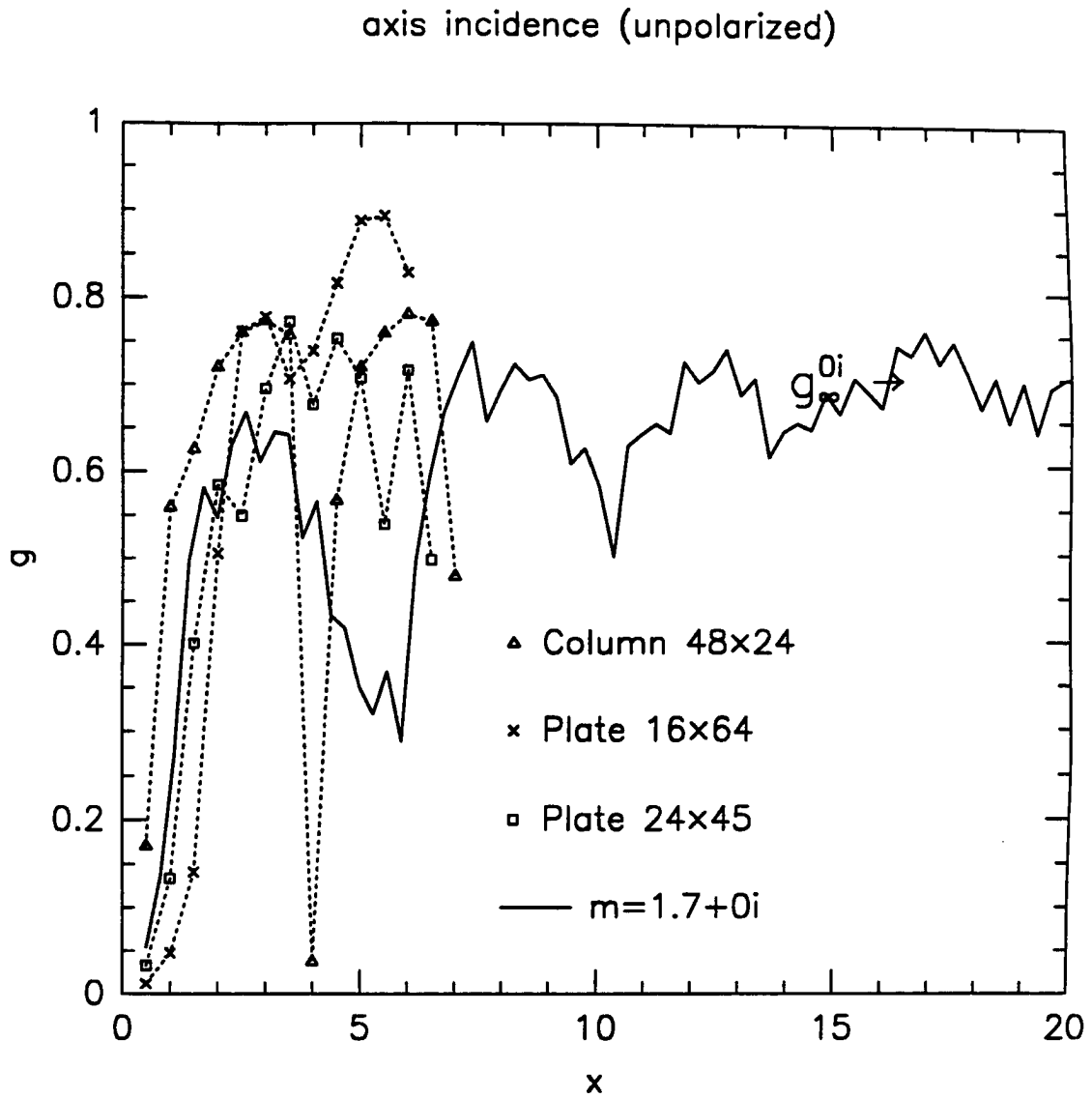
Figure 5.17: Same as in 5.15 but for non-absorption case with the refractive index $m = 1.7 + 0i$.

show the asymmetry parameter for the case without absorption. The asymptotic value of asymmetry parameter for large size parameter is needed to estimate g_{∞}^{0i} (c.f. 5.2.1). Solid line in Fig. 5.16 and 5.17 is for Mie calculations and g_{∞}^{0i} in this plot if for spheres. It is not possible to give a definite value of g_{∞}^{0i} for irregular particles by examination of Figs 5.16 and 5.17. However, the asymmetry parameter derived for the irregular particles is generally larger in comparison to equivalent spheres. This indicates that the backscatter plays an insignificant role which is contrary to Pollack and Cuzzi's (1980) assumption. The results are also in agreement with Asano and Sato's (1980) calculations for randomly-oriented spheroids and for similar range of size parameters.

However, calculations of random averages would present more definitive answer. For the absorption case there is little difference between 24 × 45 plates with the complex refractive index 0, 0.01, and 0.001 (Figure 5.18). This is qualitatively similar to the spherical case (solid lines in Figure 5.18). Two orientations of incident light are presented in Figure 5.19.

The asymmetry parameter for small size parameters is similar to that of equivalent volume spheres. The larger the size parameter, the larger is g in comparison with an equivalent volume sphere. This is similar to the case of hexagonals plates and columns in this refractive index range. Figure 5.20 corresponds to the geometry presented in Fig. 5.13. This is for full and hollow prisms. The hollow plate has a slightly larger asymmetry parameter then for a solid particle. We attempted to obtain the larger size parameter values. However, it required a large computational effort; approximately one hour of CRAY Y-MP CPU time for each data point, due to the slow convergence of conjugate gradient iterations. This fact illustrates well that further theoretical research is needed to improve the DDA methods, in particular with regard to the problem of orientational averages for large values of size parameter.

5.3 Porosity and particle structure

In recent years there has been a growing interest in the study of scattering properties of particles with highly irregular shapes such as branched chains of aerosols (Iskander
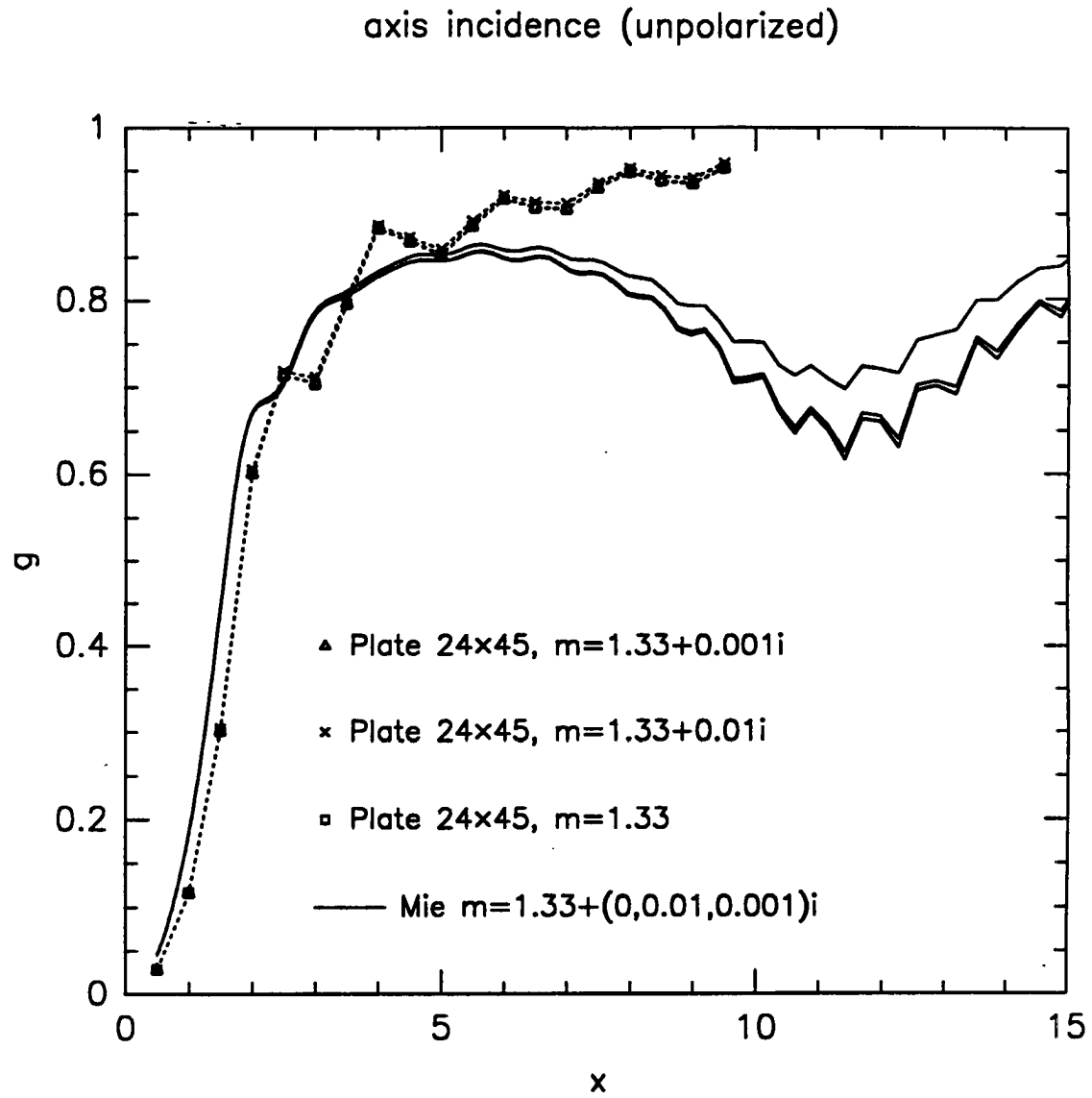
Figure 5.18: Asymmetry parameter for 24 × 45 plate for refractive index $m = 1.33 + 0i$, $m = 1.33 + 0.01i$, and $m = 1.33 + 0.001i$. Solid lines are for the same values of refractive index but for spheres.
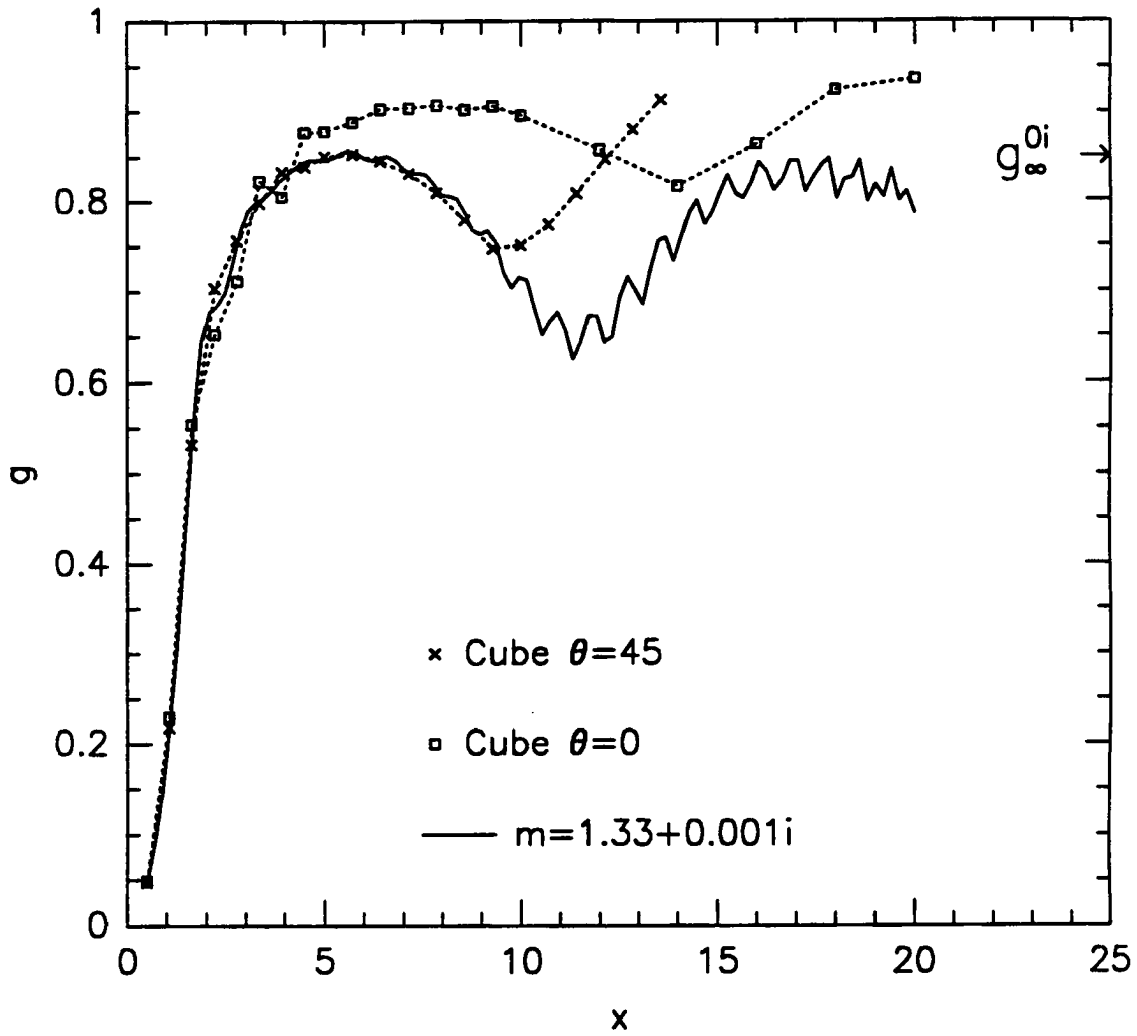
Figure 5.19: Asymmetry parameter for a cube with refractive index $m = 1.33 + 0.001i$ as a function of size parameter for two orientations (face,$\theta = 0$ and edge, $\theta = 45$.

side incidence (unpolarized)
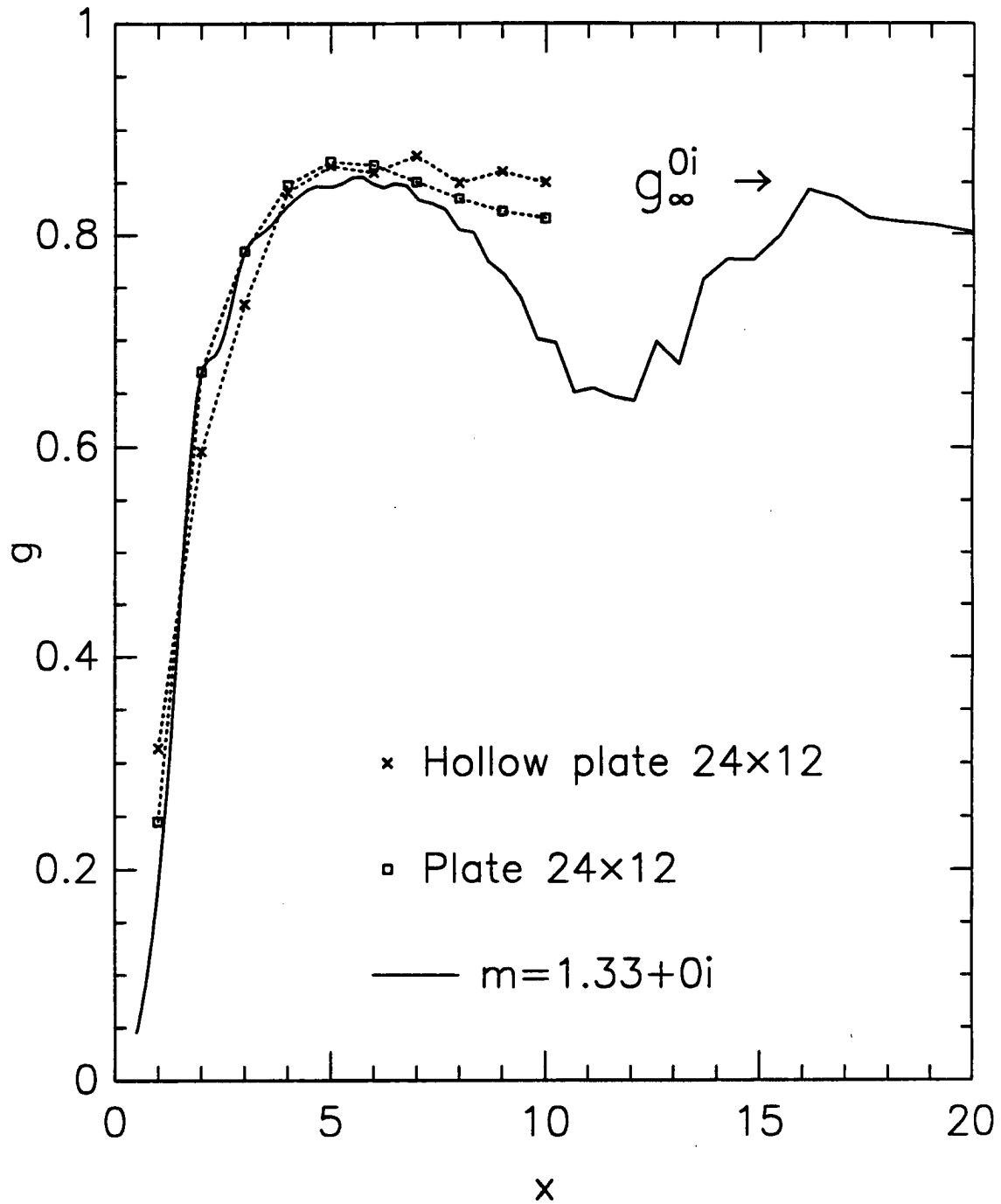
Figure 5.20: Asymmetry parameter for full and hollow plate with refractive index $m = 1.33 + 0i$ as a function of size parameter.

et al., 1989; Ku and Shim, 1992), helical structures (Chiappetta and Torresani, 1988), fractal dust grains (Wright, 1987), "fluffy" particles (Hage and Greenberg, 1990), aggregate particles (West and Smith, 1991), and chiral particles (Keller et al., 1985). Aerosol studies are relevant to detection of airborne particles, characterization of atmospherics aerosols and predicting their climatic effects, and evaluation of the various scenarios of nuclear winter, evaluation of radiant heat transfer from flames (see Iskander et. al (1989) and references therein). A related problem, but considerably less studied, is that of scattering by highly nonspherical particles like hollow prisms, combination of bullets (rosettes), twist and twin prisms, spatial plates, or rimed crystals. Such problems have to be ultimately treated in a certain averaged sense at least for the purpose of highly parameterized numerical models. In this section we discuss the "colored sphere" problem for randomly averaged orientations. We impose inhomogeneity in refractive index which are to represent structure within the crystal. It is is believed that random averaging of scattering properties over all orientations leads to more uniform scattering properties. Such problems are tightly connected to stochastic radiative transfer because particle structure has to be defined in certain mean and deviation from the mean sense.

To build some intuition about the effects of internal structure on far field scattering, we begin with the two sphere cluster. Figure 5.21 presents extinction (Q_{ext}) and absorption (Q_{abs}) efficiencies for two spheres in multipole approximation for truncation $N_t = 10$. Squares are for the case of refractive index $m = 1.7 + 0.01i$ (both spheres) and light propagating parallel to the common axis. Crosses are for the same uniform distribution of refractive index but for random average over all orientations. The solid line shows results of Mie calculations. Clearly extinction efficiencies for the particular orientation case deviates strongly from the random orientation case. Randomly averaged extinction is closer to Mie results but still significantly differs from it. Thus, there is certain degree of uniformization but the shape signature is significant even after full random orientation averaging. Consider now Figures 5.22 and 5.23. These are exact solutions for two spheres but for the non-uniform distribution of the refractive index. In Fig. 5.22 crosses are for $m = 1.72 + 0.01i$ and $m = 1.68 + 0.01i$, and squares are for large fluctuations in the real
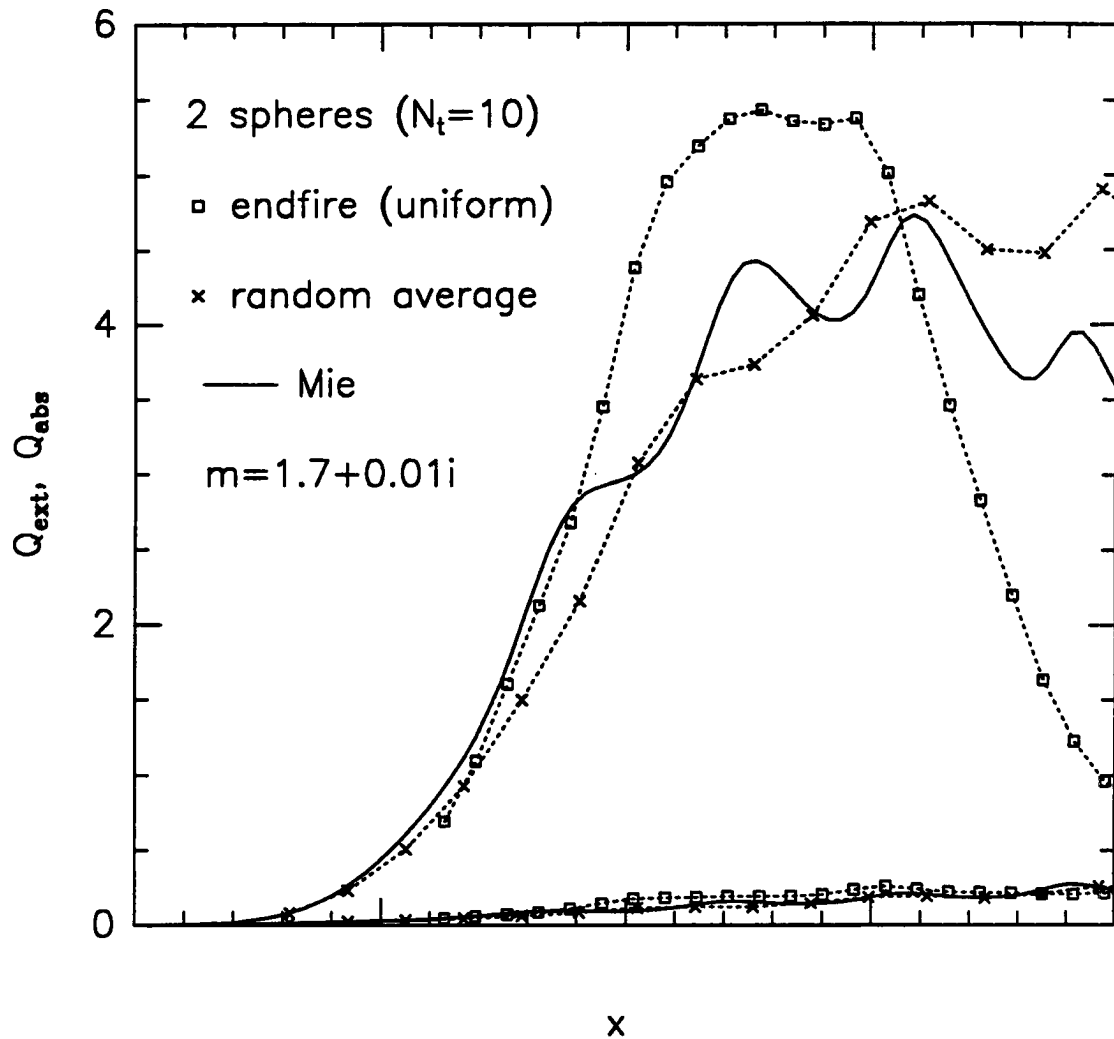
Figure 5.21: Extinction (Q_{ext}) and absorption Q_{abs} efficiencies for two spheres in multipole approximation for truncation $N_t = 10$. Squares are for the case of refractive index $m = 1.7 + 0.01i$ (both spheres) and light propagating parallel to the common axis. Crosses are for the same uniform distribution of refractive index but for random average. Solid line shows results of Mie calculations.

DMSCAT

Two spheres ($N_t=10$)

Random average.

$\square$ m=1.7+0.01i (uniform)

$\times$ (1.72,1.68)+0.01i

$\triangle$ (1.80,1.60)+0.01i
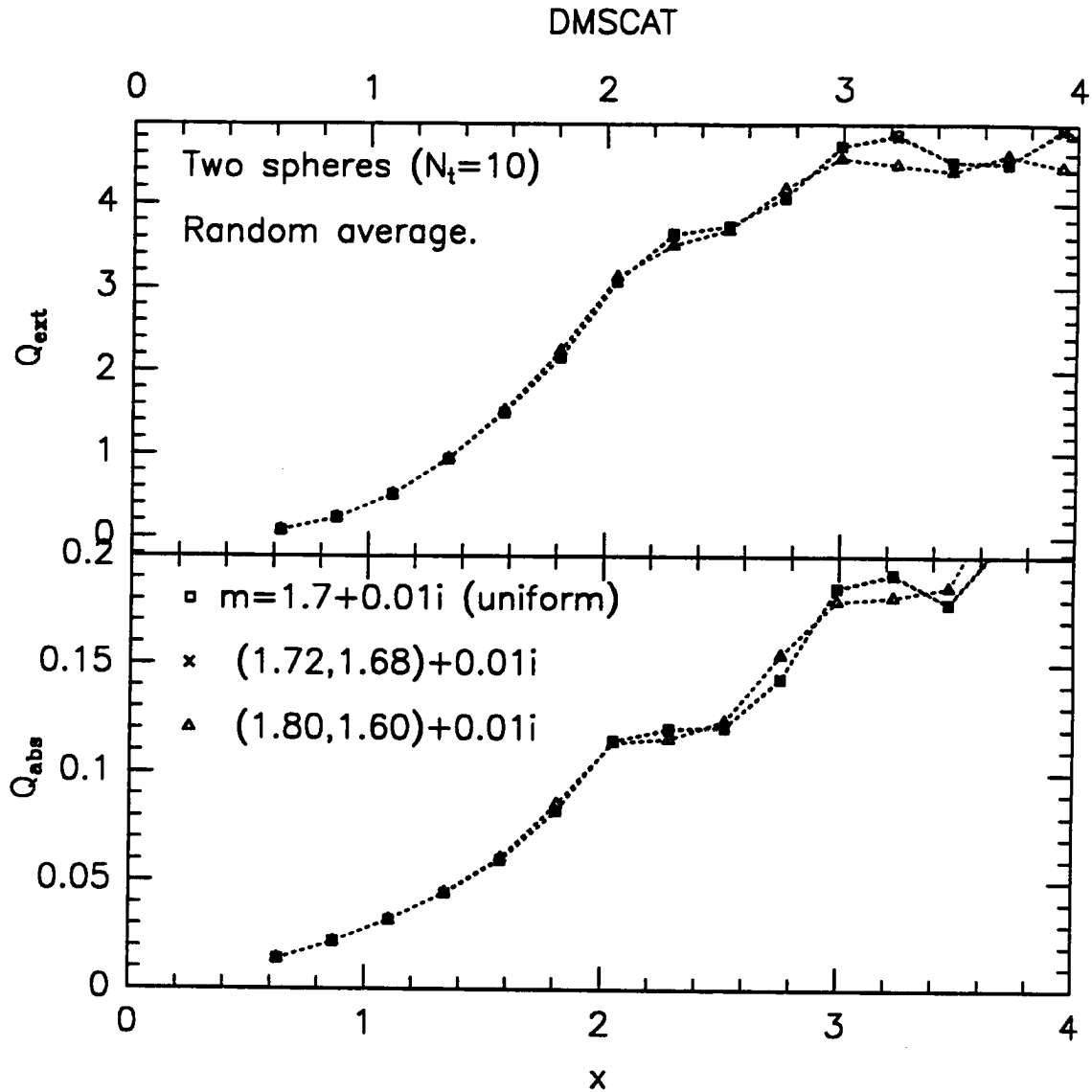
Figure 5.22: Same as in 5.21 but for non-uniform distribution of the refractive index. Crosses are for $m = 1.72 + 0.01i$ and $m = 1.68 + 0.01i$, and squares for large fluctuations in the real part of refractive index $m = 1.80 + 0.01i$ and $m = 1.60 + 0.01i$.
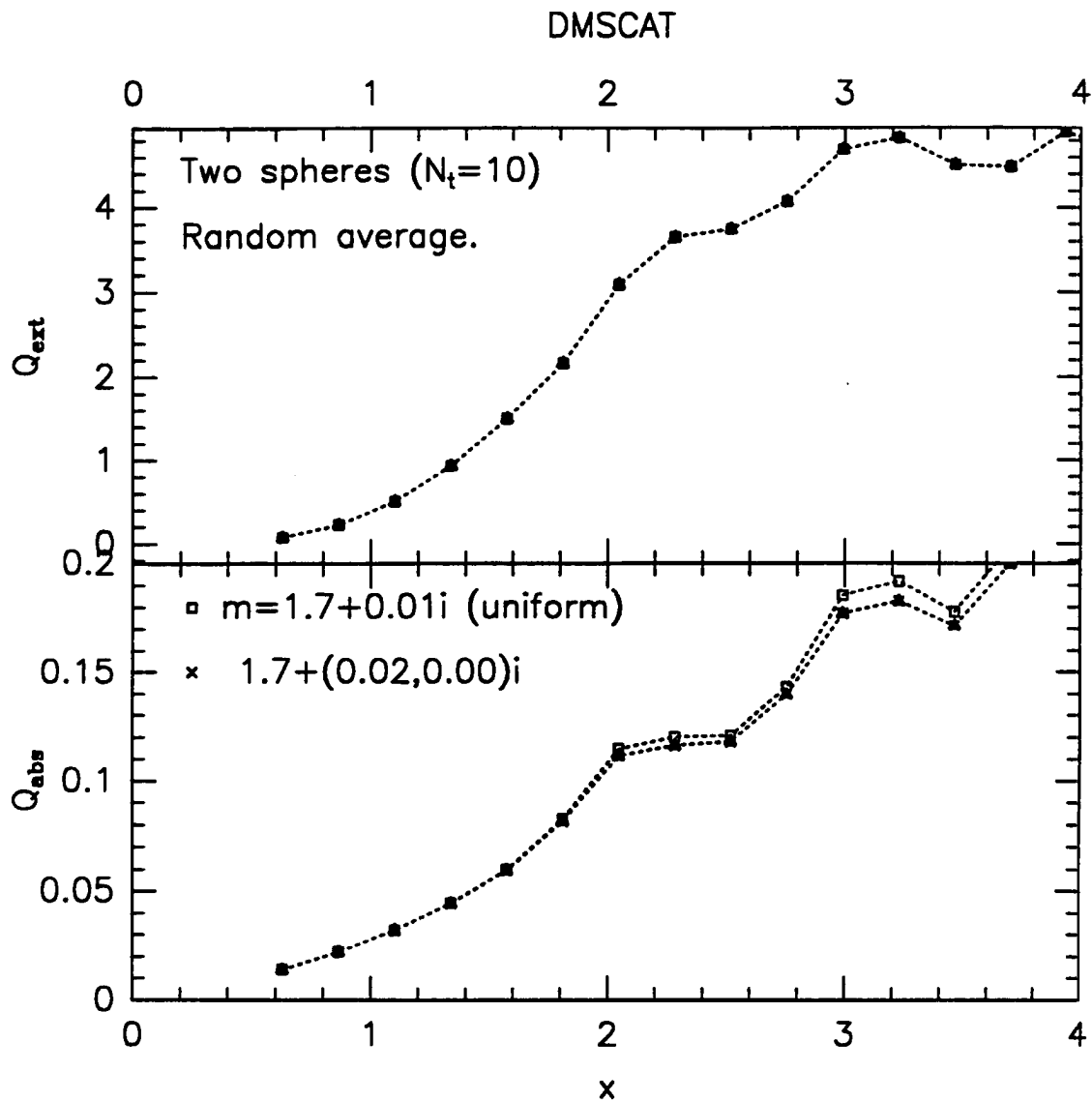
Figure 5.23: Same as in 5.22 but for non-uniform distribution of complex part of refractive index. Crosses are for $m = 1.7+0.01i$ and $m = 1.7+0.01i$, and squares for $m = 1.7+0.02i$ and $m = 1.60 + 0i$.

part of refractive index $m = 1.80 + 0.01i$ and $m = 1.60 + 0.01i$. In Fig. 5.23 crosses are for $m = 1.7 + 0.01i$ and $m = 1.7 + 0.01i$, and squares are for $m = 1.7 + 0.02i$ and $m = 1.60 + 0i$. Notice that an average refractive index is kept $1.7 + 0.01i$ for all cases discussed in this section. For small fluctuations of refractive index the results are very close to the case of $m = 1.7 + 0.01i$, i.e. of the uniform distribution of refractive index. However, for larger deviations, and larger size parameter, changes in efficiencies become apparent. Changes in complex refractive index couple strongly to absorption efficiencies (Figure 5.23).

We will now discuss the dipole approximation for a sphere composed of $N = 136$ dipoles placed on a cubic lattice. Figure 5.24 shows such a sphere. Every dipole may be colored, i.e. assigned different values of refractive index. A spherical target is incidental here and any shape could be discussed. In principle, by imposing various refractive index changes, we can model ice crystals with air bubbles (porosity), sooth inclusions, twisted structures, etc. Four such models are presented in Figure 5.25 (a) is for the uniform, $m = 1.7 + 0.01i$, distribution of the refractive index over all lattice elements, (b) is for with four different values of refractive index $m = 1.8 + 0.01i$, $m = 1.6 + 0.01i$, $m = 1.9 + 0.01i$, and $m = 1.5 + 0.01i$ these values are assigned to dipoles in four quarters of a sphere, (c) distribution with two different values of refractive index $m = 1.85 + 0.01i$ $m = 1.45 + 0.01i$ assigned uniformly to two halves of a sphere, (d) fractal distribution with the power spectrum -0.4 (in one dimension). These models (a,b,c, and d) progress from uniform to more random. Results for these refractive index distributions are shown in Figure 5.26. The results for the "fractal" case is not presented but would overlap the uniform case. We have noticed that such fractal distributions, but with small deviation from the mean, result in scattering properties similar to the uniform distribution. For larger deviations from the uniform refractive index, larger size parameters, and well-defined refractive index domains the average over all orientations case shows a signature of particle structure. This is quite similar to the two sphere cluster discussed above.

In passing we mention that the orientation averages discussed here for the multipole approximation are based on the direct inversion of a matrix (Mackowski, 1992) and not on a sequence of solutions to many particular light incidence problems. The technique is

similar to that discussed by Flatau et. al (1990) in the DDA case. However, extensions to larger particles is of importance and suggestions for achieving this are discussed in Chapter 8.

5.4 Summary

Efficiencies for ice particles of small size parameters are fairly insensitive to shape and structure but this is progressively less so for increasing size parameters. There is a tendency of uniformization of colored problems to gray ones, but the structure can still be seen in efficiencies, particularly for pronounced inhomogeneities (large domains and/or large deviations in refractive index). It remains to quantify and systemize these effects with, perhaps, fractal dimension as a parameter in case an of air bubble or sooth inclusions. As a next step, non-spherical and non-homogeneous cases should be attacked. This requires an efficient solution technique for large, full orientation averages, cases, what is apparently, a difficult theoretical task. We present some results for another highly irregular shape (combination of hexagonal bullets) in Chapter 8.
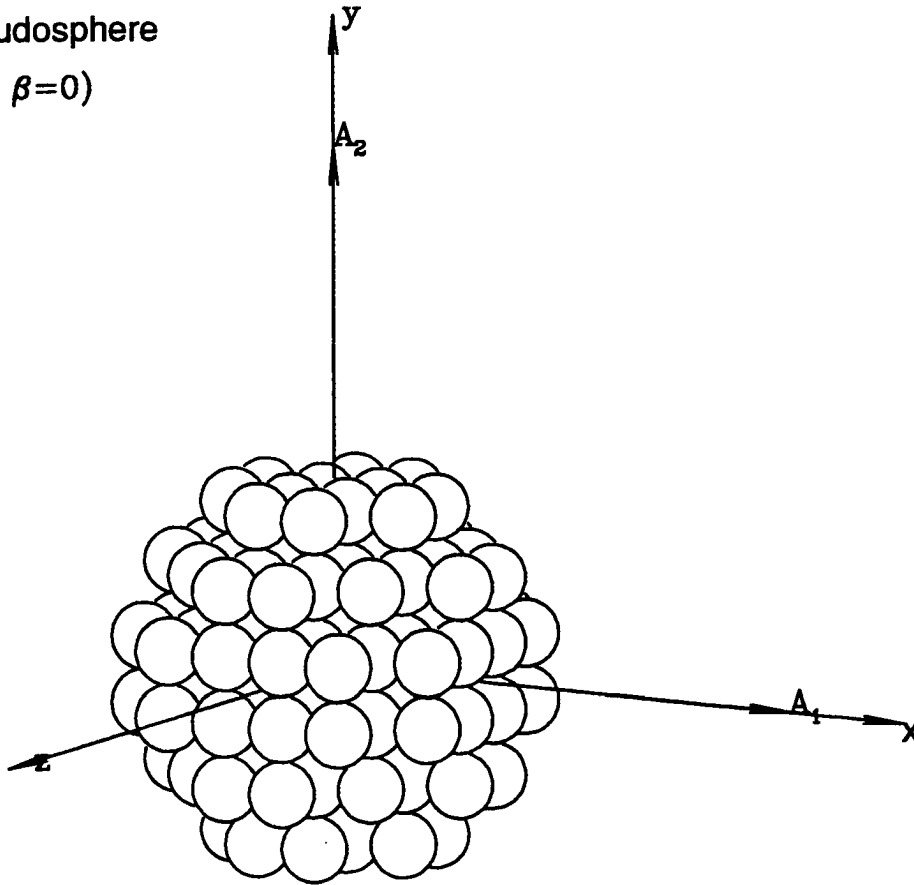
Figure 5.24: Pseudosphere composed of $N = 136$ dipoles. Each dipole may have different refractive index.
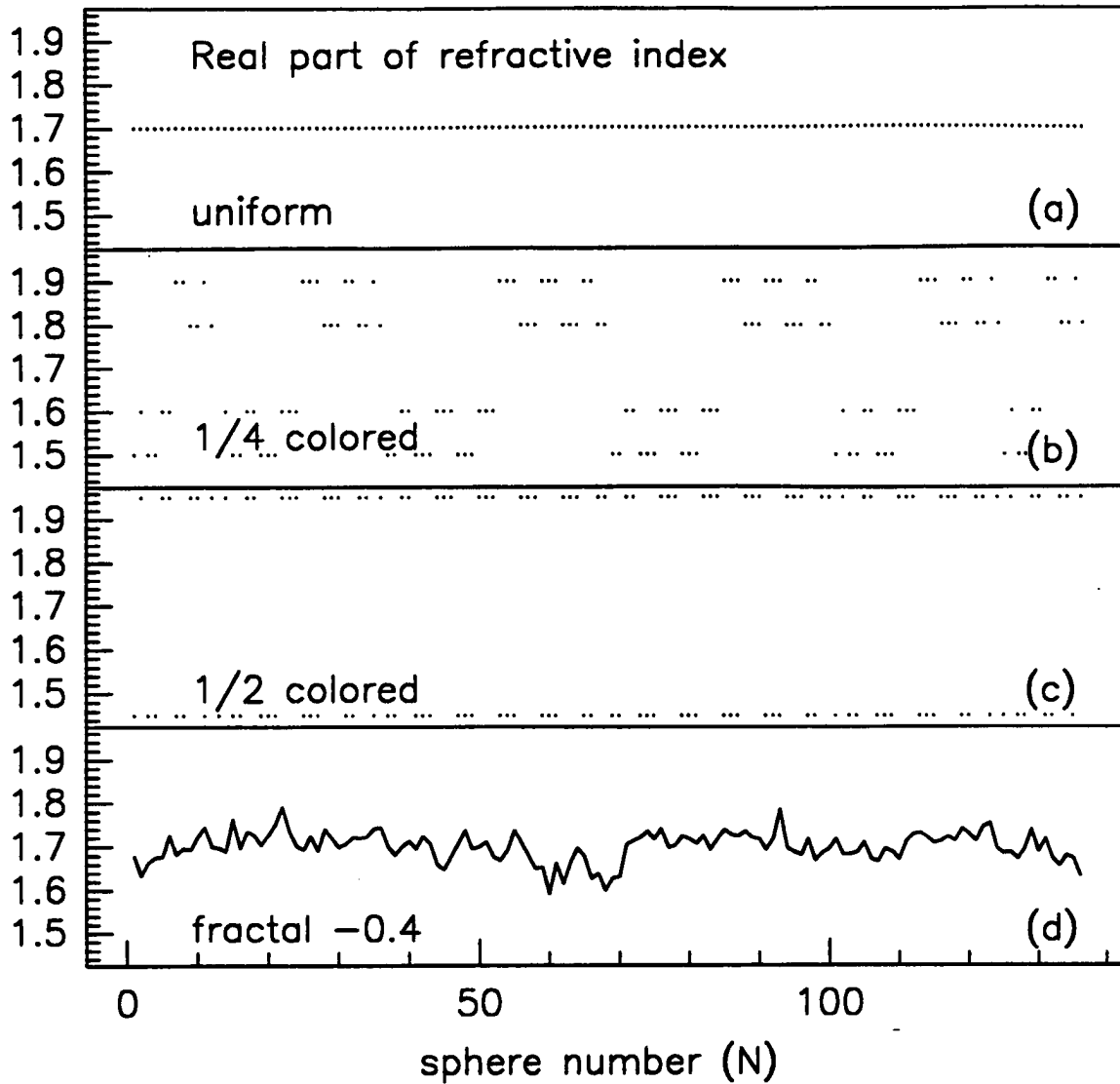
Figure 5.25: Four model of non-uniform distribution of refractive index. (a) uniform, $m = 1.7 + 0.01i$, (b) lattice dipoles with four different values of refractive index $m = 1.8 + 0.01i$, $m = 1.6 + 0.01i$, $m = 1.9 + 0.01i$, and $m = 1.5 + 0.01i$, (c) lattice dipoles with two different values of refractive index $m = 1.85 + 0.01i$ $m = 1.45 + 0.01i$, (d) "fractal" distribution with the power spectrum -0.4.

DMSCAT
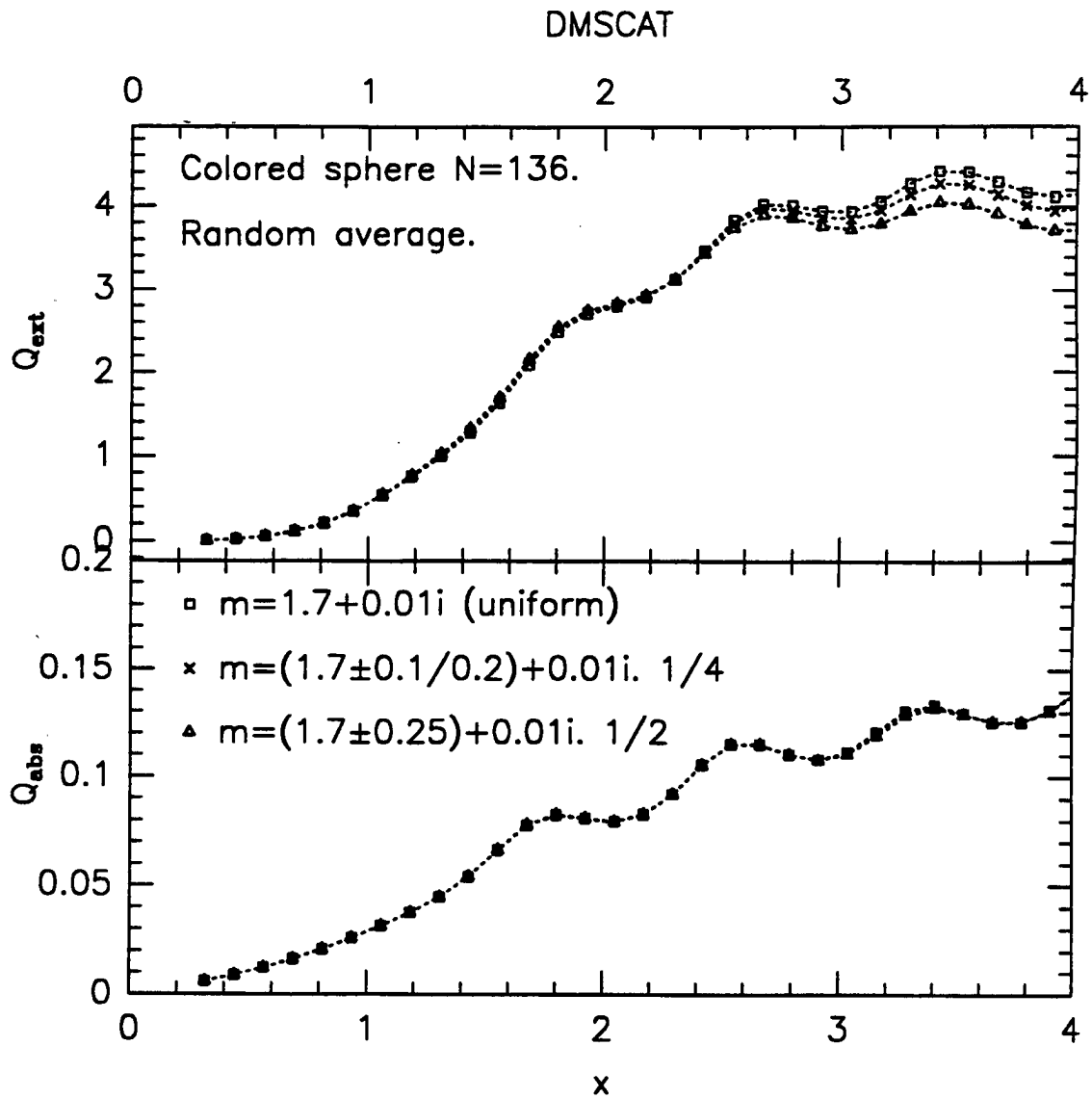
Figure 5.26: Extinction and absorption efficiencies for colored pseudosphere composed of $N = 136$ dipoles placed on cubic lattice. Refractive models are are illustrated in Figure 5.25. Result for fractal distribution are same as for the uniform case (squares).

Chapter 6

COMPARISON OF THE ADT WITH DDA FOR CUBES

6.1 Introduction

In this chapter we discuss comparisons between the rigorous and approximate methods — discrete dipole and anomalous diffraction approximations. The very large body of work related to the anomalous diffraction theory (ADT) for irregular shapes is commonly presented without verification with rigorous methods. This is particularly true for medium and large size parameters which we deal with here. There is a temptation to use ADT because of its simplicity. However, as we show, the ADT and DDA do not agree for certain cases.

On a more technical note we describe in this chapter a fast and general method for the anomalous diffraction theory (ADT) calculations for particles of arbitrary shape. It allows calculations to be preformed on most targets for which the ADT results have been published up to now. In addition extinction and absorption efficiencies for any convex polyhedron in arbitrary orientation can be obtained. Thus, cubes, prisms, pseudo-spheres, cylinders, and spheroid in arbitrary orientation are all examples of valid targets. Vertices of polyhedron are represented by a three-dimensional list of vertices. Rotation of vertices is performed using a coordinate-free rotation matrix. Thus, averaging over all possible orientations can be performed. A fast ray-convex polyhedron intersection algorithm is used to calculate the phase shift and the extinction and absorption efficiencies are calculated using a two-dimensional quadrature.

6.2 Anomalous diffraction theory — basic concepts

The anomalous diffraction theory is a well established and active field of research. Numerous contributions have been published on various aspects of the theory. Mahood (1987) provides an extensive review of the theory and practical applications. A similar theory comes under the name high-energy or eikonal approximation (Bourrely et al., 1986; Perrin and Lamy, 1986; Perrin and Lamy, 1983; Chen, 1989). Comparisons between high-energy and ADT exist (Debi and Sharma, 1979; Sharma et al., 1981; Sharma et al., 1982; Sharma et al., 1984a). Both methods can be derived from the Maxwell equations written in the integral form (Saxon, 1955). Mostly extinction, absorption, and scattering efficiencies are studied, but certain extensions to small-angle phase function and backscatter are possible (Sharma et al., 1984b; Chen and Hook, 1976; Chen, 1988). Spheres are the most commonly studied (Farone and Robinson, 1968; Ackerman and Stephens, 1987; Chen, 1987), with cylinders coming second (Cross and Latimer, 1970; Bryant and Latimer, 1969; Stephens, 1984). Studies of non-spherical particles include: cube for three particular orientations (Napper, 1966; Napper and Ottewill, 1963), hexagon in particular orientation (Flatau et al., 1988), analytical solution for the hexagon in arbitrary orientation by (Kuznetsov and Pavlova, 1988), disk and ellipsoid of revolution (Bryant and Latimer, 1969), ellipsoids (Latimer, 1975), many-spheres (Chen, 1990), and prisms in particular orientation (Chýlek and Klett, 1991).

Efficiencies in ADT approximation can be calculated by a two-dimensional quadrature. Namely, it can be shown (Bryant and Latimer, 1969) that

$$Q_{ext} = \frac{2}{P} \int (1 - e^{-r} \cos \rho) dP \qquad (6.2.1)$$

and

$$Q_{abs} = \frac{1}{P} \int (1 - e^{-2r}) dP \qquad (6.2.2)$$

where

$$\rho = kd(m_{re} - 1) \qquad (6.2.3)$$

and

$$r = kdm_{im} \qquad (6.2.4)$$

d is the distance inside the particle, wavenumber $k = 2\pi/\lambda$, λ is the wavelength, and the integration is performed over the projected area P. Thus, the basic difficulty of ADT is to find the distance traveled by the light inside a particle. This can be done for most shapes analytically but the resulting expressions are complex and studies are often constrained to particular ("easy") orientations. In the next section we present a new and fast algorithm based on the ray tracing method to get efficiencies (6.2.1) and (6.2.2) for most common shapes and in arbitrary orientation.

6.3 The ray-tracing scheme

To get the distance d needed to calculate the phase shifts (6.2.3, 6.2.4) we use fast ray-convex polyhedron intersection algorithm. This requires defining a target by its vertices.

A target is defined by vertices of a polyhedron v_i, $i = 1, \ldots, n_v$, where v is a vector. More specifically an object is defined as an Indexed_Poly File. Indexed_poly files take advantage of a connectivity list to reduce memory requirements. Thus, for example, a cube is described by eight vertices. The vertices are used in a connectivity list which gives a set of co-planar faces (polygons) defining the object. Thus, a cube would have six such faces. The object can be arbitrarily rotated by three subsequent rotations of vertices. Once the object has been defined we project vertices on a zy-plane, assuming that incoming light is in the positive-x direction. The convex hull (minimum-area convex polygon containing the set of points) of projected vertices (Eddy, 1977; Sedgewick, 1983) and the projected area are calculated. We also define a rectangular grid encompassing the convex hull. For each ray originating on this grid and traveling in the x-direction we calculate the distance inside the polyhedron using a ray-polyhedron intersection algorithm (Haines, 1991). A distance array is formed for arbitrary orientation of an object. A rotated vector v' is given in terms of the original vector v, the axis of rotation a, and the angle of rotation θ as (Leubner, 1979)

$$v' = R(a, \theta)v \qquad (6.3.1)$$

The coordinate-free rotation operator R is given by
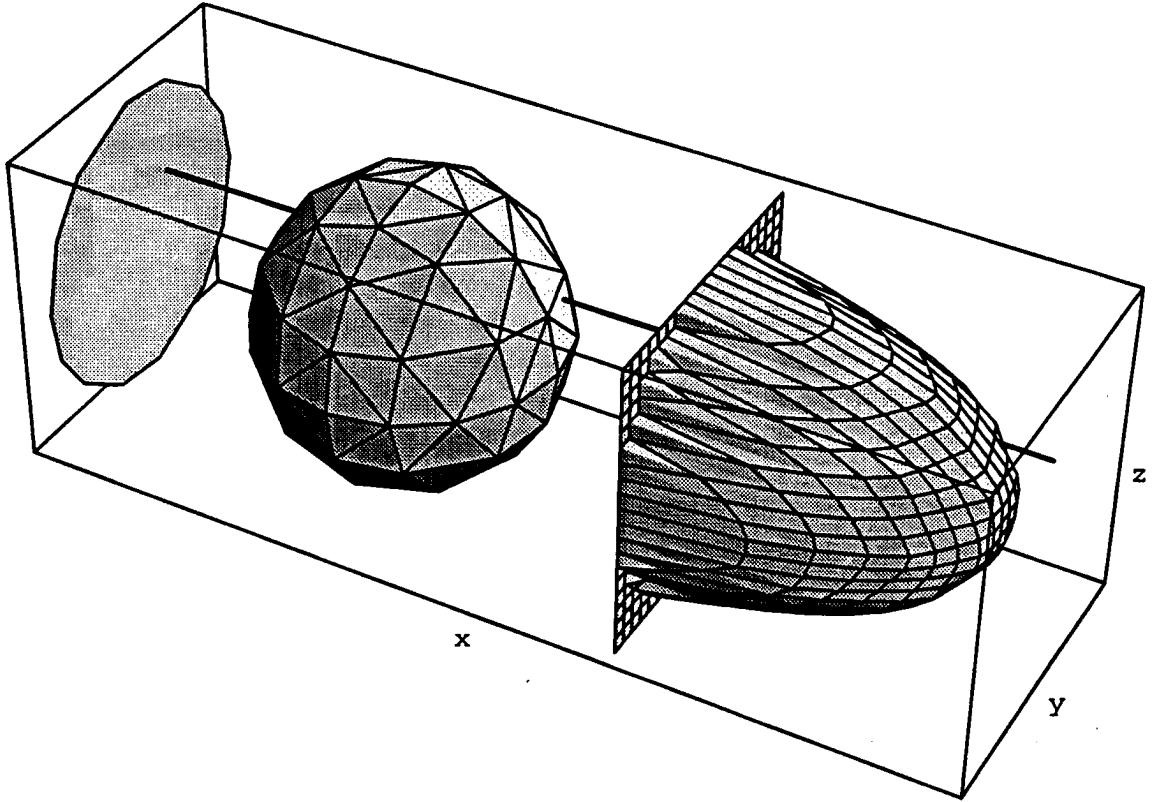
Figure 6.1: Convex polyhedron composed of polygons (center) models pseudo-sphere. No rotation is applied. To the right the shadow of the polyhedron is presented. It is calculated by projecting vertices and calculating their convex hull. To the left distances inside the polyhedron are shown.

$$\mathbf{R}(\mathbf{a}, \theta) = \cos\theta \, \mathbf{1} + (1 - \cos\theta)\mathbf{aa} + \sin\theta \, \mathbf{a} \times \mathbf{1}. \tag{6.3.2}$$

Two successive rotations $\mathbf{v}'' = \mathbf{R}_2(\mathbf{a}, \theta)\mathbf{v}'$ and $\mathbf{v}' = \mathbf{R}_1(\mathbf{a}, \theta)\mathbf{v}$ combine as $\mathbf{v}'' = \mathbf{R}(\mathbf{a}, \theta)\mathbf{v}$ where $\mathbf{R} = \mathbf{R}_2\mathbf{R}_1$.

If needed, a target can be rotated. Specification of rotations is performed as follows: The target is assumed to have two vectors $\mathbf{a}_1$ and $\mathbf{a}_1$ embedded in it; $\mathbf{a}_2$ is perpendicular to $\mathbf{a}_1$. The target orientation in the laboratory frame is set by three angles: β, θ, and φ. The polar angles θ and φ specify the direction of $\mathbf{a}_1$ in the laboratory frame. The target is assumed to be rotated around $\mathbf{a}_1$ by an angle β. The angles β, θ, and φ sample the intervals $(\beta_{min}, \beta_{max})$, $(\theta_{min}, \theta_{max})$, $(\varphi_{min}, \varphi_{max})$. The prescription for choosing the angles is to uniformly sample in β, φ, and $\cos\theta$. This prescription represents random orientation within the specified limits of β, θ, and ϕ. True random orientation would, in principle,

be represented by β, θ, and φ in the intervals $(0, 360)$, $(0, 180)$, $(0, 360)$. The validity of the ADT integration scheme is established using several different tests. We checked if the randomly-averaged projected area is linearly related to the total surface area of an object (Vouk, 1948). We have also compared our ADT calculations with the analytical results for spheres. Three datasets have been used with 2046 faces and 1026 vertices, 512 faces and 258 vertices, 128 faces and 66 vertices. The results for 2046 (solid line) and 512 (dotted line) are very similar. The exact ADT calculations overlap with the numerical ones. The approximation with 128 vertices (dashed line in Fig. 6.2) doesn't approximate the analytical solution well because the resulting polyhedron doesn't approximate a sphere.

6.4 Results

In order to compare DDA with ADT we report the results of DDA calculations for absorption and extinction by a single cube. Results for the refractive index $m = 1.33 + 0.01i$ and $m = 1.33 + 0.001i$ are presented. The range $x = 0.5 - 20$ of size parameters is used. Notice that small size parameters are outside the validity of the ADT assumptions, so large errors there are of no consequence. However, the size parameters of the order of 10 are meaningful in the context of a ADT vs. DDA comparisons. For such values of refractive index and size parameter the ADT for spheres is considered to be a good approximation. Figures 6.3 and 6.4 presents Mie vs. ADT comparisons of (a) extinction and (b) absorption for spheres. The extinction maxima and minima are well reproduced. The fractional error for extinction (not presented) is generally below 30 percent. The ADT absorption follows qualitatively that obtained from the Mie solution. However, the values are under-predicted. This behavior is well known and semi-empirical remedies are possible (Ackerman and Stephens, 1987).

The two cube orientations have been used: $\theta = 0$ (edge incidence) and $\theta = 45$ (side incidence). These two cases are illustrated in Figs 6.5 and 6.6. These figures show the DDA targets resolved on the $32 \times 32 \times 32$ lattice. Resolution of the cubic lattice was varied to keep the dipole-size related parameter $|m|kd$ in the $0.6 - 1$ range and computational time is manageable. Thus, for $x = 0.5 - 5$ we used $16 \times 16 \times 16$ lattice, for $x = 5.5 - 10$

we used $25 \times 25 \times 25$ lattice, for $x = 10.5 - 15$ we used $32 \times 32 \times 32$ lattice, and for larger x both $40 \times 40 \times 40$ and $50 \times 50 \times 50$ resolution have been used. In other words, the amount of dipoles used varied between $N = 4096$ and $N = 125000$. The fractional error convergence criterion for the conjugate gradient solver was set in the 10^{-5} and 10^{-3} range. Less precision was requested for larger size parameters to reduce computer time. The extinction for $m = 1.33 + 0.01i$ is presented in Fig. 6.7.

Results for $\theta = 45$ (Fig. 6.7b) show fairly good agreement between the two methods. The error is similar to that observed between Mie vs. ADT (for spheres) in this size parameter range. Surprisingly, the $\theta = 0$ case (Fig. 6.7a), for the same refractive index, shows much larger deviations. In Fig. 6.8 fractional error of extinction efficiency is presented. The maximum error is about 80 percent at $x = 11.5$. Also, in this case, the ADT maximum predicted at $x = 6$ is shifted by $\Delta x \approx 1$ in comparison to the DDA. Similar disagreement, slightly more pronounced, can be observed for extinction in the $m = 1.33 + 0.001i$ case; c.f. Fig. 6.9.

Figures 6.10 and 6.11 show absorption efficiencies for $m = 1.33 + 0.01i$ and $m = 1.33 + 0.001i$, respectively. A qualitative behavior is similar to that for Mie vs. ADT for spheres. Absorption seems to be dependent on equivalent volume. Such qualitative behavior indicates that absorption for cubes, in this size range, can be approximated by the ADT. However, additional empirical corrections are needed, perhaps in a similar fashion to corrections for spheres (Ackerman and Stephens, 1987). It is not clear if similar corrections can be developed for scattering and extinction efficiencies because they would have to be shape dependent.

6.5 Summary

We developed a new method to perform the anomalous diffraction theory calculations for irregular particles. This method should be of use for remote sensing particle methods and a basis for simple parameterization schemes. To this author's knowledge, the first comparisons of the ADT for a non-spherical particle with the exact solution are reported here. The results show that DDA and ADT results are not in agreement for the face-in

light incidence close to the values of size parameter where constructive and destructive interference is taking place. However, the results compare well for other orientations studied. The absorption efficiency is under-predicted but the qualitative behavior is in agreement and suggests a simple relation to the volume of the particle. This fact makes it possible to introduce semi-empirical corrections to absorption efficiencies.
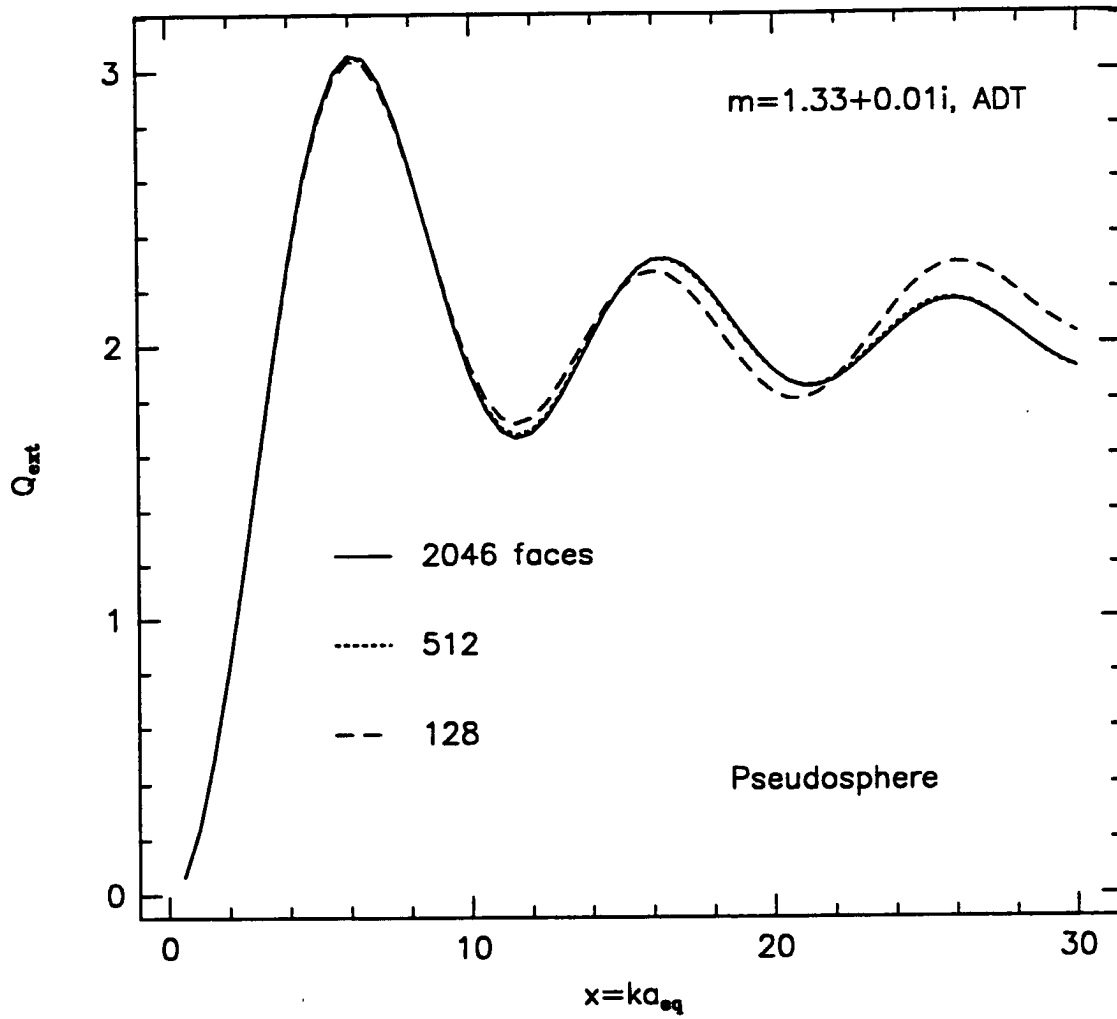
Figure 6.2: Extinction efficiency factor Q_{ext} for pseudo-spheres approximating sphere with 2046, 512, and 128 faces. Results are shown for the ADT method as function of $x = ka_{eq}$.
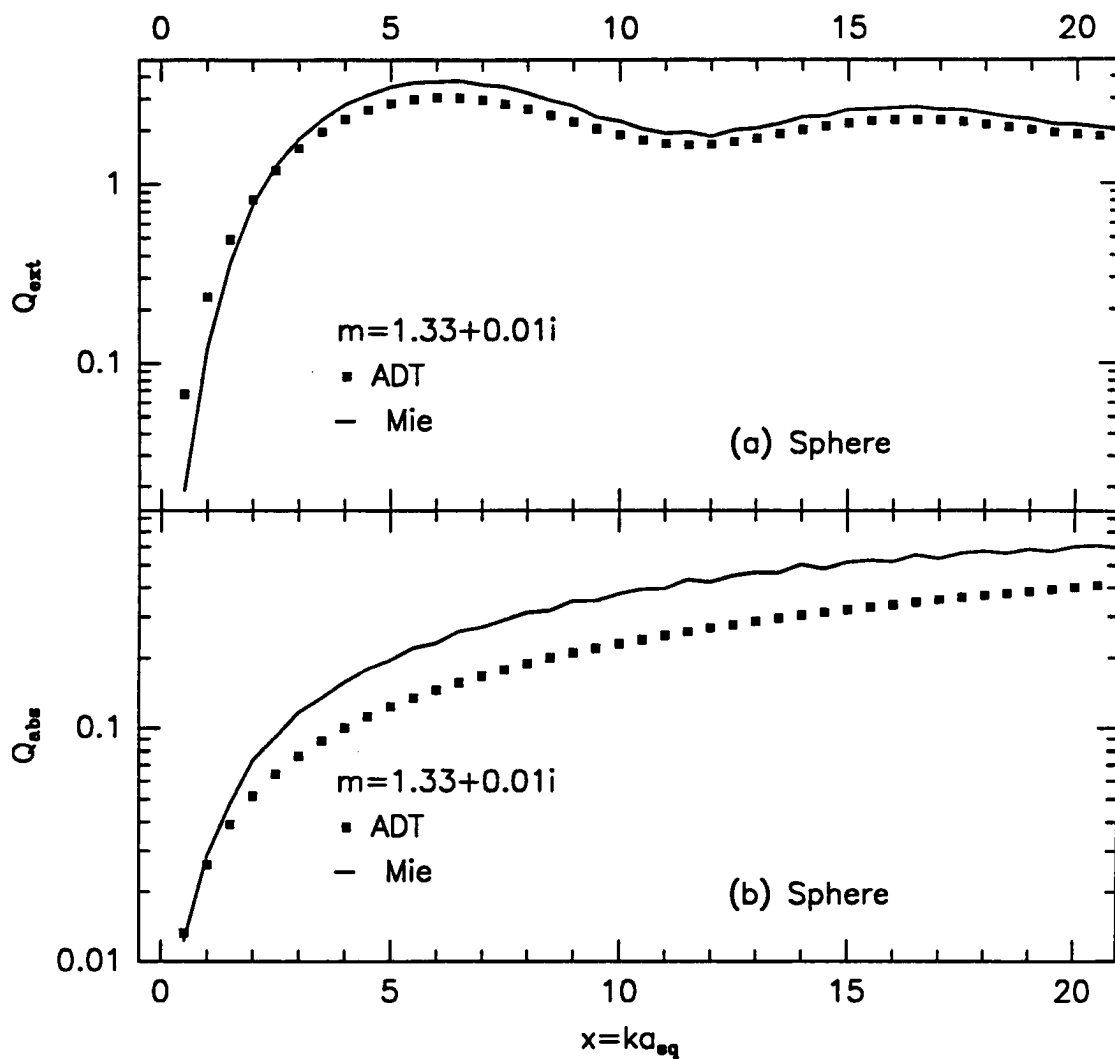
Figure 6.3: (a) Extinction efficiency factor Q_{ext}. (b) Absorption efficiency factor Q_{abs}. Results are shown for the Mie and ADT methods for sphere of refractive index $m = 1.33 + 0.01i$ as functions of $x = ka_{\text{eq}}$.
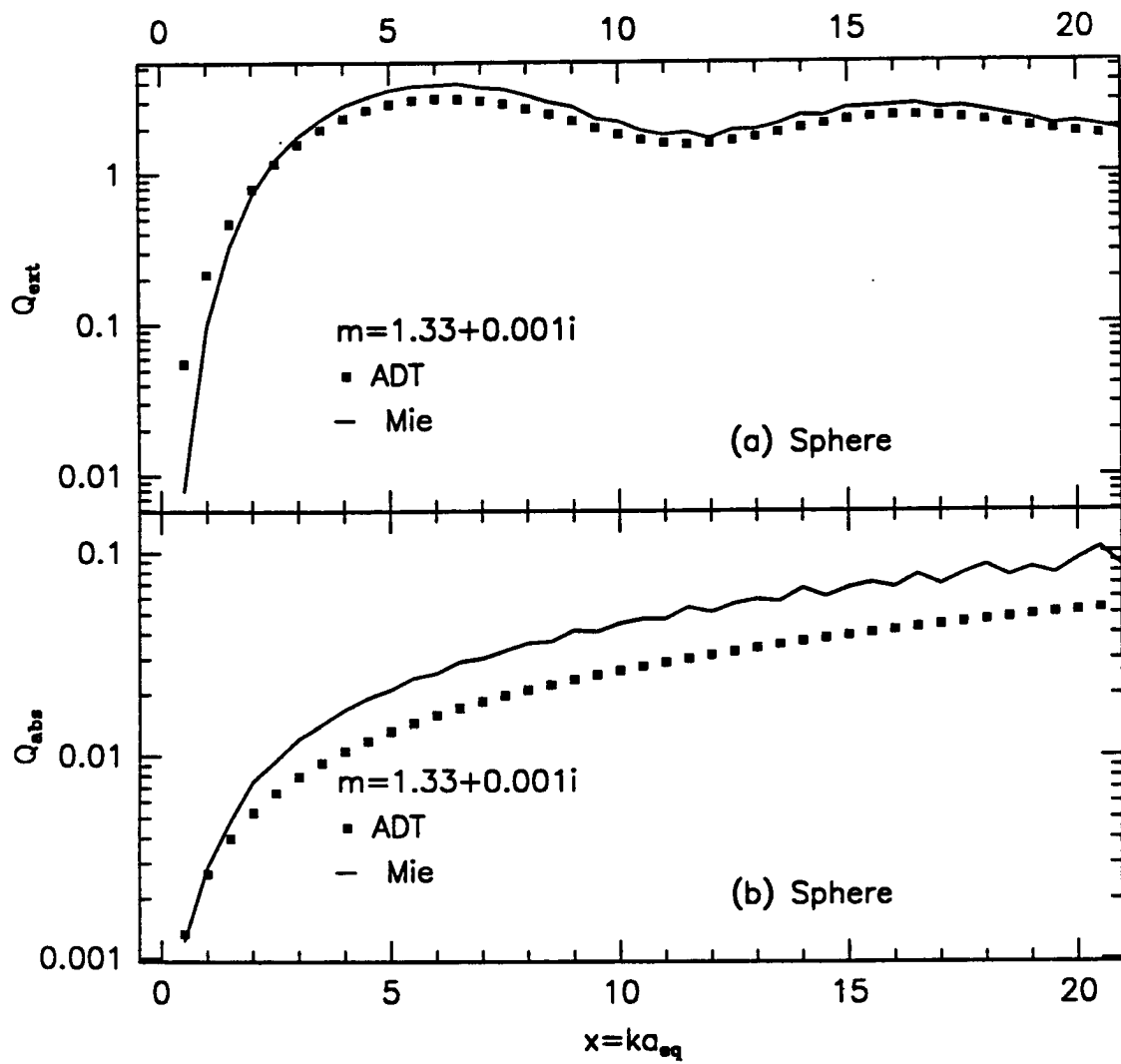
Figure 6.4: Same as in Fig. 6.3 but for $m = 1.33 + 0.001i$.

Pseudocube

$N=32768$ ($\theta=0$ $\varphi=0$ $\beta=0$)
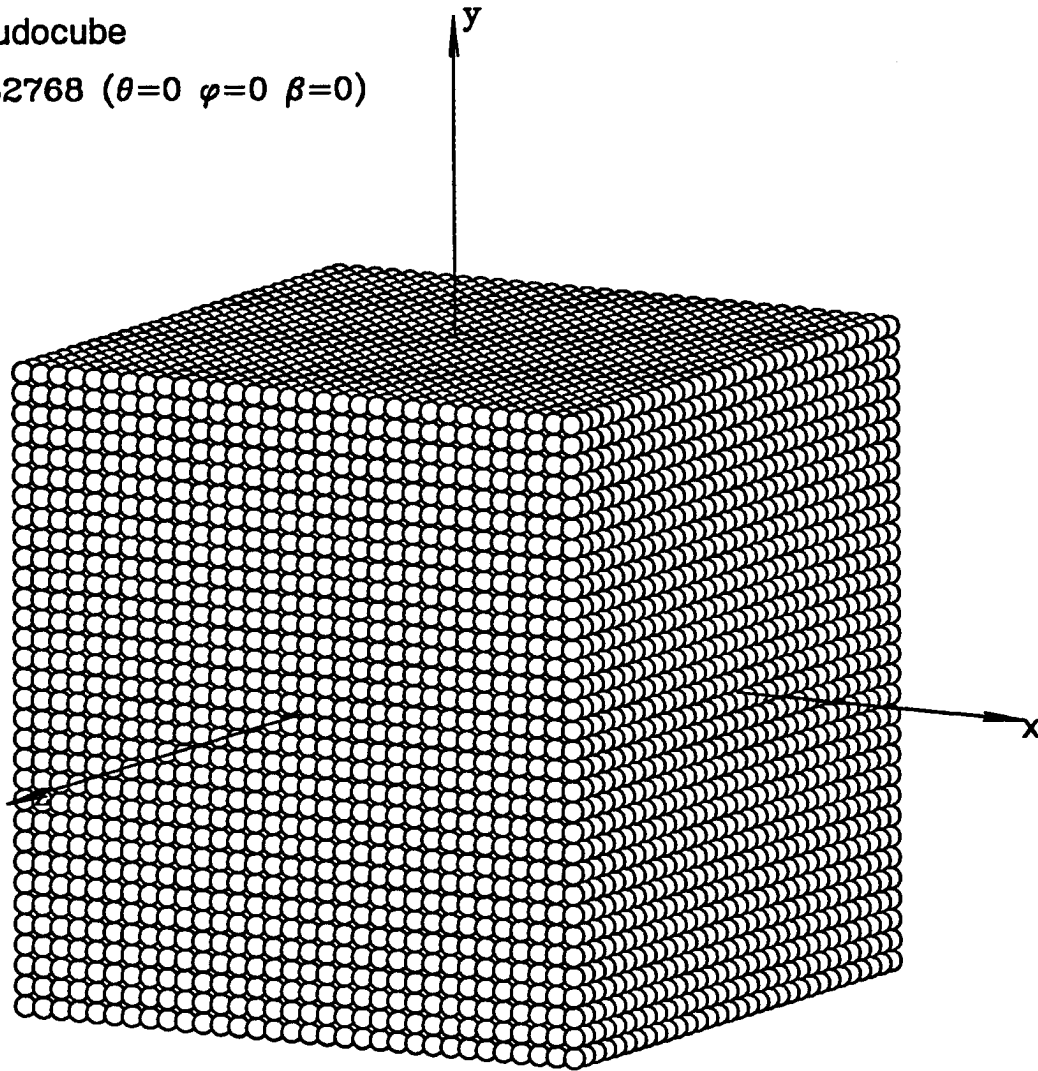
Figure 6.5: Pseudo-cube composed of $32 \times 32 \times 32$ dipoles on cubical lattice. The light is propagating along the x-axis. This is side incidence or $\theta = 0$ case.
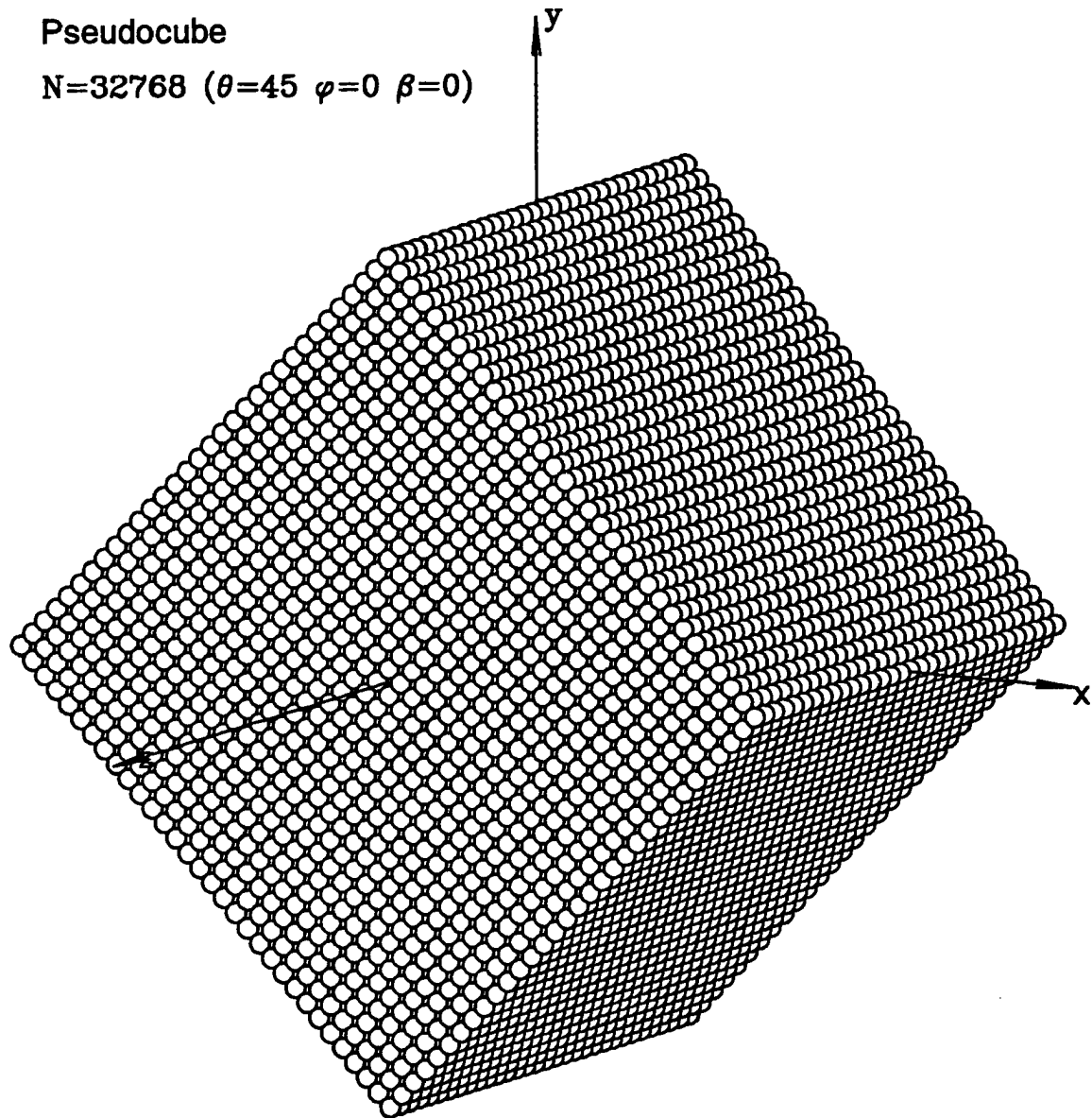
Figure 6.6: Same as in Fig. 6.5 but for the edge incidence, $\theta = 45$ case.
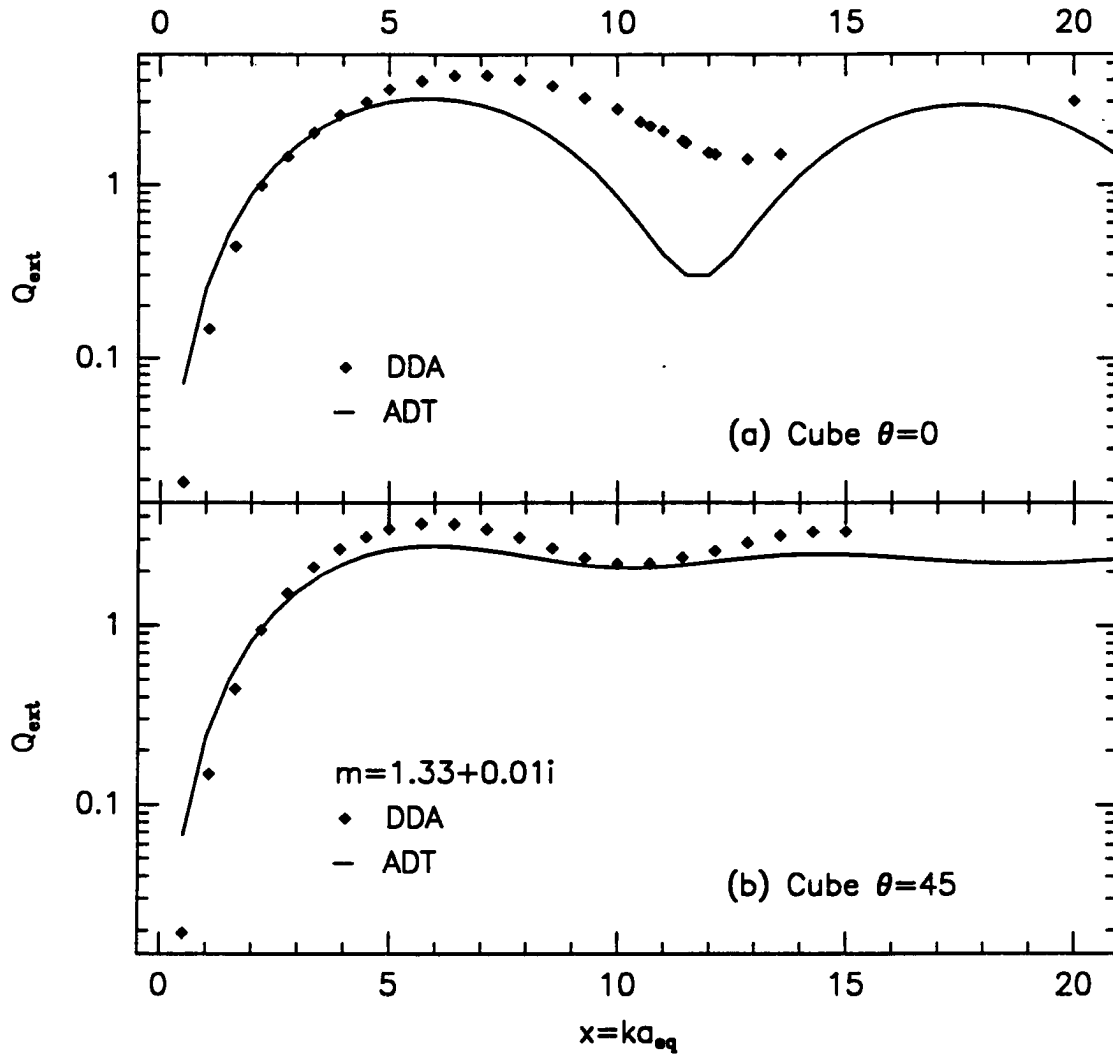
Figure 6.7: (a) Extinction efficiency factor Q_{ext} for $\theta = 0$ case. (b) Extinction efficiency factor Q_{ext} for $\theta = 45$ case. Results are shown for the DDA and ADT methods for cube of refractive index $m = 1.33 + 0.01i$ as functions of $x = ka_{eq}$.
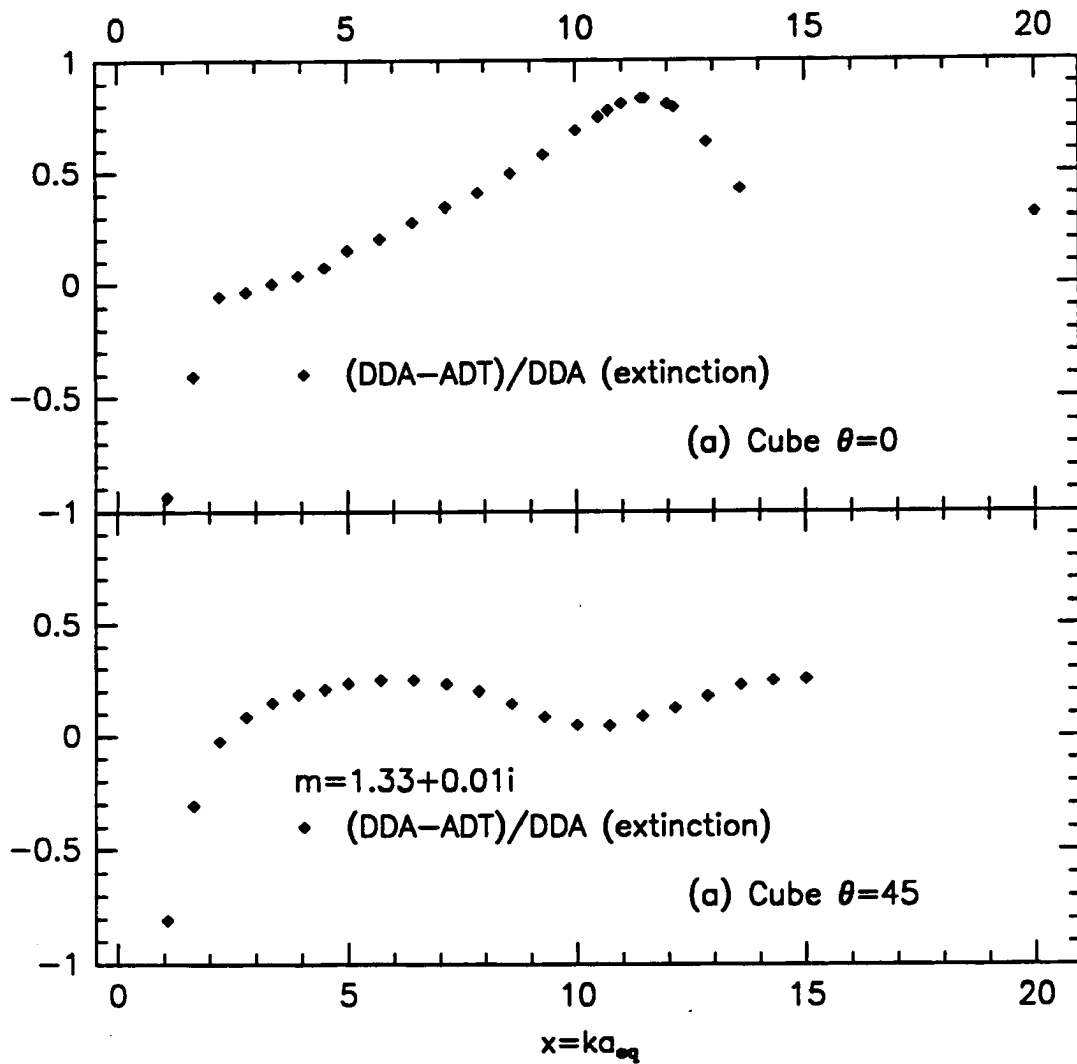
Figure 6.8: (a) Fractional error (DDA-ADT)/DDA for extinction efficiency factor Q_{ext} and $\theta = 0$ case. (b) Fractional error (DDA-ADT)/DDA for extinction efficiency factor Q_{ext} and $\theta = 45$. Results are shown for cube of refractive index $m = 1.33 + 0.01i$ as functions of $x = ka_{eq}$.
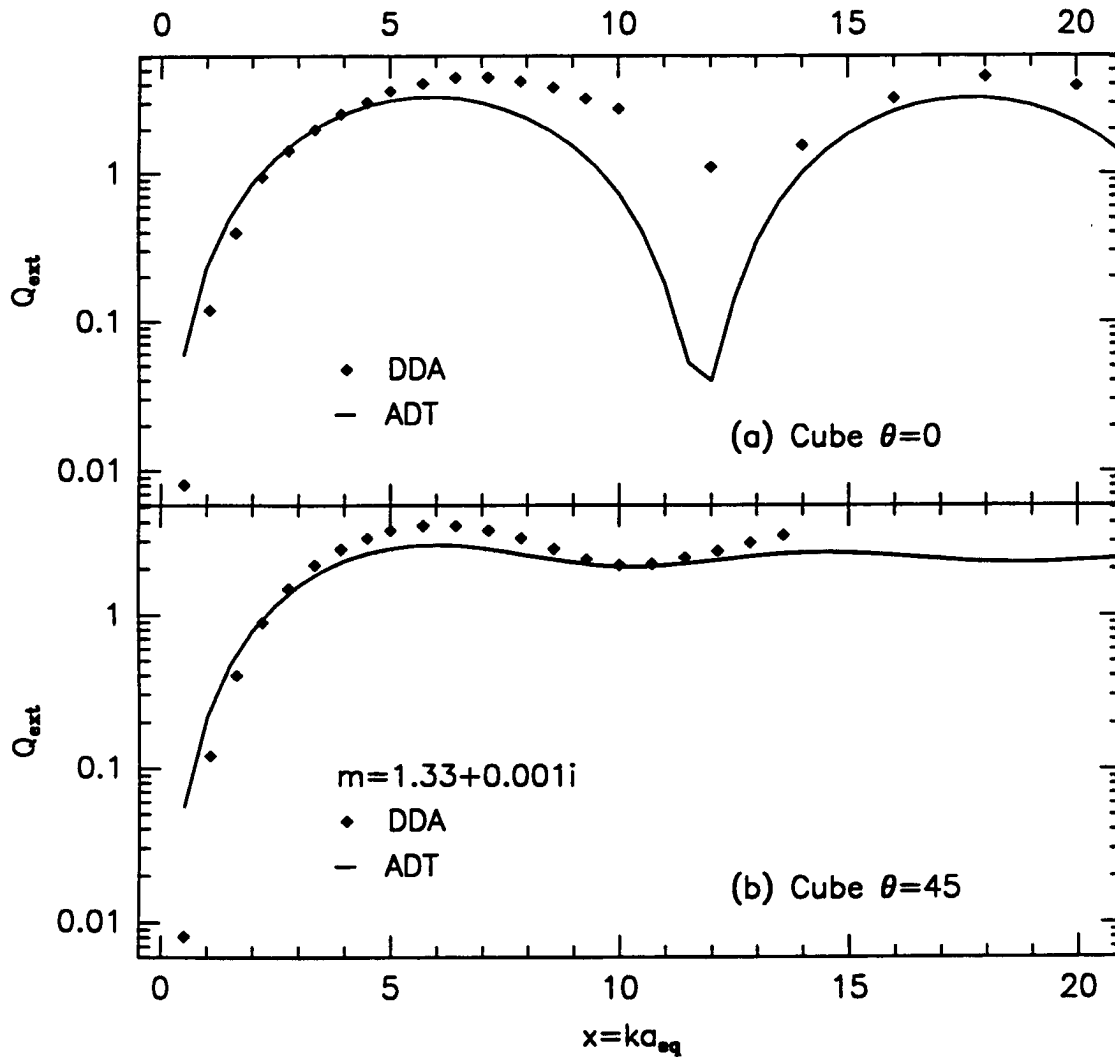
Figure 6.9: Same as in Fig. 6.7 but for $m = 1.33 + 0.001i$.
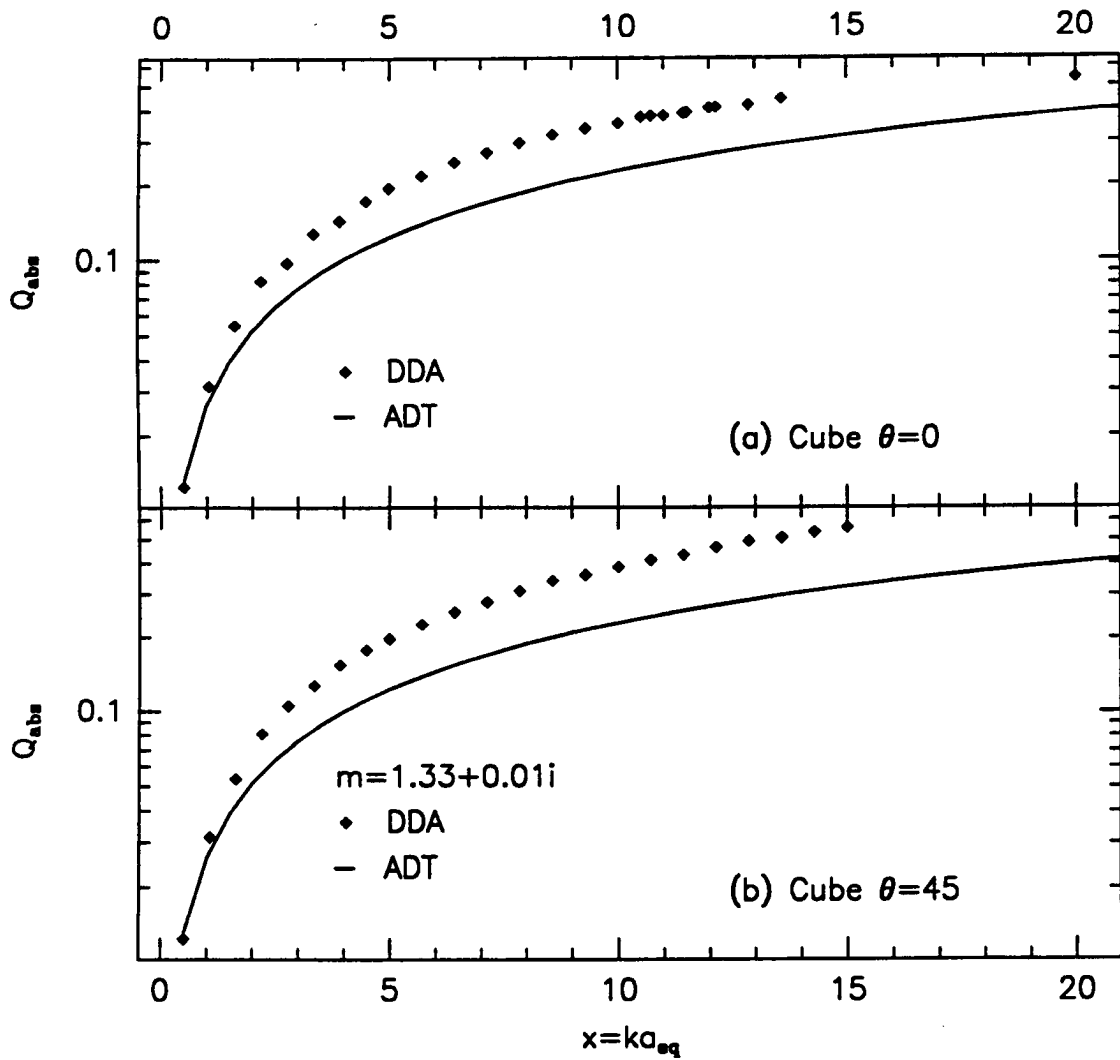
Figure 6.10: (a) Absorption efficiency factor Q_{abs} for $\theta = 0$ case. (b) Absorption efficiency factor Q_{abs} for $\theta = 45$. Results are shown for the DDA and ADT methods for cube of refractive index $m = 1.33 + 0.01i$ as functions of $x = ka_{eq}$.
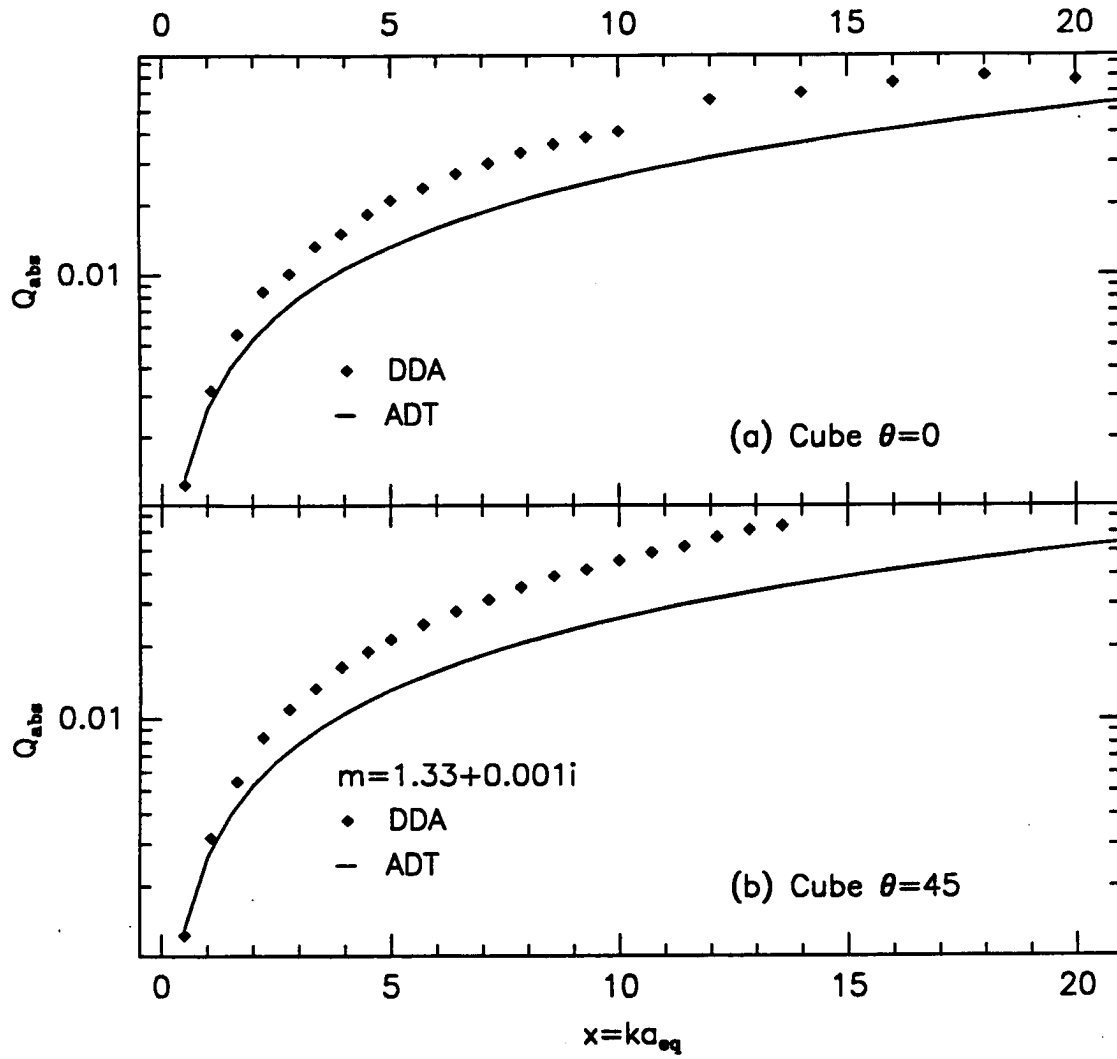
Figure 6.11: Same as in Fig. 6.10 but for $m = 1.33 + 0.001i$.

Chapter 7

SCATTERING IN ANOMALOUS DIFFRACTION APPROXIMATION

7.1 Introduction

This chapter deals with scattering properties of an ensemble of particles defined by a simple size distribution. The objective is to develop a single scattering parameterization compatible in simplicity with bulk-type microphysics schemes e.g. Flatau et. al. (1989) as currently used in mesoscale and global numerical prediction models. The goal is elusive and bordering on impossible due to the variety of shapes, unknown orientations, unknown size distributions, difficulties in theoretical scattering calculations, lack of comprehensive measurements, and constraints that the scheme has to be numerically robust. No such scheme is in existence.

We attack the problem by formulating the particle ensemble equivalent to the Anomalous Diffraction Theory for a single sphere. It is shown that two functions, $\mathcal{K}$ for single scattering properties and $\mathcal{M}$ for averaged single scattering properties come to play. By performing an asymptotic analysis, an empirical correction to the expressions for $\mathcal{K}$ and $\mathcal{M}$ is introduced. We use the scaling parameter $v = xn'$, arising in the ADT formulation, to plot results of Mie calculations. This confirms that the corrected ADT using v-scaling gives an approximate fit to Mie solutions. Encouraged by this development we assume that the methodology can be extrapolated to irregular particles. The underlying assumption is that the particle's irregularity is similar in effect to the averaging property of the size spectrum. This then leads to a search for the modified $\mathcal{K}$ function for non-spherical particles. Once $\mathcal{K}_{irr}$ is determined all averaged properties can be found from the modified $\mathcal{M}_{irr}$. These $\mathcal{M}$ functions are particle and orientation dependent. To test the assumptions we use two spheres in contact as a model for an irregular particle. It is shown that, indeed,

self-similar scaling with respect to v is possible in a such case. Thus, it is proposed to use sets of $\mathcal{M}$ functions as a basis for the bulk single scattering radiative parameterization scheme for an ensemble of irregular particles.

7.2 Preliminaries. Size distribution, related integrals, definitions

The ensemble averaged absorption and extinction coefficients require information about the size spectrum and a judicious choice of the analytical representation of this spectrum, together with expressions for the scattering efficiencies has to be made to progress the theory. This is the main reason why the anomalous diffraction theory (ADT) is invoked here together with the gamma size distribution. To establish notation we begin with the definition of volume coefficients, gamma distribution and its moments. The volume absorption coefficient is

$$\beta_{abs} = \int_0^\infty \pi r^2 n(r) Q_{abs}(r) dr = 2 \int_0^\infty \pi r^2 \left(\frac{1}{2} + \frac{e^{-yr}}{yr} + \frac{e^{-yr} - 1}{(yr)^2} \right) n(r) dr. \qquad (7.2.1)$$

and the volume extinction coefficient is

$$\beta_{ext} = \int_0^\infty \pi r^2 n(r) Q_{ext}(r) dr = 4\mathrm{Re} \left\{ \int_0^\infty \pi r^2 \left(\frac{1}{2} + \frac{e^{-zr}}{zr} + \frac{e^{-zr-1}}{(zr)^2} \right) n(r) dr \right\} \qquad (7.2.2)$$

where the ADT formulation for Q_{abs} and Q_{ext} has been applied in the right hand side equations. The size distribution $n(r)$ in (7.2.1) and (7.2.2) is assumed to be

$$n(r) dr = \frac{N_t}{\Gamma(\alpha)} \left(\frac{r}{r_n} \right)^{\alpha-1} \exp\left(-\frac{r}{r_n} \right) d\left(\frac{r}{r_n} \right) \qquad (7.2.3)$$

which is capable of representing a wide range of distributions that represent clouds in the real atmosphere. The r_n is convenient, but non-measurable, "characteristic" radius and α is a measure of the variance of the distribution. Its meaning can be explain by the following example: Consider the total area of all particles. It is defined by

$$A = \int_0^\infty \pi r^2 n(r) dr = N_t \pi r_n^2 F(2) \qquad (7.2.4)$$

where $F(2)$ is constant defined by (7.2.12). Thus, the total area is the area of a "characteristic" particle of radius r_n, i.e. πr_n^2 multiplied by the total number of particles, and adjusted by constant $F(2)$. It is also convenient now to define liquid water content

$$q = \int_0^\infty m(r) n(r) dr \qquad (7.2.5)$$

where mass is given by

$$m(r) = \frac{4}{3}\pi r^3 \rho \qquad (7.2.6)$$

Thus, it follows that

$$q = \frac{4}{3}\pi \rho N_t r_n^3 F(3) \qquad (7.2.7)$$

The liquid water content is related to mixing ratio via

$$r = \frac{1}{\rho_0} q \qquad (7.2.8)$$

and the liquid or ice path (LWP or IWP) are column integrated quantities, namely

$$LWP = \int q(z)dz \qquad (7.2.9)$$

Finally, to integrate (7.2.1) and (7.2.2) we need the following results

$$\int_0^\infty r^p n(r)dr = N_t r_n^p F(p) \qquad (7.2.10)$$

and

$$\int_0^\infty e^{-zr} r^p n(r)dr = N_t r_n^p F(p)\frac{1}{(zr_n + 1)^{\alpha+p}} \qquad (7.2.11)$$

where

$$F(p) = \frac{\Gamma(\alpha + p)}{\Gamma(\alpha)}. \qquad (7.2.12)$$

It can be shown that $F(0) = 1$, $F(1) = \alpha$, $F(2) = (\alpha + 1)\alpha$, $F(3) = (\alpha + 2)(\alpha + 1)\alpha$. Of importance in what follows are two non-dimensional parameters

$$u = x(n - 1) \qquad (7.2.13)$$

$$v = xn' \qquad (7.2.14)$$

where x is the size parameter defined for spherical paticles of radius r as

$$x = \frac{2\pi r}{\lambda} \qquad (7.2.15)$$

From discussion of the "characteristic" particle size r_n we expect that the values of v_n and u_n at characteristic radius r_n are of importance

$$v_n = x_n n' \quad u_n = x_n(n - 1). \qquad (7.2.16)$$

and

$$w_n = v_n + iu_n \tag{7.2.17}$$

It is also relevant to note that the connection between r_n and the effective radius e_e is

$$r_e = (\alpha + 2)r_n \tag{7.2.18}$$

7.3 van de Hulst (ADT) and Bohren and Nevitt (BNA) approximations

In this section we present, in a consistent way, expressions for the distribution-averaged efficiencies in van de Hulst's (1957) and Bohren and Nevitt's (1983) approximations. The ADT theory is nominally valid for $x \gg 1$ and $\mid m - 1 \mid \ll 1$, where

$$m = n - in' \tag{7.3.1}$$

is complex refractive index. The semi-empirical correction developed here, on the basis of asymptotic behavior, extends its applicability. Since, within the framework of approximate theories, there are similarities between non-averaged and averaged properties we carry the analysis in parallel.

7.3.1 Absorption efficiencies

In anticipation of what follows we begin by introducing two related functions $\mathcal{K}$ and $\mathcal{M}$

$$\mathcal{K}(w) = \frac{1}{2} + \frac{\exp(-w)}{w} + \frac{\exp(-w) - 1}{w^2} \tag{7.3.2}$$

and $\mathcal{M}$

$$\mathcal{M}(w) = \frac{1}{2} + \frac{1}{\alpha(\alpha+1)} \left[\frac{\alpha}{w(w+1)^{\alpha+1}} + \frac{1}{w^2(w+1)^\alpha} - \frac{1}{w^2} \right] \tag{7.3.3}$$

where α is a parameter appearing in the definition of gamma size distribution (7.2.11) and w can is either real or complex argument. Together they, and their variants, describe the single scattering properties of single and distribution-averaged particles. Figure 7.1a shows a graph of $\mathcal{K}(w)$ (solid line) and $\mathcal{M}(w, \alpha = 2)$ (dashed line). The functions asymptote for large w to 1/2 and to 0 for small w. They have similar behavior and they appear to be"shifted" with respect to each other. In terms of (7.3.2) the absorption factor in the
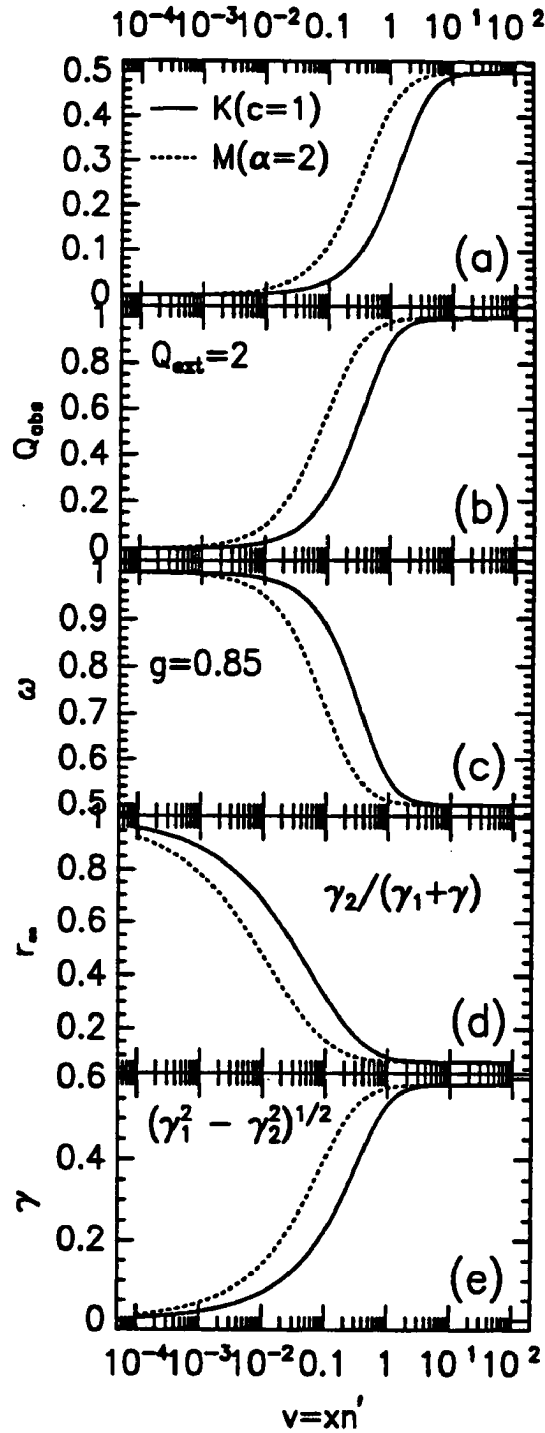
Figure 7.1: (a) $\mathcal{K}(w)$ (solid line) and $\mathcal{M}(w)$ (dashed line) as functions of the real argument v. (b) Q_{abs} (solid line) and gamma distribution averaged Q_{abs} for the parameter $\alpha = 2$ (c) single scattering albedo ω (solid line) and distribution averaged ω (dashed line) for $Q_{ext} = 2$ (d) reflectivity of the infinite medium (for $g = 0.85$ and $Q_{ext} = 2$ (e) eigenvalue arising in a two-stream model.

ADT is (Smith, 1982)

$$Q_{abs} = 2\mathcal{K}(4v) \tag{7.3.4}$$

where $\mathcal{K}(v)$ is function of the real argument v. Using (7.2.10-7.2.11) we get

$$\beta_{abs} = 2A\mathcal{M}(4v_n) \tag{7.3.5}$$

where the total surface area A is defined in (7.2.4). Equations (7.3.4) and (7.3.5) illustrate the formal similarity between single and distribution-averaged properties. The result (7.3.5) can be specialized for particular values of parameter α describing the width of size distribution. For example for $\alpha = 1$

$$\beta_{abs} = A - \frac{A}{(4v_n + 1)^2} \tag{7.3.6}$$

and for $\alpha = 2$

$$\beta_{abs} = A - \frac{A}{3}\frac{4v_n + 3}{(4v_n + 1)^3} \tag{7.3.7}$$

The plot of Q_{abs} is given in Figure 7.1b (solid line) for both single and distribution-averaged ($\alpha = 2$) cases as a function of $v = xn'$ (7.2.14); for the distribution-averaged case v_n defined in (7.2.16) is employed. For fixed vales of wavelength, characteristic radius, and complex part of refractive index, absorption is greater for the distribution-averaged case. However, v_n has to be carefully related to measurable quantities as discussion of the characteristic radius in the introductory comments in this chapter indicates.

The alternative to ADT is the geometric optics based approximation developed by Bohren and Nevitt (1983). This approximation, unlike ADT, gives the correct small and large particle limits for absorption efficiencies and therefore it offers certain advantages over the ADT approximation. The Bohren and Nevitt approximation (BNA) results can also be cast in terms of $K(w)$ making this function of unifying importance for the present development. The absorption efficiency is given as

$$\hat{Q}_{abs} = c\left[2\mathcal{K}(4v) - a^2\mathcal{K}(a4v)\right] \tag{7.3.8}$$

and for the distribution-averaged case replacement of $\mathcal{K}$ with $\mathcal{M}$ carries over from the ADT approximation. This gives

$$\hat{Q}_{abs} = cA\left[2\mathcal{M}(4v) - a^2\mathcal{M}(a4v)\right] \tag{7.3.9}$$

where

$$a = \frac{(n^2 - 1)^{1/2}}{n} \tag{7.3.10}$$

and

$$c = \frac{4n^3}{(n + 1)^2 - (n - 1)^2 \exp(-4v)} \approx \frac{4n^3}{(n + 1)^2 - (n - 1)^2} \tag{7.3.11}$$

last approximation holds for n close to 1. Thus (7.3.8) and (7.3.9) allow us to interpret the BNA as a correction to ADT. It enhances ADT by a factor c and reduces it by the correction $a^2 K(a4v)$. For $n = 1$ both approximations are equivalent and the BNA has proper limits for both small and large v. Figure 7.2 shows comparison between BNA (solid line) and ADT (dashed line) absorptions as a function of v for fixed real part of refractive index.

The importance of (7.3.9) goes beyond the corrections it introduces for spheres. From the purely mathematical standpoint (7.3.9) can be treated as a function of v with two free parameters a and c. These two parameters control the "shift" and asymptotic behavior. We expect, on purely intuitive grounds, that the irregular particles would also have well defined asymptotic properties (but not necessarily the same as spherical particles), and that the effect of non-sphericity will also be to "shift" the absorption curve. If this is so eq. (7.3.9) can be used as a trial function with a and c selected by a suitable optimization technique using results from more complex scattering theories. We will discuss this concept further.

7.3.2 Extinction efficiency

The extinction efficiency can be related to $\mathcal{K}$ and $\mathcal{M}$ functions in a similar way. From the definition

$$Q_{ext} = 4\text{Re}\{\mathcal{K}(2(v + iu))\} \tag{7.3.12}$$

We note that (7.3.12) is a function of two arguments u and v. Thus, extinction and extinction-related functions, cannot be expected to scale with v only. The volume extinction efficiency is given by

$$\beta_{ext} = 4A\text{Re}\{\mathcal{M}(2w_n)\} \tag{7.3.13}$$
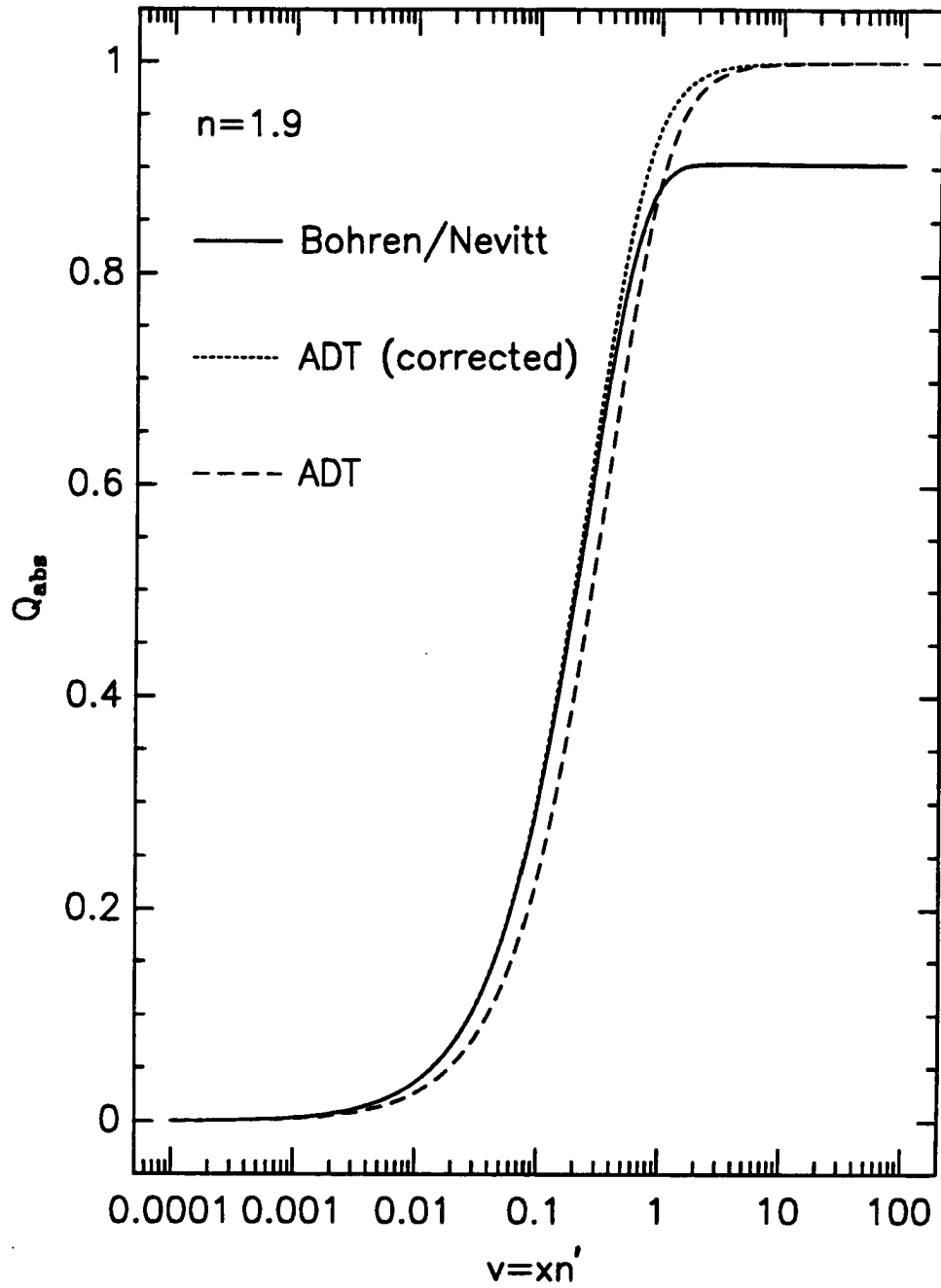
Figure 7.2: Comparison of BNA (solid line), corrected ADT (dotted line) and ADT (dashed line).

Equation (7.3.13) has simple form for small integer values of α. For $\alpha = 1$ we have

$$\beta_{\text{ext}} = 2A - \text{Re}\left\{\frac{2A}{(2w_n + 1)^2}\right\} \tag{7.3.14}$$

and for $\alpha = 2$

$$\beta_{\text{ext}} = 2A - \frac{2A}{3}\text{Re}\left\{\frac{2w_n + 3}{(2w_n + 1)^3}\right\} \tag{7.3.15}$$

The extinction efficiency for large sphere tends asymptotically to 2. This provides a convenient mechanism which avoids treatment of (7.3.12) as a function of two variables. Convenient as it is, it is not a perfect approximation and leads to a departure of the approximate theories from exact calculations.

7.3.3 Single scattering albedo

The single scattering albedo is defined as

$$\omega = 1 - Q_{\text{abs}}/Q_{\text{ext}} \tag{7.3.16}$$

or as

$$\omega = 1 - \beta_{\text{abs}}/\beta_{\text{ext}} \tag{7.3.17}$$

for a distribution averaged albedo. It is straightforward to determine (7.3.16) from absorption (7.3.4) and extinction efficiencies (7.3.12). Figure 7.1c presents the single scattering albedo derived with $Q_{\text{ext}} = 2$ and plotted as a function of v. This choice avoids complications related to the dependence of (7.3.12) on complex argument. We will show that Mie calculations scaled by v alone are in remarkable agreement with Fig. 7.1c. The distribution averaged single scattering albedo is given in the ADT approximation by

$$\tilde{\omega} = 1 - \frac{2\mathcal{M}(4v_n)}{4\text{Re}\{\mathcal{M}(2w_n)\}} \tag{7.3.18}$$

Assuming that $\beta_{\text{sca}} = 2A$ we get the following approximation

$$\tilde{\omega} = \frac{1}{2} - \frac{1}{(\alpha + 1)\alpha}\left[\frac{\alpha}{v_n(v_n + 1)^{\alpha+1}} + \frac{1}{v_n^2(v_n + 1)^\alpha} - \frac{1}{v_n^2}\right] \tag{7.3.19}$$

It can be shown that for conservative scattering ($v_n = 0$), gives $\tilde{\omega} = 1$ as expected.

7.4 Corrections to ADT

The BNA approximation has correct asymptotic limits. It is therefore reasonable to ask if the ADT can modified such that the asymptotic limits are satisfied. Using both small and large parameter expansions, we introduce scaling of v to improve on ADT.

7.4.1 Small v approximations

For small w, (7.3.2) has series representation

$$\mathcal{K}(w) \approx \frac{1}{3}w - \frac{1}{8}w^2 + \frac{1}{30}w^3 \tag{7.4.1}$$

and similarly

$$\mathcal{M} = \left(\frac{1}{3}\alpha + \frac{2}{3}\right)w - \left(\frac{1}{8}\alpha^2 + \frac{5}{8}\alpha + \frac{3}{4}\right)w^2 \tag{7.4.2}$$

for small w. Equation (7.4.1) leads to the following series expansions for the ADT

$$Q_{abs} = \frac{8}{3}v - 4v^2 + \frac{64}{15}v^3 \tag{7.4.3}$$

Notice that the coefficient of the linear term doesn't depend on refractive index. Equation (7.4.2) can be written as

$$\beta_{abs} = (\frac{8}{3}\alpha + \frac{16}{3})Av_n - (4\alpha^2 + 20\alpha + 24)Av_n^2 \tag{7.4.4}$$

From the BNA, we have

$$\hat{Q}_{abs} = \frac{8}{3}n^2(1 - a^3)v \tag{7.4.5}$$

which is the proper limit for small v (Bohren and Nevitt, 1983). Linear and quadratic approximations to Q_{abs} are presented in Figure 7.3. These low order approximations work well for $v < 0.1$, approximately. The BNA has similar qualitative behavior. However, the limit for large v depends slightly on the real part of refractive index and is given by

$$\hat{Q}_{abs} = \frac{4n^3}{(n+1)^2}(1 - a^2) = \frac{4n}{(n+1)^2} \tag{7.4.6}$$

Table 7.1 presents coefficient b_λ of the linear approximation

$$Q_{abs} = b_\lambda x \tag{7.4.7}$$
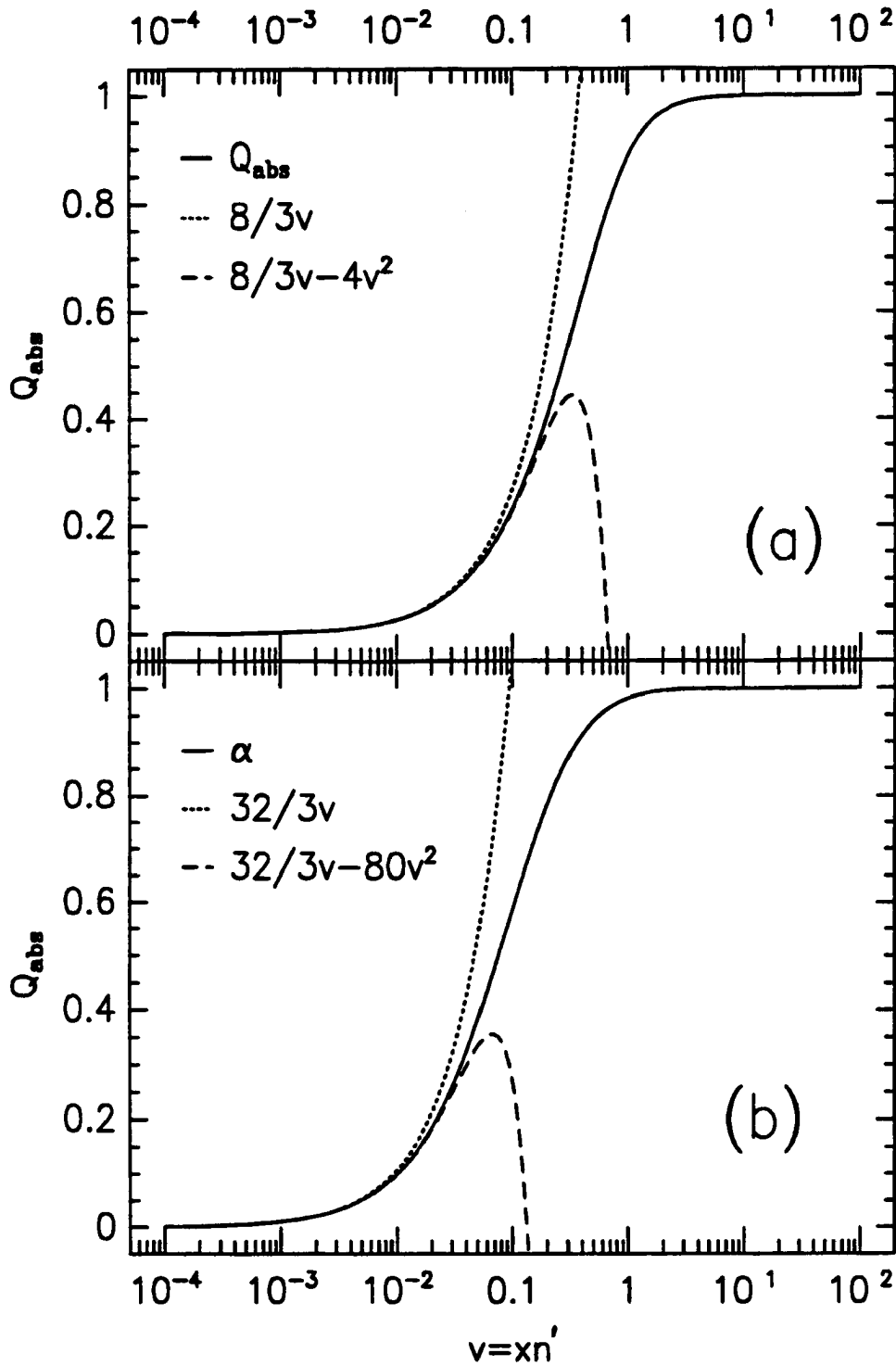
Figure 7.3: (a) Q_{abs} (solid line), linear (dotted line) and quadratic (dashed line) approximations. (b) Same as in (a) but for gamma distribution averaged cases, $\alpha = 2$.

Table 7.1: Values of real(n) and imaginary parts (n') of the refractive index used. The terms b (ADT) and b (BNA) are based on the linear approximation for small xn'. The term b (Chýlek) is based on a least square fit of (Chýlek and Ramaswamy, 1982).

λ	n	n'	b (ADT)	b (BNA)	b (Chýlek)
8.0	1.291	.035	.09	.12	.10
8.2	1.285	.036	.10	.12	.10
8.4	1.279	.037	.10	.12	.10
8.6	1.272	.038	.10	.12	.10
8.8	1.266	.039	.10	.13	.11
9.0	1.259	.040	.11	.13	.11
9.2	1.252	.042	.11	.14	.11
9.4	1.244	.044	.12	.14	.12
9.6	1.235	.046	.12	.15	.12
9.8	1.224	.050	.13	.16	.12
10.0	1.214	.053	.14	.17	.13
10.2	1.202	.059	.16	.19	.13
10.4	1.190	.065	.17	.21	.14
10.6	1.176	.074	.20	.23	.16
10.8	1.166	.086	.23	.27	.17
11.0	1.155	.098	.26	.31	.19
11.2	1.145	.115	.31	.36	.21
11.4	1.138	.134	.36	.41	.23

based on (7.4.3), (7.4.5), and that based on the least square fit to exact calculations (Chýlek and Ramaswamy, 1982). The BNA coefficient b is given by

$$b = \frac{8}{3}n^2(1 - a^3)n' \qquad (7.4.8)$$

and the ADT's b is simply

$$b = \frac{8}{3}n' \qquad (7.4.9)$$

As a check of correctness of (7.4.8) we compare it with Chýlek and Ramaswamy's (1982) work. The term b (ADT) and b (BNA) are based on the linear approximation for small xn'. The term b (Chýlek) is based on a least square fit of to the Mie calculation. The agreement is, in general, good. In this case, the ADT results are in fact closer to Mie calculations than BNA.

7.4.2 Asymptotic expansions for large v

Asymptotic expansion of Q_{abs} for large v follows as

$$Q_{abs} = 1 - \frac{1}{8v^2} \qquad (7.4.10)$$

and for extinction

$$Q_{ext} = 2 - \frac{1}{w^2} \qquad (7.4.11)$$

where Q_{ext} tends to 2 for large w. Although this limiting value of 2 is correct for the extinction efficiency, the approach to the value of 2 should be from above and not from below (Nussenzweig and Wiscombe, 1980). This could be remedied by an empirical correction for the edge effects of the type

$$Q_{ext} = 2 + 1.9923x^{-2/3} \qquad (7.4.12)$$

but it is not done here. In the same approximation an asymptotic expansion for large absolute value of w_n is

$$\beta_{ext} \approx 2A. \qquad (7.4.13)$$

Thus, the total extinction is equal to twice the total cross-section of all the particles.

We are ready now to introduce the corrected ADT. Consider again the small v behavior. In ADT it is

$$Q_{abs} = \frac{8}{3}v \qquad (7.4.14)$$

and BNA gives

$$\hat{Q}_{abs} = \frac{8}{3}n^2(1-a^3)v \qquad (7.4.15)$$

Therefore, we can expect that replacing v by

$$v_{new} = n^2(1-a^3)v \qquad (7.4.16)$$

in the ADT will have correct small v behavior. This is confirmed in Figure 7.2. The solid line is the BNA results which asymptotes to $4n/(n+1)^2$. The original ADT is given as dashed line. It differs from the BNA for most, but very small, v's. The modified ADT introduced here gives excellent agreement with BNA up to $v \approx 1$. In both cases the asymptotic limit for large v is equal 1.

7.5 Results - single scattering approximations

In this section we present comparison of calculations based on the corrected ADT and Mie results. We also exploit the self-similarity predicted by the ADT; namely, that the Mie results should be similar with respect to the parameter v.

7.5.1 Comparison with Mie calculations

Figure 7.4 presents single scattering albedo as a function of wavelength calculated from Mie (solid line) and corrected ADT (dashed line) for two particle sizes (5μm (a) and 50μm) (b). The lower panel (c) shows spectra of both the real and complex part of refractive index for ice.

It is clear from Fig. 7.4 that the single scattering albedo is strongly tied to the complex part of refractive index. Notice that Q_{abs} defined by (7.3.4) depends only on the complex part of refractive index. The expression (7.3.4) predicts (Ackerman and Stephens, 1987) that the single parameter v defines absorption properties of particles under consideration. This simplification suggests an alternative way of presenting results given in Figure 7.4. Instead of wavelength we use v as abscissae. Such scaling predicts that all relationships for particles of different size (x) and composition (n') collapse onto one curve.

The upper panel (a) of Figure 7.5 shows absorption efficiency as a function of v for two particle sizes: 5μm and 50μm. The self-similarity with respect to v holds for $v < 1$, approximately. The lower panel (b) shows wavelength as a function of v. Notice that $v < 0.1$ describes the solar and near-infrared regions. It is clear that the ADT underestimates absorption in both cases. This can be improved but the spread of points given by Mie theory indicates that absorption does not simply scale with one parameter v.

7.5.2 Scaling with respect to v

Figures 7.6 and 7.7 present comparison of Mie calculations with scattering calculations using the ADT. The left column presents Mie calculations plotted against the wavelength. The right column correspond to the same calculations plotted with respect to the ADT
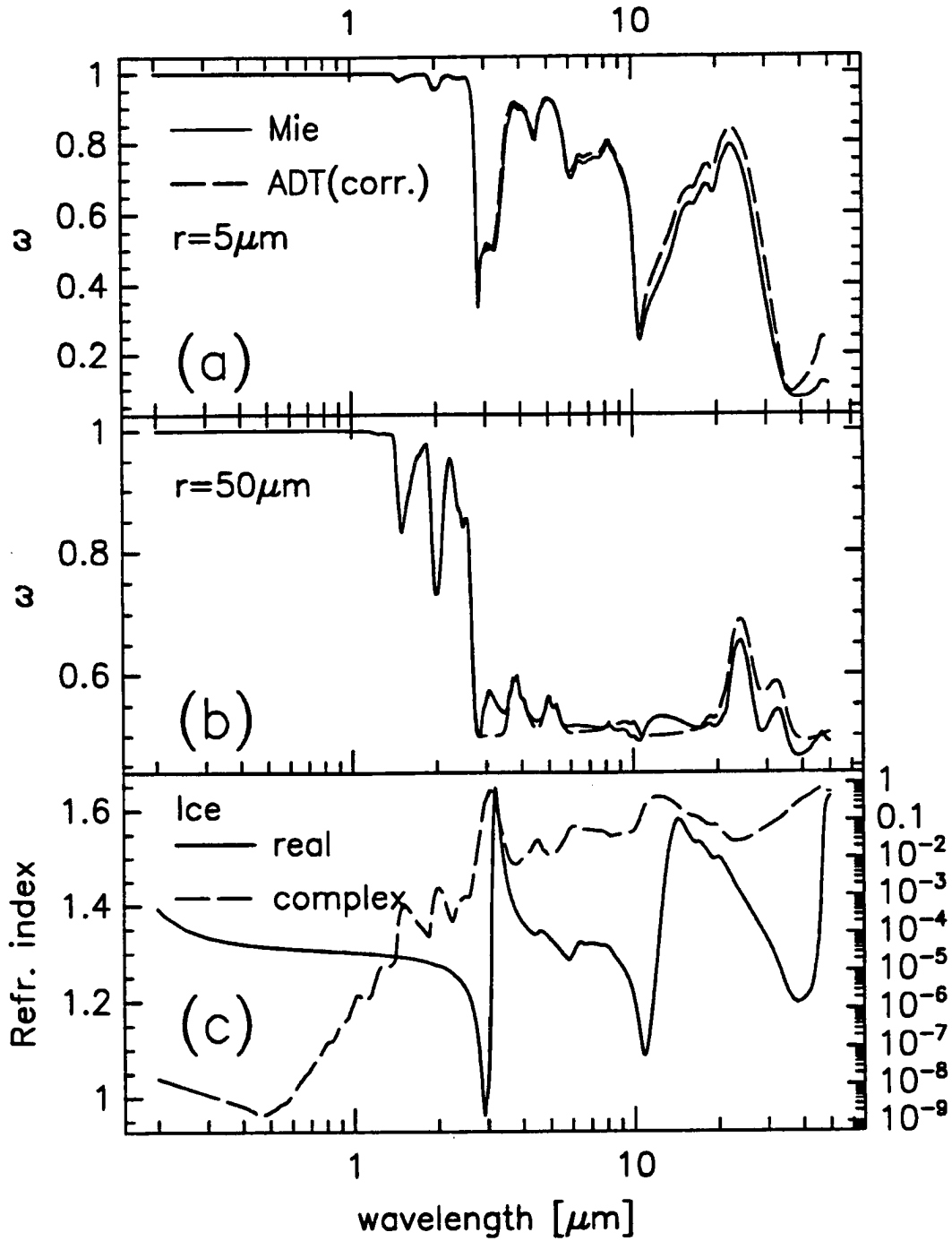
Figure 7.4: (a) Single scattering albedo as a function of wavelength calculated from Mie (solid line) and corrected ADT (dashed line) for the particle of 5μm radius. (b) Same as (a) but for 50μm particle. (c) Refractive index of ice.
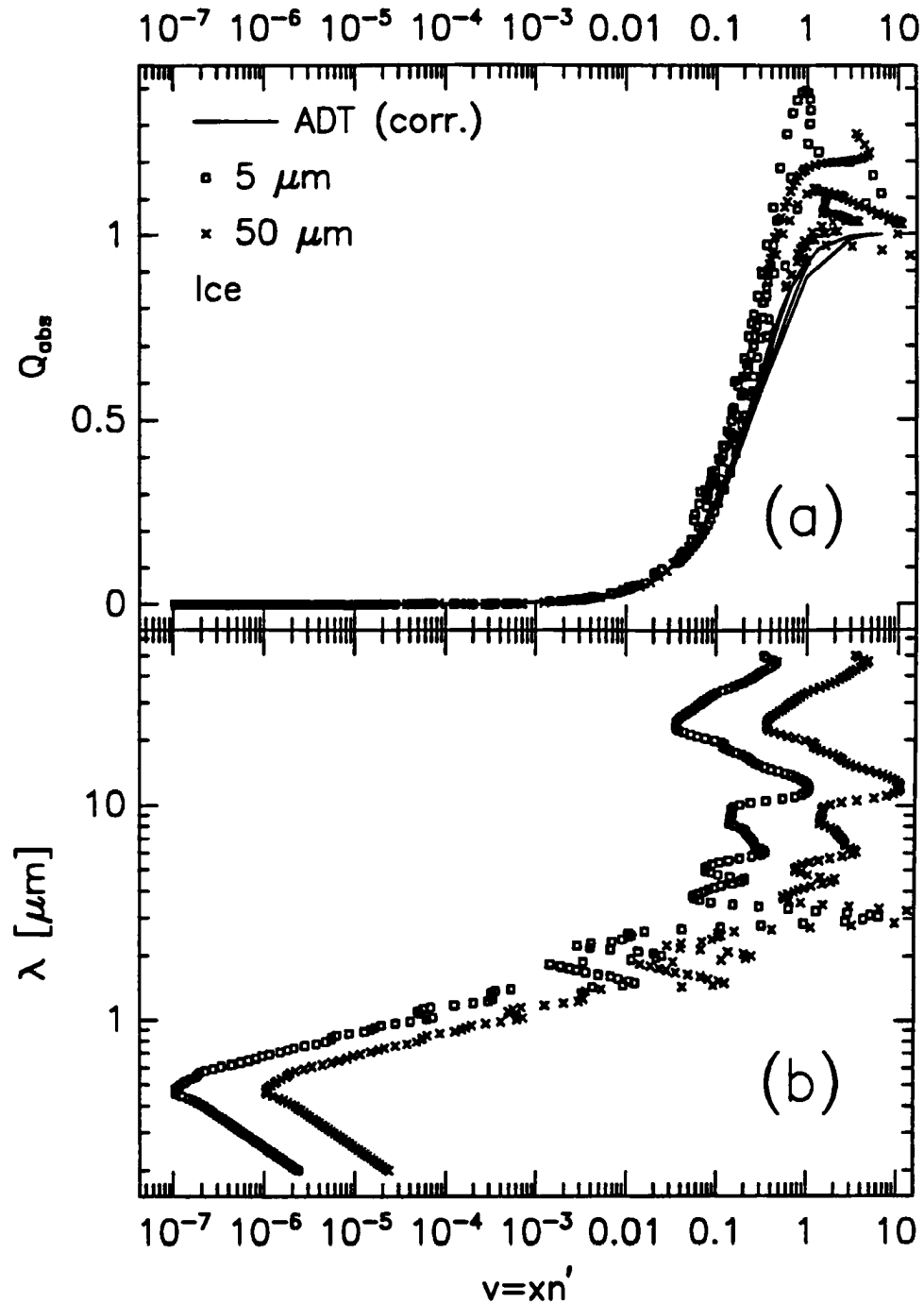
Figure 7.5: (a) Absorption efficiency as a function of v for two particle sizes (squares for 5μm and crosses for 50μm particle). The solid line is for the anomalous diffraction. (b) Wavelength as a function of parameter v for 5μm (squares) and 50μm (crosses)

parameter v. Both carry the same information. From 7.6i and 7.6j one can estimate what wavelength corresponds to v and vice versa. Examining (b), (d), (f), and (h) (right column plots) we see that for small values of v, quantities r_∞ (albedo for optically thick medium), λ (eigenvalue defining two-stream, plane parallel radiative transfer equation), $\gamma Q_{ext}/Q_{abs}$ and Q_{abs} behave very well. The real part of refractive index comes to play for $v > 1$. Examining 7.6j we see that values of $v < 1$ corresponds to the entire solar region except in the centers of the very strong near infrared absorption bands.

The single scattering albedo is presented in Fig. 7.8 as a function of wavelength. The solid lines are Mie calculations for gamma distribution with $\alpha = 2$. The dashed line is the corresponding modified ADT. Squares give values of Mie without averaging for characteristic radius r_n. It can be seen that modified ADT agrees well with the Mie calculations and how smoothing by averaging over the size distribution helps contribute to this excellent agreement.

7.6 Results for irregular particles

The basic idea in this section is to develop, perhaps empirically, the $\mathcal{K}$ function for an irregular particle. It is not immediately clear that this is possible analitically although it can be defined in a least square sense.

We explore this possibility in (Fig. 7.9), by presenting some results for two-spheres in the end-fire configuration. Each panel has three curves corresponding to a 5μm equivalent volume particle (solid line) a 10μm sphere (dotted line) and a 30μm equivalent volume sphere (dashed line) The two-sphere calculations in "end-fire" configuration also shown. The left column figures are plotted as a function of wavelength whereas the right column figures are plotted as a function of v. Panels (a,b) correspond to the two-stream, plane-parallel reflection for infinite medium, (c,d) to Q_{ext}, (e,f) to the single scattering albedo. Panels (g,h) corresponds to Q_{abs}, (i) shows $v = xn'$ as a function of λ and (j) λ as a function of wavelength. Examination of right hand side panels (b), (c), and (d) indicate that the results scale with respect to equivalent radius. Extinction efficiency is more erratic for the two spheres in comparison to single sphere results. It is not dramatically
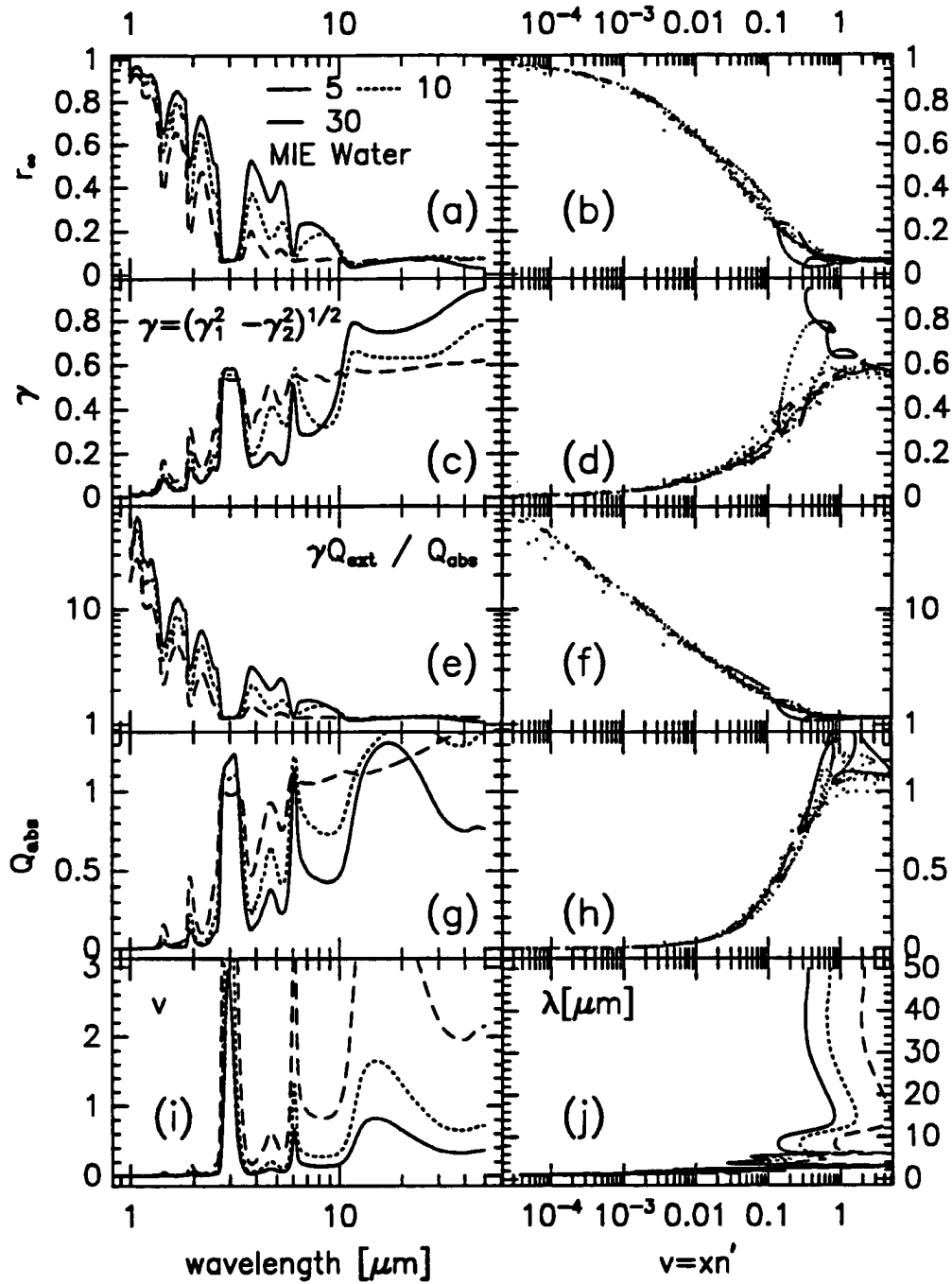
Figure 7.6: Each panel has three curves. Solid line is for 5μm particle. Dotted line is for 10μm dashed line is for 30μm. Mie calculations are presented. Left column figures are plotted as a function of wavelength. Right column figures are plotted as a function of v. (a,b) Two-stream reflection for infinite medium. (c,d) Eigenvalue of two-stream matrix. (e,f) Ratio of $\gamma Q_{ext}/Q_{abs}$. (g,h) Q_{abs}. (i) $v = xn'$. (j) Wavelength.
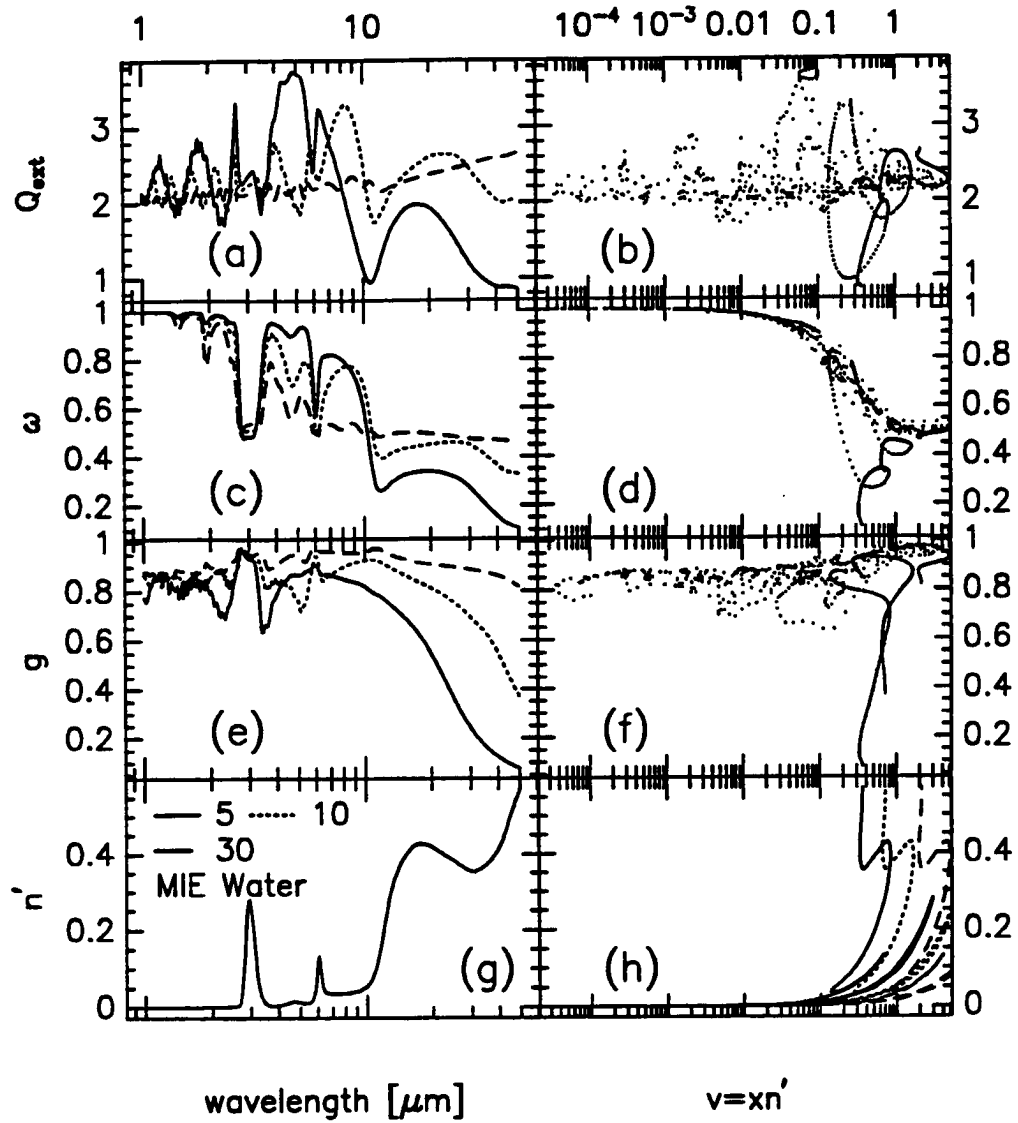
Figure 7.7: Same as in 7.6 but for (a,b) Extinction efficiency. (c,d) Single scattering albedo. (e,f) Asymmetry parameter. (g,h) Complex part of refractive index.
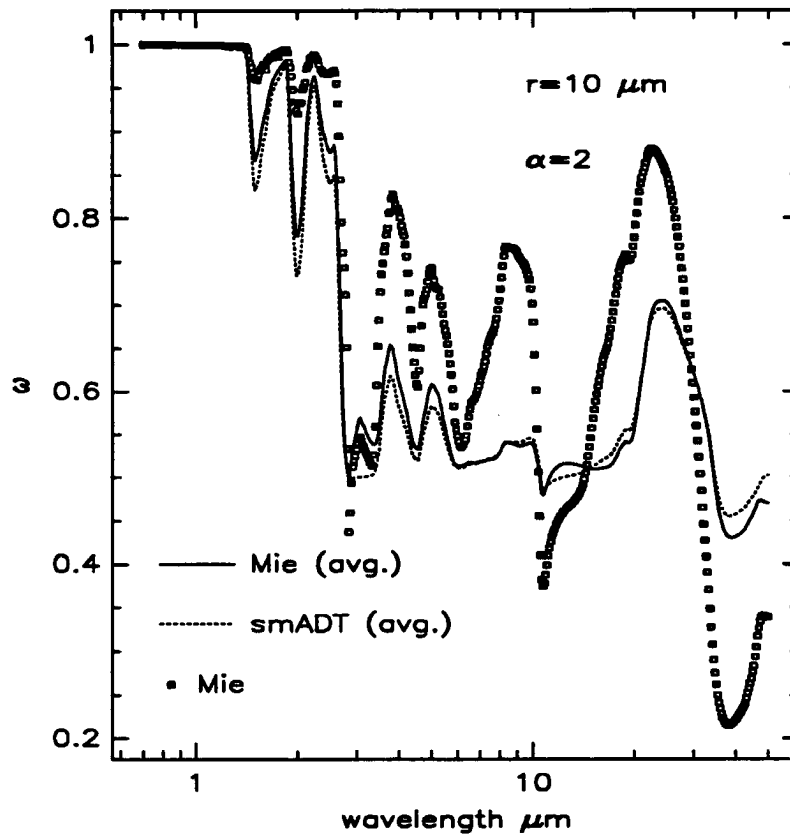
Figure 7.8: Single scattering albedo as a function of wavelength. Solid line are Mie calculations for gamma distribution with $\alpha = 2$. The dashed line is the corresponding modified ADT. Square points give values of Mie without averaging for characteristic radius r_n

pronounced here, but it is expected that for other irregular shapes the $\mathcal{K}_{irr}$ is "shifted" with respect to $\mathcal{K}_{spheres}$. Thus, the effect of non-sphericity is similar to the "shifting" effect of the size distribution in the case of ensemble of spheres. This effect is seen in Fig. 7.10 for reflectivity of one (dots) and two-spheres (dashes). For v in the range from 10^{-3} to 10^{-1} the difference in albedo is about 10%. Both Mie and two-sphere results do not scale well for $v \approx 1$.

This result support the idea that sets of $\mathcal{K}$ functions can be used as a basis for the bulk single scattering radiative parameterization scheme for an ensemble of irregular particles. Knowledge of $\mathcal{K}$ also contains enough information to get the distribution-averaged functions $\mathcal{M}$.
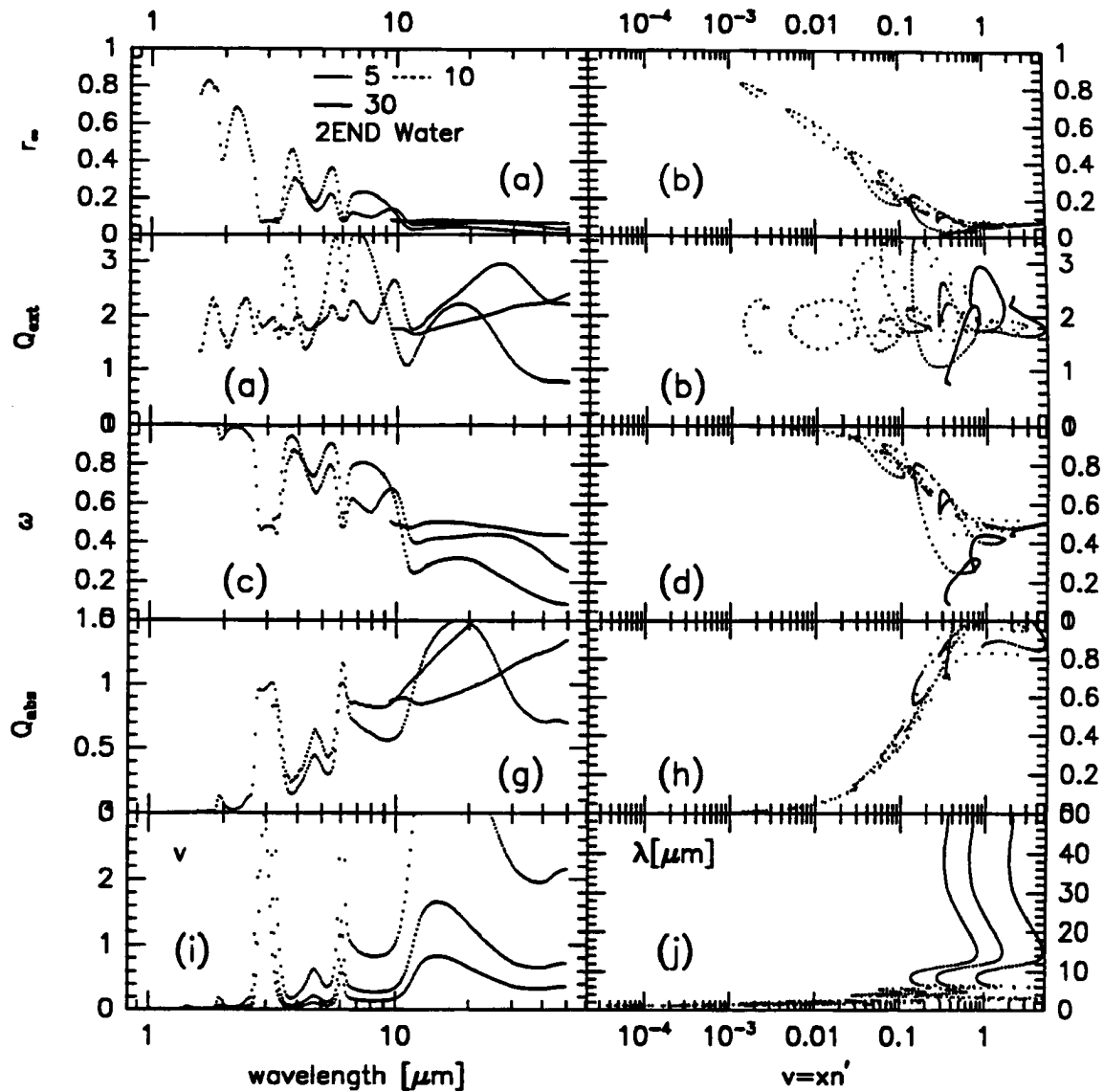
Figure 7.9: Each panel has three curves. Solid line is for 5μm equivalent radius particle. Dotted line is for 10μm dashed line is for 30μm equivalent radius. The two-sphere calculations in "endfire" configuration are presented. Left column figures are plotted as a function of wavelength. Right column figures are plotted as a function of v. (a,b) Two-stream, plane-parallel reflection for infinite medium. (c,d) Q_{ext}. (e,f) Single scattering albedo. (g,h) Q_{abs}. (i) $v = xn'$. (j) Wavelength.
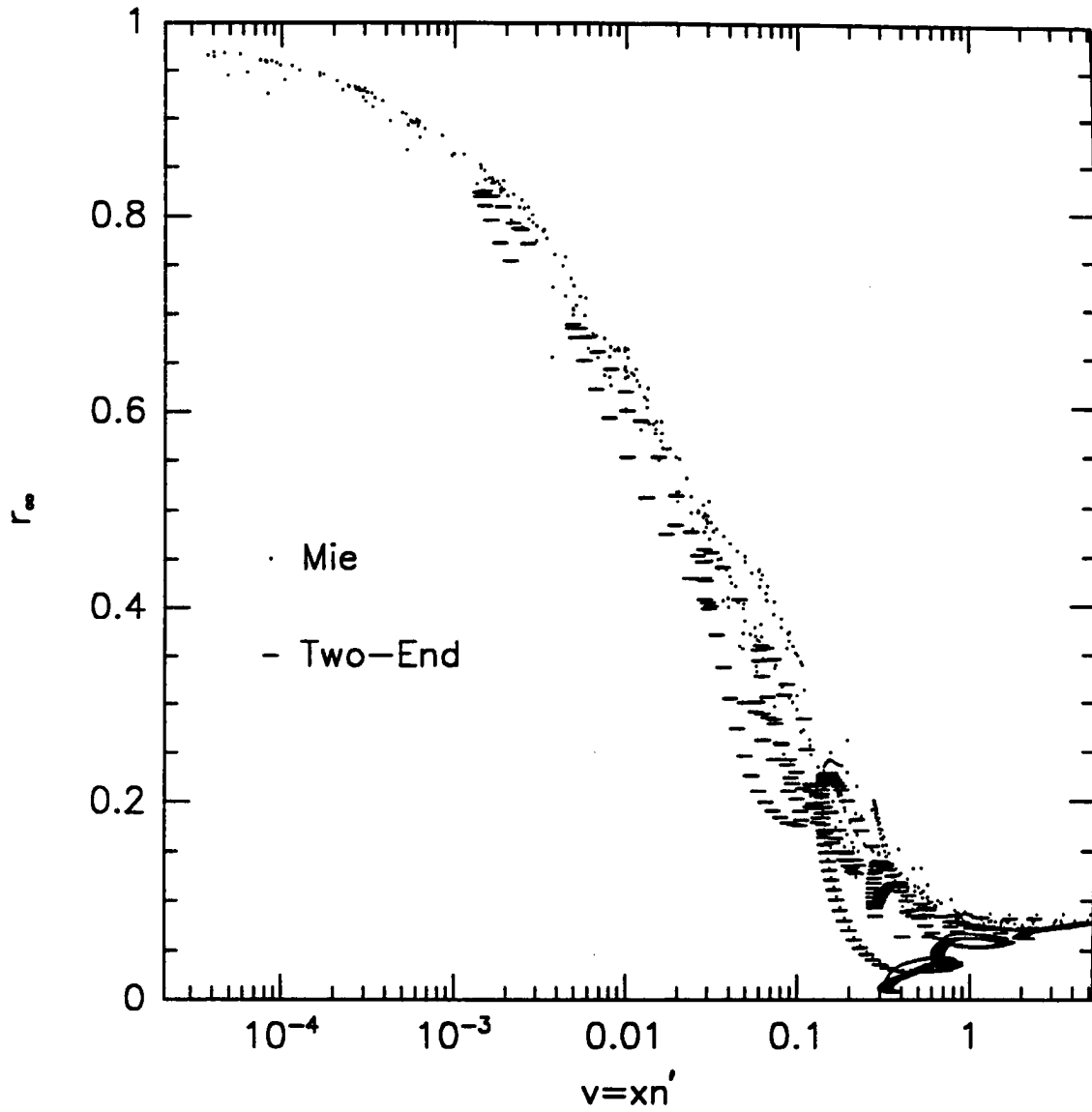
Figure 7.10: Reflectivity of a semi-infinite medium as a function of $v = xn'$ for two-spheres in endfire configuration (dash) and for a single sphere (dot).

Chapter 8

SUMMARY, CONCLUSIONS, AND FURTHER RESEARCH

8.1 Summary

The effects of irregular particles on scattering of radiation are considered using theoretical methods. The major motivation for studying scattering by irregular particles is presented on the basis of results from a simple climate model. These results indicate that uncertainties in our knowledge of the asymmetry parameter and extinction factors significantly affect the response of this model to an imposed climate change.

The Discrete dipole approximation (DDA) is considerably extended in this study and related publications (Draine and Flatau, 1990; Flatau et al., 1990b; Flatau et al., 1990a; Flatau et al., 1991). We show that the matrix equation in the DDA approximation is governed by a symmetric BT matrix and we exploit the properties of such matrices in the solution of the "DDA equation" by using block-Toeplitz or FFT techniques. Particular advantages of the algorithms used in this study are that: (1) the requirements for storage of the DDA matrix on a computer are significantly reduced over the more general case; (2) the full inverse of the DDA matrix can be constructed from just two block columns; (3) CPU time requirements for large N are far less than for direct solvers. These numerical savings are especially relevant to the DDA and to the problem of orientational averaging.

The method is validated against exact results. This validation establishes DDA as a sound and exact method to study scattering by irregular particles. The choice of the polarizability scheme is justified on the basis of the multipole solution for a cluster of two spheres in contact. Results show that the DDA, together with the CG-FFT algorithm, makes possible accurate calculations of scattering and absorption by dielectric targets with

size parameter x as large as $20 - 30$. This last limit is of computational nature and is not related to the stability of the method.

DDA is then applied to study scattering by particle shapes typical of ice crystal clouds. Keeping in mind meteorological applications we limit ourselves to particles typical of upper tropospheric cirrus clouds and we discuss only the "bulk" type characteristics, such as asymmetry parameter and extinction efficiencies. The new results include calculations of the asymmetry parameter for several irregular particles. These results indicate that $g_{irr} > g_{sph}$. We also discuss scattering on inhomogeneous particles ("colored problem"). We show that the efficiencies for ice particles of small size parameters are fairly insensitive to shape and structure but this is progressively less so for increasing size parameters. There is a tendency of colored problems to become "gray" ones with more uniform structure, but the structure can still be seen in efficiencies, particularly for pronounced inhomogeneities (large domains and/or large deviations in refractive index).

In order to validate Anomalous Diffraction Theory for irregular particles we developed a new method to perform such calculations. This method is of use for remote sensing particle methods and will form a basis for simple parameterization schemes. To this author's knowledge, the first comparisons of the ADT for a non-spherical particle with an exact solution are reported here. The results show that DDA and ADT results are not in agreement for the face-in light incidence close to the values of size parameter where constructive and destructive interference is taking place. However, the results compare well for other orientations studied. The absorption efficiency is under-predicted but the qualitative behavior is in agreement and suggests a simple relation to the volume of the particle. This fact makes it possible to introduce semi-empirical corrections to absorption efficiencies.

Parameterization of scattering properties of irregular particles is considered on the basis of the anomalous diffraction theory. We develop the ADT for particles distributed in size. A key result is that the similarity scaling predicted by the ADT for spheres is also shown to apply for nonspherical particles. The results represent a complete parameterization of the three main optical properties: the volume extinction β_{ext}, the single

scattering albedo ω, and the particle asymmetry parameter g, as a function of refractive index, characteristic radius of the distribution and the distribution width.

8.2 Conclusions

We went considerable way towards our stated goal of advancing the knowledge about the effects of irregular particles on scattering radiation. It is possible now to apply the DDA and get answers about processes which depend on details of particle structure. These include applications in high resolution spectroscopy, optical particle sizing, local albedo returns (radar), line-by-line radiative transfer calculations, angular dependence of lidar backscatter, halo, and directional cloud albedo. A framework was built for the parameterization of effects of irregular particles and presented evidence that such a parameterization is possible. This development is related to the second object of this research, namely understanding and simplifying the "bulk" scattering processes.

These scattering problems are difficult and much remains to be done, extended, or discovered. Faster machines, better methods, will let us perform calculations in the higher size parameter range.

8.3 Suggestions for future research

8.3.1 Discrete Multipole Approximation (DMA)

It is possible to specialize the multi-sphere method (Bruning and Lo, 1969; Borghese et al., 1979; Fuller, 1991; Mackowski, 1991; Hamid et al., 1990) to the Rayleigh approximation. Figure 8.1 shows a discrete multipole solution of scattering by a sphere with refractive index $m = 1.7 + 0.1i$ as a function of size parameter x. Exact results from Mie solutions (solid line) are compared with results computed using the DMA in the Rayleigh approximation (cross) and DDA (square). The magnetic dipole moment in the DMA method was included. A sphere with the equivalent size parameter x is composed of $N = 136$ small "lattice" spheres. The results show that DMA can be reduced to the discrete dipole approximation. A combined multipole/dipole method (DM/DD) can be developed: Figure 8.2 shows a cross-section of a cube built of a centrally positioned sphere

m=1.7+0.1i, line—Mie, cross—DM(mag), square—DD(Drai88)

Figure 8.1: Discrete multipole solution of scattering by a sphere with refractive index $m = 1.7 + 0.1i$ as a function of size parameter x. Exact results from the Mie solution (solid line) are compared with results computed using the DMA (cross) and DDA (square) for $N = 136$ dipoles or pseudo-spheres.

and complemented by spherical dipoles. The central sphere is visible as a cavity in Fig. 8.2 and its electromagnetic response include higher order multipoles. Discrete multipole re-

Multipole pseudocube

$(\theta=0 \quad \varphi=0 \quad \beta=0)$
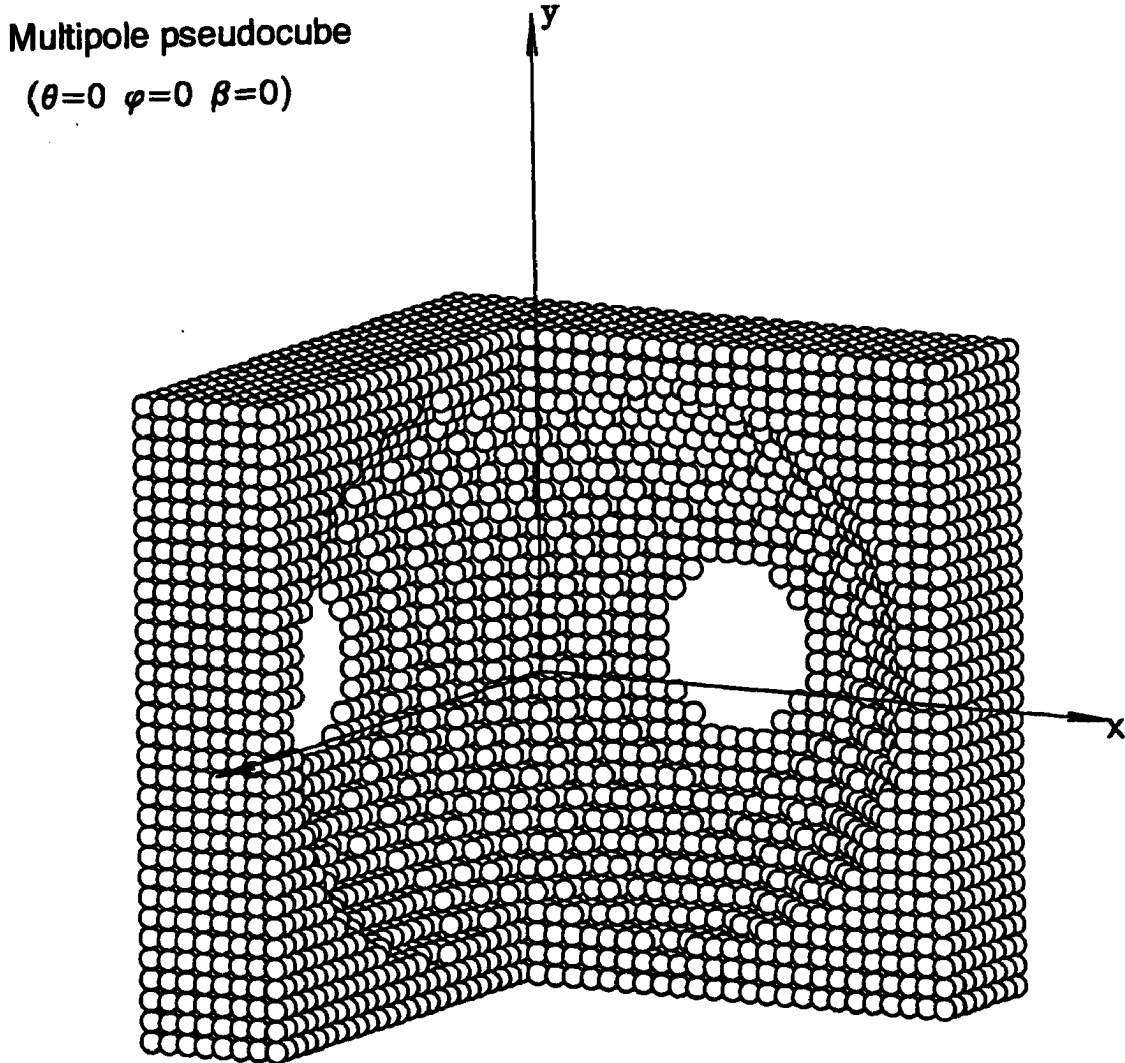
Figure 8.2: Cross-section of a cube shows a spherical cavity inside.

sults of scattering by a cube with refractive index $m = 1.7 + 0.1i$ as a function of size parameter x are shown in Fig. 8.3. Exact DDA results (solid line) are obtained by placing dipoles on a high resolution lattice ($27 \times 27 \times 27$). Crosses show the approximate result for the combined multipole/dipole method. There are $N = 80$ "corner" dipoles in this scheme and one multipole sphere in the center. Results for a cube composed of dipoles only are plotted as squares. There are $N = 216$ dipoles in this case. Mie solution results are also included (dashed line).

Further work should include validation of the method, development of more robust numerics, and extension to elongated shapes. A combined multipole/dipole method leads to a drastic decrease in the number of dipoles needed to represent the shape but may break the translational invariance. Deeper understanding of spatial invariance in multipole representation is needed. There is also a need for extension of DDA to non-cubical lattices which would allow calculations for objects with larger aspect ratios. Quasi-two dimensional problems like scattering by long hexagonal prisms may be attacked with the DDA and/or DM/DD approach with long cylinders as unit lattice dipoles (Taubenblatt, 1990). This is essentially a two-dimensional problem and is apparently simple to handle numerically. It remains a challenge to reproduce a halo from the numerical solution to Maxwell equations.

8.3.2 Orientational averaging

Orientational averages are related to the inverse of the DDA matrix **A**. The shape information is contained there and is decoupled from the incident electric wave. ADT and Rayleigh-Gans-Debye approximation can be formulated in terms of a similar linear system of equations. It is therefore natural to expect that the inverse of $\mathbf{A}^{-1}$ or its invariants (e.g. trace) should play an important role in the theory being developed here (Flatau et al., 1990a; Keller and Bustamante, 1986). For targets described by a small number of dipoles, finding $\mathbf{A}^{-1}$ can be done by direct inversion. For interesting problems with large size parameters, the order of **A** can approach 10^5. For such cases direct inversion is not possible which is why $\mathbf{A}^{-1}$ is not yet sufficiently studied. Two ideas can be pursued here: resolvent kernel (Kattawar et al., 1987) and spectral representation. To fix notation consider a Fredholm integral equation of the second kind (Pipkin, 1991)

$$u(x) = f(x) + \int_a^b K(x,y)u(y)dy \qquad (8.3.1)$$

This is our prototype equation corresponding to DDA integral formulation. Here $f(x)$, $u(x)$, and $K(x,y)$ correspond to the incident electric field, searched electric field, and dyadic Green's function, respectively. After discretization we have
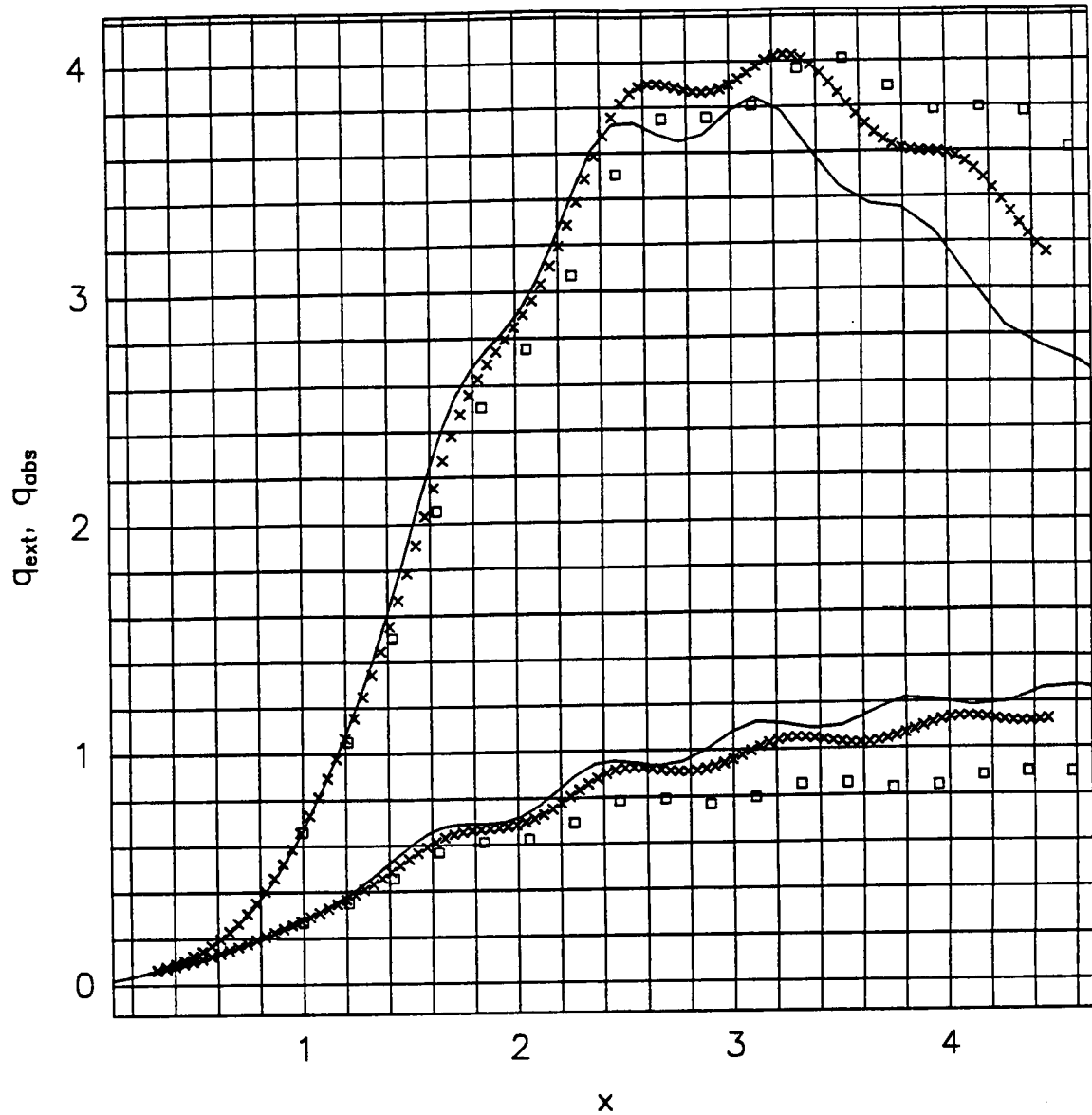
$$\mathbf{u} = \mathbf{f} + \mathbf{Ku} \qquad (8.3.2)$$
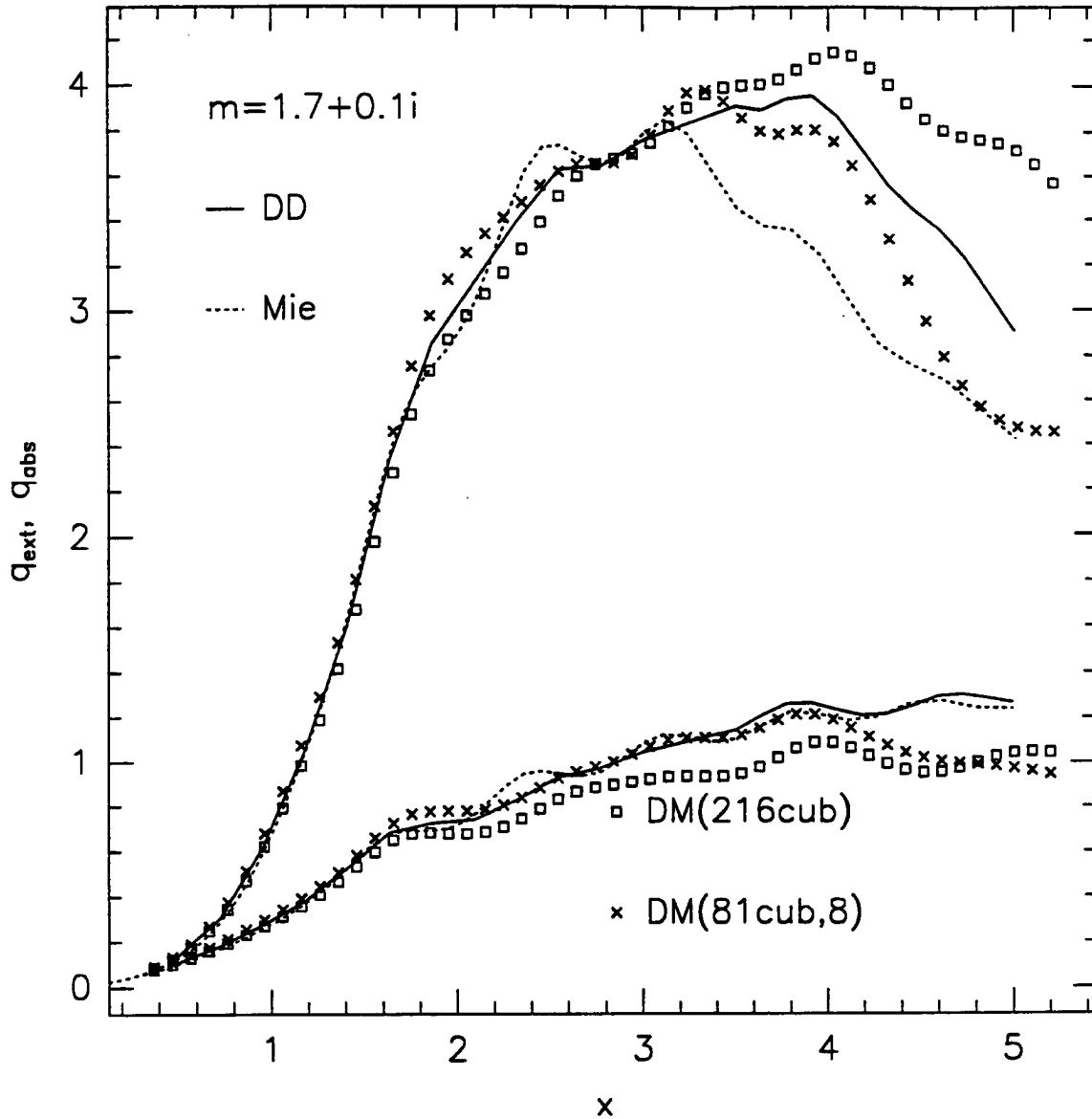
Figure 8.3: Discrete multipole solution of scattering by a cube with refractive index $m = 1.7 + 0.1i$ as a function of size parameter x. Exact DDA results (solid line) are obtained on high resolution lattice ($27 \times 27 \times 27$). Crosses show approximate result for cube computed using the combined multipole/dipole method. There are $N = 80$ "corner" dipoles in this scheme and one sphere in the center. Results for cube build by dipoles are plotted as squares. There is $N = 216$ dipoles in this case. For comparison Mie calculations are also included (dashed line).

where u, f are vectors, and K matrix. A vector φ_i is a right eigenvector of the matrix K if

$$K\varphi_i = k_i\varphi_i \tag{8.3.3}$$

k_i is called the eigenvalue. A left eigenvector of K is

$$\psi_i K = k_i \psi_i \tag{8.3.4}$$

If we use the eigenvectors φ_i as base vectors, we can write any vector f in the form

$$f = \sum f_i \varphi \tag{8.3.5}$$

Because of the orthogonality of left and right eigenvectors, the coefficients f_i, the components of f with respect to the basis φ_i, are the inner products of f with the left eigenvectors

$$f = \sum \varphi_i (\psi_i, f) \tag{8.3.6}$$

It can be shown that

$$K = \sum k_i \varphi_i \psi_i \tag{8.3.7}$$

This is the spectral representation of K. Also

$$K^n = \sum k_i^n \varphi_i \psi_i \tag{8.3.8}$$

and, in particular, the inverse is

$$K^{-1} = \sum k_i^{-1} \varphi_i \psi_i \tag{8.3.9}$$

The linear system of equations (8.3.2) can be written as

$$u = f + Rf \tag{8.3.10}$$

where the resolvent matrix R is defined by eigenpairs

$$R = \sum \frac{k_i}{1 - k_i} \varphi_i \psi_i \tag{8.3.11}$$

The idea of resolvent kernel has been pursued in the context of the DDA by Kattawar *et al.* (1987) who solved the matrix differential equation to get the resolvent. Unfortunately, the

need for an explicit representation of **R** reduced the utility of this interesting approach. On the other hand eigenpairs of the DDA matrix can be obtained from the conjugate gradient iterations (Golub and van Loan, 1983). If only a few eigenpairs are needed to describe the resolvent it may lead to a concise representation of an inverse of **A**.

In addition, the eigenvalue analysis may provide classification of scattering by irregular particles. The shape information is contained in the normal modes of **A**. Following the eigenvalues when perturbing the shape or size (Bhatia, 1987) we may better understand the scattering response. It may turn out that the parameterization of scattering by irregular particles will be based on spectral representation. Morphology dependent resonances for spheres (Fuller, 1991) are connected to the eigenvalue analysis, and such studies can be extended to non-spherical particles. Scattering on irregular objects and random averaging of scattering properties are related to certain developments in statistical mechanics, namely studies of dielectric constant in hard sphere fluids (Cichocki and Felderhof, 1989; Kirkwood, 1936). There is also a relation to the electronic band theories (Butler and Nesbet, 1990). All of this is largely uncharted territory.

8.3.3 Experiment and theory

There are some experimental results related to irregular particle scattering (Zerull and Giese, 1974; Zerull, 1976; Zerull et al., 1977b; Napper and Ottewill, 1963; Perry et al., 1978; Schureman et al., 1981; Wang and Gustafson, 1984). Wiscombe and Mugnai (1983), Bohren and Huffman (1983) and Pollack and Cuzzi (1980) provide additional references on this topic. At the moment the theory seems to be ahead of the laboratory experiments. Experimental studies could be stimulated by providing a set of well defined theoretical results on scattering. Such results should include full S_{ij} matrix, and derived quantities such as backscatter, asymmetry parameter, and depolarization for targets with clear non-spherical signatures. We provide an example of a calculation we advocate in Fig. 8.4 for the rosette shape (Fig. 8.5). Phase function and depolarization ratio are presented there. The depolarizatiom ratio is an important quantity observed by polarization lidars. Values other than unity indicate non-spherical shape.

Combination of bullets (rosette)

(θ=90 φ=0 β=0)
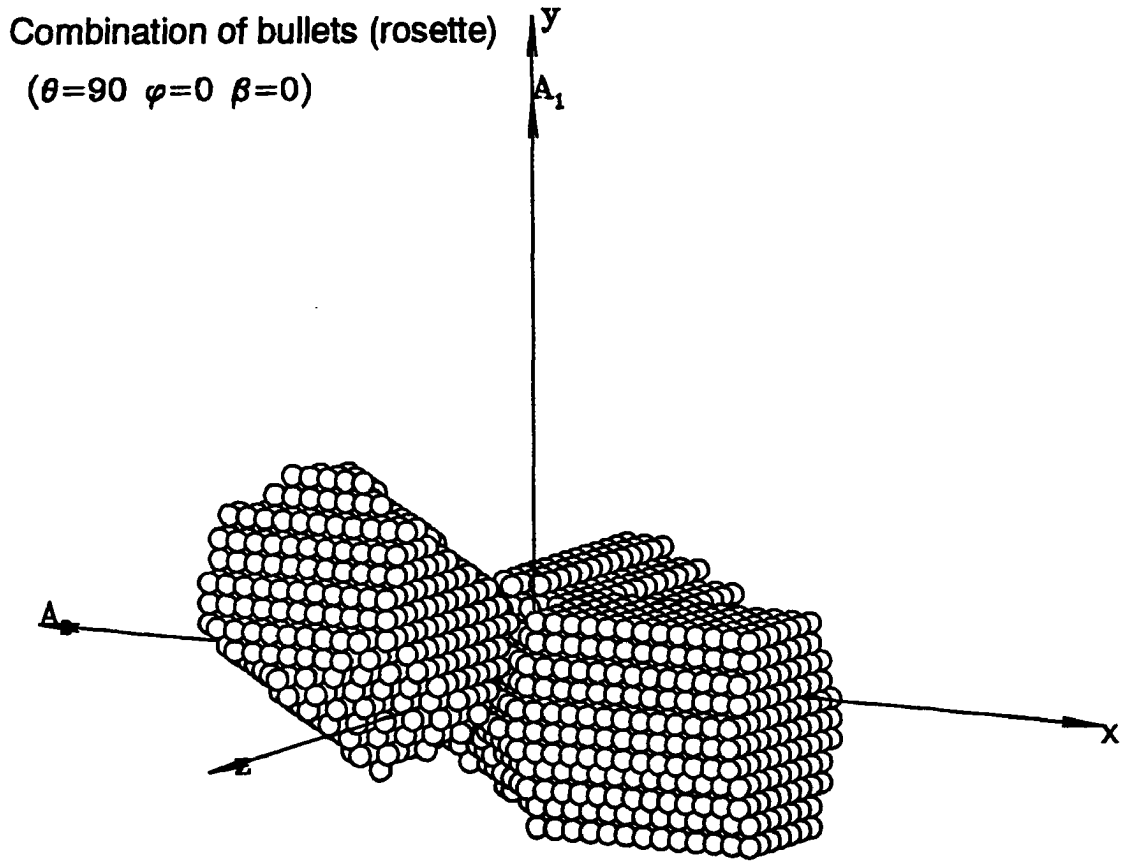
Figure 8.4: Mueller matrix elements S_{11} (phase function) and depolarization ratio S_{22}/S_{11} as a function of scattering angle for combination of bullets (see 8.5).

On the other hand, experimental results on scattering by simple shapes in particular orientation and for sequences of size parameters are needed for the validation purposes. The sequences (refractive index, size parameter, orientation) are important for comparisons.

Experiments can help theory. Comprehensive laboratory measurements of scattering by ensembles of particles in random orientation (Dugin et al., 1977; Volkovitskiy et al., 1975; Volkovitskiy et al., 1980) would be of value to stimulate theoretical progress. This is related to parameterization issues. It is not clear what would constitute a "good" set of parameters defining the bulk radiative response of irregular particles, and such parameters could be defined by experimentalist.

8.3.4 Miscellaneous

Here is a list of possible extensions of this work:

1. Development of basic classification of side scatter, backscatter, depolarization in terms of departure from sphericity.

2. Further comparisons of approximate (e.g. ADT) and semi-exact (DDA) theories for different shapes and orientations. Extension of analysis to larger size parameters. Study of random-averaged results in both approximations. Phase function comparisons between both methods.

3. Use DD and/or DM approximations to study effective medium theories, role of porosity, and role of refractive index inhomogeneities.
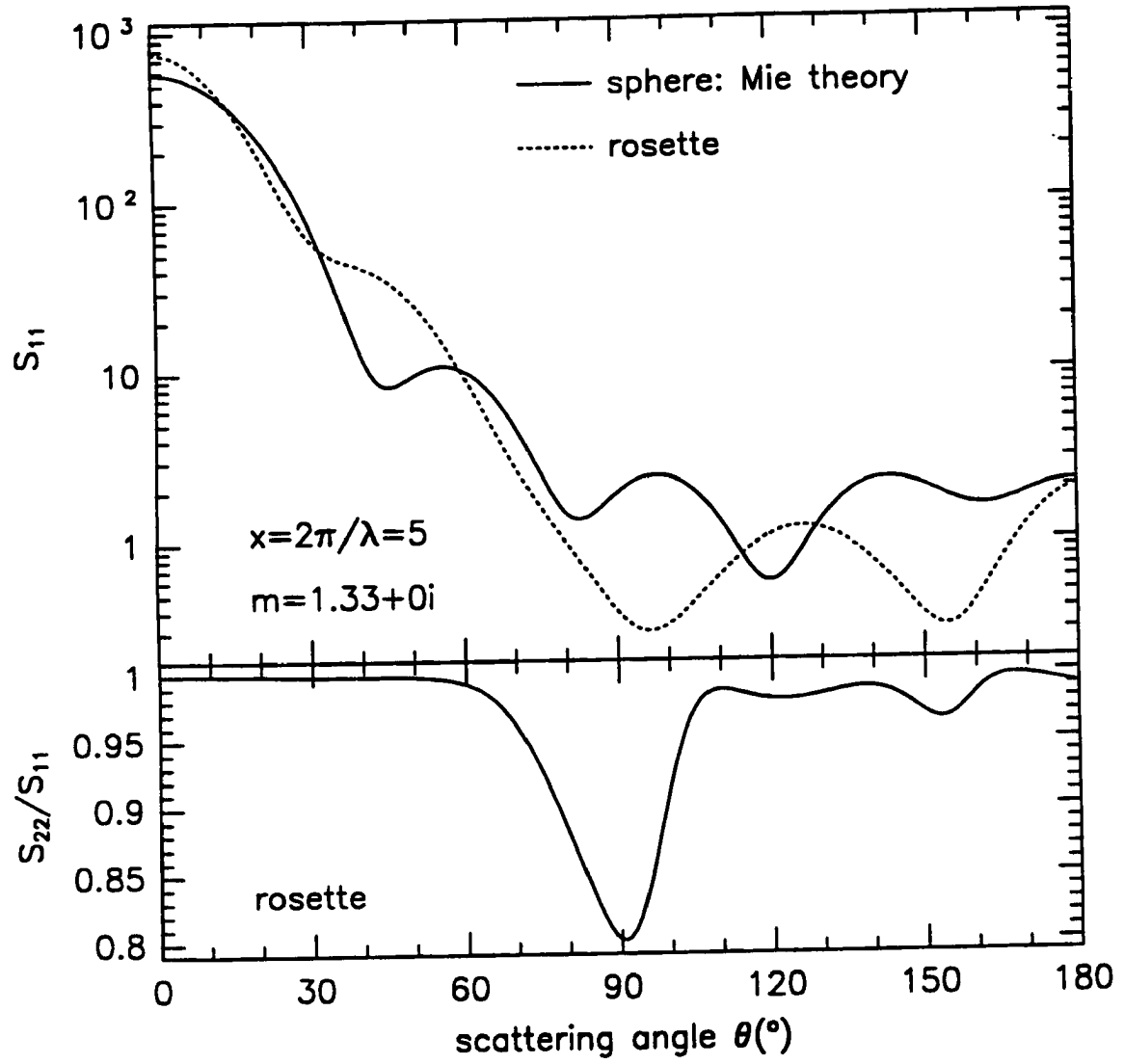
Figure 8.5: Combination of three bullets.

Bibliography

Ackerman, S. A. and G. L. Stephens, 1987: The absorption of solar radiation by cloud droplets: an application of anomalous diffraction theory. *J. Atmos. Sci*, 44, 1574—1588.

Arushanian, O. B., M. K. Samarin, V. V. Voevodin, B. S. Garbow, M. Boyle, W. R. Cowell, and K. W. Dritz, 1983: The Toeplitz package users' guide. Technical Report ANL-83-16, Argonne National Laboratory, Argonne, Il 60439.

Asano, S. and M. Sato, 1980: Light scattering by randomly oriented spheroidal particles. *Appl. Opt.*, 19, 679—691.

Bhatia, R., 1987: *Perturbation bounds for matrix eigenvalues*. Pitman research notes in mathematics. Longman Scientific and Technical Press, 162.

Bird, R. B., R. C. Armstrong, and O. Hassager, 1977: *Dynamics of polymeric liquids, Vol. 1 Fluid mechanics*. Wiley, New York. (Appendix A).

Bohren, C. F. and D. R. Huffman, 1983: *Absorption and scattering of light by small particles*. J. Wiley and Sons, New York.

Bohren, C. F. and T. J. Nevitt, 1983: Absorption by a sphere: a simple approximation. *Appl. Opt.*, 22, 774—775.

Bohren, C. F. and S. B. Singham, 1991: Backscattering by nonspherical particles: A review of methods and suggested new approaches. *J. Geophys. Res.*, 96, 5269—5277.

Borghese, F., P. Denti, G. Toscano, and O. Sindoni, 1979: Electromagnetic scattering by a cluster of spheres. *Appl. Opt.*, 18, 116—120.

Bourrely, C., P. Chiappetta, and B. Torresani, 1986: Light scattering by particles of arbitrary shape: a fractal approach. *J. Opt. Soc. Am. A*, **3**, 250—255.

Bruning, J. H. and Y. T. Lo, 1969: Multiple scattering by spheres. Technical Report 69-5, Antenna Laboratory, Department of Electrical Engineering, Enginnering Experiment Station, University of Illinois, Urbana, Illinois, 169.

Bryant, F. D. and P. Latimer, 1969: Optical efficiencies of large particles of arbitrary shape and orientation. *J. Coll. Inter. Sci.*, **30**, 291—304.

Bunch, J. R., 1985: Stability of methods for solving Toeplitz systems of equations. *SIAM J. Sci. Stat. Comput.*, **6**, 349—364.

Butler, W. H. and R. K. Nesbet, 1990: Validity, accuracy, and efficiency of multiple-scattering theory for space-filling scatterers. *Phys. Rev. B*, **42**, 1518—1525.

Chen, T. W., 1987: Scattering of light by a stratified sphere in high energy approximation. *Appl. Opt.*, **26**, 4155—4158.

Chen, T. W., 1988: Eikonal approximation method for small-angle light scattering. *J. Mod. Opt.*, **35**, 743—752.

Chen, T. W., 1989: High energy light scattering in the generalized eikonal approximation. *Appl. Opt.*, **28**, 4096—4102.

Chen, T. W., 1990: Sum rule for multiple scattering of light by neighboring spheres. *J. Appl. Phys.*, **67**, 7147—7148.

Chen, T. W. and D. W. Hook, 1976: Backward potential scattering at high energy. *Phys. Rev. D*, **12**, 1765—1771.

Chiappetta, P. and B. Torresani, 1988: Electromagnetic scattering from a dielectric helix. *Appl. Opt.*, **27**, 4856—4860.

Chýlek, P. and J. D. Klett, 1991: Absorption and scattering of electromagnetic radiation by prismatic columns: anomalous diffraction approximation. *J. Opt. Soc. Am. A*, **8**, 1713—1720.

Chýlek, P. and V. Ramaswamy, 1982: Simple approximation for infrared emissivity of water clouds. *J. Atmos. Sci.*, **39**, 171—177.

Cichocki, B. and B. U. Felderhof, 1989: Electrostatic spectrum and dielectric constant of nonpolar hard sphere fluids. *J. Chem. Phys.*, **90**, 4960—4967.

Cohen, A. and P. Alpert, 1980: Radiation pressure on randomly oriented infinite cylinders. *Appl. Opt.*, **19**, 558—560.

Cox, S. K., 1971: Cirrus clouds and climate. *J. Atmos. Sci.*, **28**, 1513—1515.

Cross, D. A. and P. Latimer, 1970: General solutions for the extinction and absorption efficiencies of arbitrary oriented cylinders by anomalous-diffraction methods. *J. Opt. Soc. Am.*, **60**, 904—907.

Davis, M. H., 1967: The forces on two spheres in Stokes flow. Memorandum RM-5357-PR, The RAND Corporations, 1700 Main St., Santa Monica, Calif., 18.

Debi, S. and S. K. Sharma, 1979: Investigation of domains of validity of approximation methods in light scattering from spherical obstacles. *Optica Acta*, **26**, 297—300.

Dongarra, J. J., J. R. Bunch, C. B. Moler, and G. W. Stewart, 1978: *LINPACK users guide.* SIAM Publications, Philadelphia.

Dongarra, J. J. and E. Grosse, 1987: Distribution of mathematical software via electronic mail. *Comm. ACM*, **30**, 403—407.

Draine, B. T., 1988: The discrete-dipole approximation and its application to interstellar graphite grains. *Astrophys. J.*, **333**, 848—872.

Draine, B. T. and P. J. Flatau, 1990: DDSCAT. *J. Quant. Spectrosc. Radiat. Transfer*, **44**, I. Software package JQSRT-020-S90.

Draine, B. T. and J. J. Goodman, 1992: Wave propagation on a polarizable point lattice and the discrete dipole approximation. submitted to The Astrophysical Journal.

Dugin, V. P., O. A. Volkovitskiy, S. O. Mirumyants, and N. K. Nikiforova, 1977: Anisotropy of light scattering by artificial crystalline cloud formation. *Izv., Atmos. Oceanic Phys.*, **13**, 22—25.

Eddy, W. F., 1977: A new convex hull algorithm for planar sets. *ACM Transactions on Mathematical Software*, **3**, 398—403.

Farone, W. A. and M. J. I. Robinson, 1968: The range of validity of the anomalous diffraction approximation to electromagnetic scattering by a sphere. *Appl. Opt.*, **7**, 643—645.

Flatau, P. J., B. T. Draine, and G. L. Stephens, 1991: Scattering of light by cirrus ice crystals — application of the Discrete Dipole Scattering Code DDSCAT. Symposium on Aerosol-Cloud-Climate Interactions, XX General Assembly IUGG.

Flatau, P. J., G. L. Stephens, and B. T. Draine, 1988: Scattering on hexagonal ice crystals: discrete dipole and anomalous diffraction approximations. In *International radiation symposium*, Lenoble, J. and Geleyn, J.-F., editors, A. Deepak Publishing, Hampton, Viginia, USA, 72—75. Lille, France.

Flatau, P. J., G. L. Stephens, and B. T. Draine, 1990a: Light scattering by rectangular solids in the discrete-dipole approximation: a new algorithm exploiting the block-Toeplitz structure. *J. Opt. Soc. Am.*, **7**, 593–600.

Flatau, P. J., G. L. Stephens, and B. T. Draine, 1990b: Radiative properties of visible and subvisible cirrus: scattering on hexagonal ice crystals. In *FIRE science results 1988*, McDougal, D. S. and Wagner, H. S., editors, NASA Langley Research Center, NASA, Hampton, Virginia, 75–80. Proceedings of a conference held in Vail, Colo. July 11-15, 1988. NASA CP3083.

Flatau, P. J., G. J. Tripoli, J. Verlinde, and W. R. Cotton, 1989: The CSU-RAMS cloud microphysics module: General theory and code documentation. Technical Report 451, Colorado State University, Fort Collins, Colorado 80523.

Friedlander, B., M. Morf, T. Kailath, and L. Ljung, 1979: New inversion formulas for matrices classified in terms of their distance from Toeplitz matrices. *Lin. Alg. Appl.*, **27**, 31—60.

Fuller, K. A., 1991: Optical resonances and two-sphere systems. *Appl. Opt.*, **30**, 4716—4731.

Fuller, K. A. and G. W. Kattawar, 1988: Consummate solution to the problem of classical electromagnetic scattering by an ensemble of spheres. I. Linear chains. *Opt. Lett.*, **13**, 90—92.

Goedecke, G. H. and S. G. O'Brien, 1988: Scattering by irregular inhomogeneous particles via the digitized Green's function algorithm. *Appl. Opt.*, **27**, 2431—2438.

Gohberg, I. C. and G. Heinig, 1974: inversion of finite Toeplitz matrices with entries being elements from a noncommutative algebra. *Rev. Roumaine Math. Pures Appl.*, **19**, 623—665. (in Russian).

Golub, G. H. and C. F. van Loan, 1983: *Matrix computations*, volume 3 of *John Hopkins series in the mathematical sciences*. Johns Hopkins University Press, Baltimore, 476, 1 edition.

Goodman, J. J., B. T. Draine, and P. J. Flatau, 1991: Application of fast-Fourier-transform techniques to the discrete-dipole approximation. *Optics Letters*, **16**, 1198—1200.

Hage, J. I. and J. M. Greenberg, 1990: A model for the optical properties of porous grains. *Astrophys. J.*, **361**, 251.

Haines, E., 1991: Fast ray-convex polyhedron intersection. In *Graphics Gems II*, Avro, J., editor. Academic Press, Boston, 643.

Hallet, J., 1987: Faceted snow crystals. *J. Opt. Soc. Am (A)*, **4**, 581—588.

Hallet, J. and R. E. J. Lewis, 1967: Mother of pearl clouds. *Weather*, **22**, 56—65.

Hamid, A.-K., I. R. Ciric, and M. Hamid, 1990: Electromagnetic scattering by an arbitary configuration of dielectric spheres. *Can. J. Phys.*, **68**, 1419—1428.

Hansen, J. E. and L. D. Travis, 1974: Light scattering in planetary atmospheres. *Space science reviews*, **16**, 527—610.

Harimaya, T., 1976: The embryo and formation of graupel. *J. Meteor. Soc. Japan*, **54**, 42—51.

Hocking, L. M., 1959: The collision efficiency of small drops. *Quart. J. Roy. Met. Soc.*, **85**, 44-50.

Irvine, W. M., 1965: Light scattering by spherical particles: Radiation pressure, asymmetry factor, and extinction cross section. *J. Opt. Soc. Am.*, **55**, 16—21.

Iskander, M. F., H. Y. Chen, and J. E. Penner, 1989: Optical scattering and absorption by branched chains of aerosols. *Appl. Opt.*, **28**, 3083—3091.

Jackson, J. D., 1975: *Classical electrodynamics.* Wiley, New York, 2nd edition.

Kajikawa, M., 1973: Laboratory measurements of falling velocity of individual ice crystals. *J. Meteor. Soc. Japan*, **51**, 263—272.

Kajikawa, M., K. Kikuchi, and C. Magono, 1980: Frequency of occurence of peculiar shapes of snow crystals. *J. Met. Soc. Jap.*, **58**, 416—421.

Kattawar, G. W., C.-R. Hu, M. E. Parkin, and P. Herb, 1987: Muller matrix calculations for dielectric cubes: comparison with experiments. *Appl. Opt.*, **26**, 4174—4180.

Keller, D. and C. Bustamante, 1986: Theory of the interaction of light with large inhomogeneous molecular aggregates. I. Absorption. *J. Chem. Phys.*, **84**, 2961—2971.

Keller, D., C. Bustamante, and I. Tinoco, 1985: Model computations on teh differential scattering of circularly polarized light (CIDS) by dense macromolecular particles. *Biopolymers*, **24**, 783—797.

Kerker, M., 1969: *The scattering of light and other electromagnetic radiation.* Academic Press, New York and London.

Kikuchi, K. and A. W. Hogan, 1979: Properties of diamond dust type ice crystals observed in summer season at Amudsen-Scott South Pole station, Antarctica. *J. Met. Soc. Jap.*, **57**, 180—190.

Killinger, R. T. and R. H. Zerull, 1988: Effects of shape and orientation to be considered for optical particle sizing. In *Optical particle sizing: theory and practice*, Plenum Press, N. Y., 419—429.

Kirkwood, J. G., 1936: On the theory of dielectric polarization. *J. Chem. Phys.*, **4**, 592—601.

Kobayashi, T., 1961: . *Philos. Mag.*, **6**, 1361.

Kobayashi, T., Y. Furukawa, K. Kikuchi, and H. Uyeda, 1976: On twinned structures in snow crystals. *J. Crystal Growth*, **32**, 233—249.

Kokodii, N. G., 1985: Radiation pressure on large-diameter cylindrical particles. *Opt. Spectrosc.*, **59**, 219—221.

Ku, J. C. and K.-H. Shim, 1992: A comparison of solutions for light scattering and absorption by agglomerated or arbitrary-shaped particles. *J. Quant. Spectrosc. Radiat. Transfer*, **47**, 201—220.

Kuznetsov, V. V. and L. N. Pavlova, 1988: Attenuation and absorption of radiation by optically soft cylindrical particles. *Bull. USSR Acad. Sci. Atmos. Oceanic Phys.*, **24**, 147—151. English translation.

Latimer, P., 1975: Light scattering by ellipsoids. *J. Col. Interface Sci.*, **53**, 102—109.

Lee, C. W., 1972: On the crystallographic orientation of patial branches in natural polycrystalline snow crystals. *J. Meteor. Soc. Japan*, **50**, 171—180.

Leubner, C., 1979: Coordinate-free rotation operator. *Am. J. Phys.*, **47**(8), 727—729.

Liou, K.-N., 1974: On the radiative properties of cirrus in the window region and their influence on remote sensing of the atmosphere. *J. Atmos. Sci.*, **31**, 522—532.

Liou, K. N., Q. Cai, J. B. Pollack, and J. N. Cuzzi, 1983: Light scattering by randomly oriented cubes and parallelepipedes. *Appl. Opt.*, **22**, 3001—3008.

Mackowski, D., 1992: . private communication.

Mackowski, D. W., 1991: Analysis of radiative scattering for multiple sphere configurations. *Proc. R. Soc. Lond. A*, **433**, 599—614.

Mahood, R. W., 1987: The application of vector diffraction to the scalar anomalous diffraction approximation of van de Hulst. Master's thesis, The Pennsylvania State University, Department of Meteorology.

Manabe, S. and R. T. Wetherald, 1967: Thermal equilibrium of the atmosphere with a given distribution of relative humidity. *J. Atmos. Sci.*, **24**, 241—259.

McClain, W. M., J. A. Schauerte, and R. A. Harris, 1984: Model calculations of intramolecular interference effects in Raleigh scattering from solutions of macromolecules. *J. Chem. Phys.*, **80**, 606—616.

Minnis, P., K.-N. Liou, and Y. Takano, 1992: Inference of cirrus cloud properties using satellite-observed visible and infrared radiances. Part I: Parameterization of radiance fields. in press Journal of Atmospheric Sciences.

Morris, A. H., 1990: NSWC library of mathematics subroutines. Technical Report NSWC TR 90-21, Naval surface warfare center, Dahlgren, Virginia 22448-5000, 492.

Nakaya, U., 1954: *Snow cystals — natural and artificial.* Harvard University Press, Cambridge, MA.

Napper, D. H., 1966: A diffraction theory approach to the total scattering by cubes. *Kolloid-zeitschrift und Zeitschrift fur Polymere*, **218**, 41—46.

Napper, D. H. and R. H. Ottewill, 1963: Light scattering studies on monodisperse silver bromide sols. In *ICES Electromagnetic scattering*, Kerker, M., editor, Clarkson College of Technology, Pergamon Press, N. Y., 377—386.

Nussenzweig, H. M. and W. J. Wiscombe, 1980: Efficiency factors in Mie scattering. *Phys. Rev. Lett.*, **45**, 1490—1494.

Ono, A., 1971: Some aspects of the natural glaciation processes in relatively warm maritime clouds. *J. Meteor. Soc. Japan*, **49**, 845—858.

Perrin, J.-M. and P. l. Lamy, 1983: Light scattering by large rough particles. *Optica Acta*, **30**, 1223—1244.

Perrin, J.-M. and P. L. Lamy, 1986: Light scattering by large particles II. A vectorial description in the eikonal picture. *Optica Acta*, **33**, 1001—1022.

Perry, R. J., A. J. Hunt, and D. R. Huffman, 1978: Experimental determinations of Muller scattering matrices for nonspherical particles. *Appl. Opt.*, **17**, 2700—2710.

Peterson, A. F., S. L. Ray, C. H. Chan, and R. Mittra, 1991: Numerical implementation of the conjugate gradient method and the CG-FFT for electromagnetic scattering. In *Application of conjugate gradient method to electromagnetics and signal processing*, Sarkar, T. K., editor. Elsevier, New York, 634.

Pipkin, A. C., 1991: *A course on integral equations*, volume 9 of *Texts in applied mathematics*. Springer-Verlag, New York, 268.

Platt, C. M. R., D. R. Reynolds, and N. L. Ashire, 1980: Satellite and lidar observations of the albedo, emittance and optical depth of cirrus compared to model calculations. *Mon. Wea. Rev.*, **108**, 195—204.

Platt, C. M. R. and G. L. Stephens, 1980: The interpretation of remotely sensed high cloud emittances. *J. Atmos. Sci.*, **37**, 2314—2322.

Pollack, J. B. and J. N. Cuzzi, 1980: Scattering by nonspherical particles of size comparable to a wavelength: A new semi-empirical theory and its application to tropospheric aerosols. *J. Atmos. Sci.*, **37**, 868—881.

Pruppacher, H. R. and J. D. Klett, 1978: *Microphysics of clouds and precipitation.* D. Reidel Publishing Comp.

Purcell, E. M. and C. R. Pennypacker, 1973: Scattering and absorption of light by nonspherical dielectric grains. *Astrophys. J.*, **186**, 705—714.

Saxon, D. S., 1955: Scattering of light. Technical report, University of California, Dept. of Meteorology, Los Angeles, Calif. Sci. Rep. 9.

Schureman, D. W., R. T. Wang, B. S. Gustafson, and R. W. Schaefer, 1981: A systematic study of light scattering: I. Particle shape. *Appl. Opt.*, **20**, 4039—4050.

Sedgewick, R., 1983: *Algorithms.* Addison-Wesley, Reading, Mass.

Shah, G. A., 1990: Asymmetry parameter and efficiency for radiation pressure and scattering of electromagnetic radiation by a very large dielectric sphere. *Astrophysics and Space Science*, **178**, 251—260.

Sharma, S., S. K. Sharma, and D. J. Somerford, 1984a: The eikonal approximation to near-forward light scattering from homogeneous sphere. *Optica Acta*, **31**, 867—871.

Sharma, S. K., S. R. Powers, and D. J. Somerford, 1981: Investigation of domains of validity of approximation methods in forward light scattering from long cylinder. *Optica Acta*, **11**, 1439—1446.

Sharma, S. K., S. Sharma, and D. J. Somerford, 1984b: A new formula for backward optical scattering. *Optica Acta*, **31**, 981—982.

Sharma, S. K., D. J. Somerford, and S. Sharma, 1982: Investigation of domains of validity of corrections to the eikonal approximation in forward light scattering from homogeneous spheres. *Optica Acta*, **29**, 1677—1682.

Singham, M. K., S. B. Singham, and G. C. Slazman, 1986: The scattering matrix for randomly oriented particles. *J. Chem. Phys.*, **85**, 3807—3815.

Singham, S. B. and C. F. Bohren, 1989: Hybrid method in light scattering by an arbitrary particle. *Appl. Opt.*, **28**, 517—522.

Singham, S. B. and G. C. Salzman, 1986: Evaluation of the scattering matrix of an arbitrary particle using the coupled dipole approximation. *J. Chem. Phys.*, **84**, 2658—2667.

Smith, C. B., 1982: Inversion of the anomalous diffraction approximation for variable complex index of refraction near unity. *Appl. Opt.*, **21**, 3363—3366.

Stephens, G. L., 1980: Radiative properties of cirrus clouds in the infrared region. *J. Atmos. Sci.*, **37**, 435—446.

Stephens, G. L., 1984: Scattering of plane waves by soft obstacles: Anomalous diffraction theory for circular cylinders. *Appl. Optics*, **23**, 954—959.

Stephens, G. L., 1986: On the effect of ice porosity on the radiative characteristics of cirrus clouds. Submitted to J. Geophys. Res.

Stephens, G. L., S.-C. Tsay, P. W. Stackhouse, and P. J. Flatau, 1990: The relevance of the microphysical and radiative properties of cirrus clouds to climate and climate feedback. *J. Atmos. Sci.*, **47**, 1742-1753.

Stephens, G. L. and P. J. Webster, 1981: Clouds and climate: sensitivity of simple systems. *J. Atmos. Sci.*, **38**, 235—247.

Takahashi, C., 1979: Formation of poly-crystalline snow crystals by rimming process. *J. Meteor. Soc. Japan*, **57**, 458—464.

Taubenblatt, M. A., 1990: Light scattering from cylindrical structures on surfaces. *Optics Letters*, **15**, 255—257.

Uyeda, H. and K. Kikuchi, 1979: Observations of the three dimensional configuration of snow crystals of combination of bullet type. *J. Meteor. Soc. Japan*, **57**, 488—492.

van de Hulst, H. C., 1957: *Light scattering by small particles*. Dover Publications, Inc., New York.

van de Hulst, H. C., 1980: *Multiple light scattering. Tables, formulas, and applications*, volume 2. Academic Press, New York, 739.

Volkovitskiy, O. A., L. M. Pavlova, and V. P. Snykov, 1975: Scattering-property asymmetry of crystaline clouds. *Izv., Atmos. and Oceanic Phys.*, **11**, 475—477.

Volkovitskiy, O. A., L. N. Pavlova, and A. G. Petrushin, 1980: Scattering of light by ice crystals. *Izv., Atmos. and Oceanic Phys.*, **16**, 98—102.

Vouk, V., 1948: Projected area of convex bodies. *Nature*, **162**, 330—331.

Wang, R. T. and B. S. Gustafson, 1984: Angular scattering and polarization by randomly oriented dumbells and chains of spheres. In *Proceedings 1983 CSL scientific conference on obscuration and aerosol research*, Framer, J. and Kohl, R. H., editors, U. S. Army CSL CRDC-SP-84009, Aberdeen, MD, 237—247.

West, R. A. and P. H. Smith, 1991: Evidence for aggregate particles in the atmospheres of Titan and Jupiter. *Icarus*, **90**, 330—333.

Whalley, E. and G. E. McLaurin, 1984: Refraction halos in the solar system. I. Halos from cubic crystals that may occur in atmospheres in the solar system. *J. Opt. Soc. Am. (A)*, **1**, 1166—1170.

Wiscombe, W. J. and A. Mugnai, 1986: Single scattering from nonspherical Chebyshev particles: A compendium of calculations. NASA Reference Publication 1157, Goddard Space Flight Center, Greenbelt, Maryland.

Wiscombe, W. J. and A. Mugnai, 1988: Scattering from nonspherical Chebyshev particles. 2: Means of angular scattering patterns. *App. Opt.*, **27**, 2405—2421.

Wright, E. L., 1987: Long-wavelength absorption by fractal dust grains. *Astrophys. J.*, **320**, 818—824.

Yokoyama, E. and T. Kuroda, 1990: Pattern formation in growth of snow crystals occuring in the surface kinetic process and the diffusion process. *Phys. Rev. A*, 41, 2038—2049.

Yung, Y. L., 1978: Variational principle for scattering of light by dielectric particles. *Appl. Opt.*, **17**, 3707—3709.

Zege, E. P. and A. A. Kokhanovskiy, 1988: Integral characteristics of light scattering by large spherical particles. *Bull. USSR Acad. Sci. Atmos. Oceanic Phys.*, **24**, 508—512.

Zerull, R. and R. H. Giese, 1974: Microwave analogue studies. In *Planets, stars and nebulae studied with photopolarimetry*, Gehrels, T., editor. The University of Arizona Press, Tucson, Arizona, 901—915.

Zerull, R. H., 1976: Scattering measurements of dielectric and absorbing nonspherical particles. *Beitr. Phys. Atmos.*, **49**, 168—188.

Zerull, R. H., R. H. Giese, and K. Weiss, 1977a: Scattering functions of nonspherical dielectric and absorbing particles vs Mie theory. *Appl. Opt.*, **16**, 777—778.

Zerull, R. H., R. H. Giese, and K. Weiss, 1977b: Scattering measurements of irregular particles vs Mie theory. *SPIE*, **112**, 191–199. Optical polarimetry.